THE EFFECTS OF DIATOM FRUSTULE FILLING ON THE QUASI-STATIC AND HIGH STRAIN RATE MECHANICAL BEHAVIOR OF POLYMER MATRICES

A Thesis Submitted to
the Graduate School of Engineering and Sciences of
Izmir Institute of Technology
in Partial Fulfillment of the Requirements for the Degree of

DOCTOR OF PHILOSOPHY

in Mechanical Engineering

by
Elif GÜLTÜRK

December 2010
İZMİR

ACKNOWLEDGEMENTS

I would like to thank my advisor, Prof. Dr. Mustafa GÜDEN and my co-adviser Assoc. Prof. Dr. Alper TAŞDEMİRCİ for their invaluable advice, guidance, and encouragement. I am grateful to the other committee members.

I would like to thank to the workers of IZTECH Materials Research Center (IYTE-MAM) for their helps in the analysis of XRF, XRD and SEM. I would also like thank to Research Specialist of IZTECH Environmental. Research Center, Esra TUZCUOĞLU, for assisting me in performing FTIR measurements.

Special thanks go to Prof. Dr. Hürriyet POLAT for their helps in particle size measurement analysis.

We acknowledge The Scientific and Technical Research Council of Turkiye (TUBITAK) for financial support to 106M186 project and İYTE-BAP for support to 2008İYTE04 project.

I would like to thank my friends Levent AYDIN, Kutlay ODACI, Sinan YÜKSEL, Deniz KARSU and Ceylan ŞENÖZ for their encouragement, help and patience. I would like to appreciate deeply my room-mates Meral BUDAK, and Gözde TUNUSOĞLU for the moments that we shared together.

I am grateful to my parents ‘‘Nurhayat and Hasan ARAS’’ and my brother and sister for their constant encouragement and support.

Finally, I would like to express my special thanks to my husband Assoc. Prof. Dr. Sefa GÜLTÜRK and my daughter Hilal GÜLTÜRK for their constant encouragement, support and patience during this graduate work.

ABSTRACT

THE EFFECTS OF DIATOM FRUSTULE FILLING ON THE QUASI-STATIC AND HIGH STRAIN RATE MECHANICAL BEHAVIOR OF POLYMER MATRICES

In this study quasi-static tension and quasi-static ($1x10^{-3}$ and $1x10^{-1}$ s^{-1}) and high strain rate (300-600 s^{-1}) compression and quasi-static tensile behavior of diatom frustules-filled, Diatomaceous earth (CD) and Kieslguhr (ND), epoxy matrices were investigated experimentally and microscopically. For comparison, the compression and tensile behavior of the neat epoxy was also determined. Compression results showed that diatom frustules filling increased both modulus and yield strength of the epoxy matrix at quasi-static and high strain rates. ND frustules filled epoxy samples showed a higher strain rate sensitivity compare with CD filled samples. Tensile test results showed that the modulus of filled epoxy increased with increasing frustule content. The frustule filling, however, decreases the tensile failure strains of the epoxy and increased the tensile strength slightly. Microscopic observations on the fracture surfaces and the mounted cross-sections of deformed samples showed that the failure mechanisms were debonding of the frustules-epoxy interface and the fracture of the frustules at quasi-static strain rates while the failure of the filled composite at high strain rate was dominated by the fracture of the matrices. These results confirmed that significant benefits might anticipated from the use of diatom frustules as reinforcements and fillers in polymeric materials. Various methods; acid leaching, thermal shock and ball milling were further applied to process nano size silica powder from frustules. Projectile impact tests indicated that frustule addition increased the ballistic resistance of epoxy matrices. Finally, the strength and modulus of the filled epoxy matrices were predicted using analytical models developed for short fiber composites.

ÖZET

POLİMER MATRİSLERDE DİATOM KABUK KATKISININ STATİK VE YÜKSEK HIZ DEFORMASYON DAVRANIŞLARINA ETKİLERİ

Bu tezin amacı farklı diatom kabuklarının polimer matriste dolgu malzemesi olarak kullanılması ve kabuk katkısının matrisin statik ($1x10^{-3}$ and $1x10^{-1}$ sn^{-1}) ve yüksek hız (300-600 sn^{-1}) deformasyon davranışlarına etkilerini araştırmaktır. Bu çalışmada katkı malzemesi olarak iki farklı tip diatom (Diatomaceous earth (CD) and Kieslguhr (ND)) kullanılmıştır. Saf epoksinin basma ve çekme davranışları belirlenmiş ve karşılaştırılmıştır. Statik ve yüksek hız gerinme oranlarında yapılan basma test sonuçları, elastiklik modülünün ve basma dayanımının diatom kabuk katkısının artmasıyla arttığını göstermiştir. ND kabuk katkılı epoksi örneklerin gerinme oranına duyarlılığı daha yüksek bulunmuştur. Çekme testi sonuçlarında kabuk katkısının artmasıyla elastiklik modülü yükselmiştir. Örneklerin kırılma yüzeyleri mikroskobik olarak incelendiğinde, statik gerinme oranlarında test edilen örneklerin kopma mekanizmaları kabuk ve matris arasından sıyrılmalar ve kabukların kırılması şeklindedir. Yüksek gerinme oranlarında ise matris baskın kırılma gerçekleşmektedir. Bu çalışma diatom kabuklarının polimerik yapılarda katkı malzemesi olarak kullanılabilirliğini ve polimer malzemelerin mekanik özelliklerini iyileştirdiğini göstermiştir. Diatom kabuklarından silika toz elde etmek için asitle dağlama, bilyalı öğütme ve termal şok yöntemleri kullanılmıştır. Balistik test sonuçları diatom kabuk katkısının balistik performansı artırdığını göstermiştir. Son olarak, analitik komposit modelleri kullanılarak elastiklik modülü değerleri hesaplanmış ve bu değerler deneysel verilerle karşılaştırılmıştır.

TABLE OF CONTENTS

LIST OF FIGURES

LIST OF TABLES

CHAPTER 1

INTRODUCTION

1.1. Introduction

Polymer and polymer matrix composites have been widely investigated because of their low cost and ease processing, but the wider use of polymeric materials is limited as these materials have relatively low strength and stiffness as compared with other conventional engineering materials such as metals. Different fillers having high stiffness and relatively low density are often incorporated into polymer matrices to improve the mechanical, physical and functional properties. The most common used reinforcements in polymer matrices include carbon, glass and aramid fibers. The particulate filled polymer resins have also been investigated since the last two decades, due to their increasing applications in coatings, electronic packaging, dental restoratives, engine covers and beverage packaging (Xing and Li 2004). Studies have shown that micro/nano particle filling such as SiO_2, Al_2O_3, $Mg(OH)_2$, TiO_2, $CaCO_3$ particles, Carbon nanotubes (CNTs), mesoporous silica and layered silicate particles improves the mechanical, thermal, physical and electrical properties of polymers (Beier, et al. 2007, Chatterjee and A.Islam 2008, Fu Shao-Yun 2008, Guo, et al. 2005, Singh, et al. 2002, Zhang, et al. 2006, Zhao, et al. 2008). Few studies have been focused on the use of natural fibers as the replacement for custom fillers and fibers in the composites (Zafeiropoulos, et al. 2002). There have been numerous studies on the use of natural fibers and particles as an alternative reinforcement in polymer matrices including such as wood flour (Ichazo, et al. 2001), sisal fibers (Joseph, et al. 1999), sawdust (Suarez, et al. 2003), oil palm empty fruit bunch fibers (Hassan, et al. 2010), spongollite (natural amorphous silica fibers) (Barra, et al. 2006), okra fibers (De Rosa, et al. 2010), textile fibers (Tasdemir, et al. 2010) and natural zeolite fillers (Metin, et al. 2004). Incorporation of different fillers into polymer matrices seems to improve stiffness, dimensional stability and in some cases the strength of polymer matrix.

The studies reported in the literature till now were performed to determine the effects of different filler materials on the performance of various types of resins. It is

known that the geometrical properties of filler can have significant effects on the mechanical properties of composites. The composite stiffness for example depends significantly on the particle volume fraction as the fillers have much higher elastic modulus than the matrix. The good particle matrix adhesion increases the toughness and strength. The surface area of the filler material is also important to improve the mechanical properties of polymer matrices as it directly affects particle matrix adhesion. High surface area is usually associated with small filler size and very rough surfaces. Therefore, owing to intricate morphology and the high surface area/volume ratio, diatom frustules may be used as the reinforcing filler in polymeric composites. This potential is the main motivation of this thesis.

Diatoms are single-celled algae, living in aquatic environments (Round, et al. 1990). The shell of the diatoms, known as a frustule, is made of nano-sized silica particles with an intricate 3D structure. When these aquatic plants cells die, the silica shell/frustules form diatomaceous earth (diatomite) on the floor of the ocean. Diatomaceous earth is an abundant, extremely cheap material and extensively used in sound and heat insulation, abrasives, filters, absorbents, and explosives (Werner 1977). Recent studies have also shown that intricate microscale polymeric and ceramic structures including zirconia (Gaddis and Sandhage 2004, Zhao, et al. 2005) gold nanostructures (Losic, et al. 2005) and MgO and TiO_2 structures (Sandhage, et al. 2005) can be prepared with relatively simple processing steps using the diatom frustules as transient scaffolds, templates and in solid–gas displacement reactions, respectively. The potential engineering and medical applications of diatom frustules have also recently been proposed, including metal film membranes, pinpoint drug delivery and processing of nanopowder silica (Wee, et al. 2005). The surface area of diatomaceous earth was reported to be relatively high, 22 m^2/g (Vrieling, et al. 1999a) and it was shown to decrease slightly with the applied heat-treatment (Goren, et al. 2002). Polyaniline-diatomite composites were previously prepared by the oxidation of aniline in the presence of diatomite(Li, et al. 2003a, Li, et al. 2003b). These studies were mainly focused on the electrical properties and there was no study on the effect of diatom frustules on the mechanical properties of the composites in literature. In this study, two types diatom frustules, natural and calcined, were used as filler in an thermosetting resin in order to assess the possible effects of the frustules on the mechanical properties at quasi-static and high strain rates. It was proposed that the thermosetting resin might

penetrate through the micro pores of diatom frustules and cause the mechanical interlocking between frustules and matrix.

1.2. Dissertation Outline

Literature review on the polymer matrices reinforced with different filler materials are given in Chapter 2. The mechanical properties of reinforced polymers are also summarized in this chapter. The frustules formation and structure and the engineering and medical applications of diatom frustules are reviewed in Chapter 3. The characterization studies on the diatom frustules using Scanning Electron Microscopy (SEM), X-Ray Florescence spectrometer (XRF), Fourier transform infrared spectroscopy (FTIR) and the X-ray diffraction (XRD) and particle size analysis are given in Chapter 4. Chapter 5 is on the experimental studies to form silica powders from diatom frustules using different methods. The details of processing frustules and Differential Scanning Calorimeter (DSC) results are reported in Chapter 6. The curing behavior and thermal stability of the epoxy resin investigated through Dynamic Scanning Calorimetry and Fourier Infrared Spectroscopy are reported in Chapter 7. The effect of frustule addition on the quasi-static and high strain rate mechanical behavior of filled epoxy and the projectile test results are given in Chapter 8. The mechanical properties of filled epoxies were predicted using law of mixture, shear lag, modified shear lag and Eshelby models and the results are shown in Chapter 9. Finally, the conclusions of the thesis study are given in Chapter 10.

CHAPTER 2

LITERATURE REVIEW

Composites are important class of engineering materials, which are made from two or more constituents. The matrix material surrounds the reinforcement, which has special mechanical and physical properties that enhance the matrix. Most composites in industrial use today are based on polymeric matrices, either thermosetting or thermoplastics. The most common matrices used include polyester, vinyl ester, epoxy, phenolic, polyimide, polyamide, polypropylene, and PEEK. Ceramic, carbon and glass materials are among the widely used reinforcements.

2.1. Thermosetting Resins and Reinforcement

The thermosetting resins have usually good abrasion and dimensional stability as compared with the thermoplastics, while thermoplastics have better flexural and impact properties. In thermosetting polymers, the liquid resin is converted into hard rigid solid by the chemical cross-linking, which causes the formation of a strong three dimensional network structure. The mechanical properties depend on the molecular units making up the network and on the length and density of the cross-links. The most commonly used thermosetting resins are epoxy, unsaturated polyester and vinly ester. Epoxy resins are one of the most important thermosetting materials that have been widely chosen due to their excellent thermal, mechanical and electrical properties and relatively low cost. Epoxies are in general tougher than unsaturated polyester and vinyl esters and shrink less during curing than polyesters.

Many different reinforcements can be used for a particular and short fiber matrix system. All reinforcement has generally high stiffness and relatively low density. The most common used reinforcements are carbon, glass and aramid fibers which used extensively in polymer matrix composites. Besides, ceramic fibres, whiskers and particles can also be used to reinforce matrix material. Composites are classified by the geometry of the reinforcement as particulate, flake, and fiber reinforced matrices.

2.2. The Mechanical Behavior of Particulate Polymeric Composites

The prediction of the mechanical behavior of the particulate filled polymer matrix composites is very complex problem as many variables involve. The mechanical behavior depends on the properties of the resin, filler and the volume fractions of both constituents. In addition, the geometrical factors such as filler aspect ratio, particle size and mean inter particle distance are also important parameters affecting the mechanical properties.

The large aspect ratios of filler play a significance role to enhance mechanical behavior of particulate reinforced polymeric composites. Carbon nano tubes (CNTs) with large aspect ratios, extraordinary mechanical, thermal and electrical properties have been used as reinforcing fillers in various types of polymers to improve the mechanical properties. Beier et al.(Beier, et al. 2007) however, reported that further development for the achievement of optimal dispersion and orientation of CNT reinforcement war necessary in order to attain the best possible properties. Young's modulus of the polymer matrices can be improved by the addition of micro/nano size particles as the rigid inorganic particles have a much higher stiffness than polymer matrices. Radford (Radford 1971) examined the mechanical properties of (~30 vol%) alimuna trihydrate particulate (1, 2, 5, 8, and 12 μm) filled epoxy composites. Results showed that the modulus of composites increased as compared with that of the neat epoxy and the particle size effect on the modulus was found to be not significant. Nakamura et al. (Nakamura, et al. 1992) studied the effect of particle size on the elastic modulus of epoxy/silica composites. Spherical and irregular shaped silica particles having distinct mean sizes of 2-30 μm were used as filler. The elastic modulus was shown to remain constant with increasing particle mean size. Kinloch and Taylor (Kinloch and Taylor 2006) investigated the elastic modulus of epoxy composites with various concentrations of the silicate modifiers up to 30 wt% depending. Five types of silicates having different particle diameter and aspect ratio were investigated. The elastic modulus was found to increase with increasing weight fraction of silica. The particle morphology was found to have an insignificant effect on the modulus. Fu et al. (Fu Shao-Yun 2008) investigated the elastic modulus of the spherical glass particle (4.5-62 μm.) filled epoxy composites. The modulus was shown to be independent of particle size at low glass particle volume percentages (10-18%), while a small decrease in the

elastic modulus with the increasing particle size for relatively high particle volume percentages (30-46%) was reported. Chatterjee and Islam (Chatterjee and A.Islam 2008) examined the thermal, mechanical, morphological and the viscoelastic properties of nano size TiO_2 (5–40 nm, 0.5–2 wt%) filled epoxy composites. The nano filler infusion improved the thermal, mechanical and viscoelastic properties of the epoxy resin. The composite with 1% and 5 nm size TiO_2 showed increase in storage modulus, glass transition temperature, tensile modulus, flexural modulus and short beam shear strength. Ji et al. (Ji, et al. 2002) theoretically predicted the elastic modulus of a polymer composite filled with particles of different sizes (3-3000 nm). Results showed that the particles below a critical size of 30 nm increased elastic modulus of the composite as compared with the larger particles. In addition, the static/dynamic modulus, micro hardness, and fracture toughness of 25 nm silica nano particle filled composite were were investigated by Zhang et al. (Zhang, et al. 2006). The results showed that homogeneously distributed nano particles improved the stiffness and toughness, the static/dynamic modulus and micro hardness. In addition, the fracture toughness also increased with increasing silica content up to 14 vol%. Significant improvements in both stiffness and toughness were found when the inter particle distance was smaller than the particle diameter. Under this condition, the interphase was proposed to construct a three dimensional physical network, which dominated the performances of nano composites. Chen et al. (Chen, et al. 2008b) studied epoxy composites with two types of nanoparticles: (a) fumed silica (termed primary particles) with an average size of 12 nm (10-15 nm) and the additions of 1, 3, 5 and 15 wt%, and (b) well-dispersed agglomerates of 14 nm silica with 100 nm average size and the additions of 0.6, 3 and 5wt%. The composite modulus of 12 nm silica composites increased with increasing particle weight percentages. The composites with 100 nm silica particles showed a significant increase in modulus at 0.6 wt%, which then decreased with increasing particle weight percentages. The fracture toughness of 12 nm silica filled composites increased by 35% for 15 wt% of silica addition. Ahmad et al. (Ahmad, et al. 2008) investigated the effects of percentage of filler loading (0, 15, 30 and 45 vol%) and shapes of silica mineral particles on the mechanical and thermal properties of a composite system. Three different particles angular, cubical and elongated in shape were used to fill the composite. Elongated silica particle added composites exhibited the highest flexural strength, flexural modulus, tensile strength and tensile modulus. Chen

et al. (Chen, et al. 2008a) investigated thermal and mechanical properties of epoxy–nano composite resins filled with 12 nm spherical silica particles of various percentages. The nano particles were easily dispersed with minimal aggregation up to 25 wt%, which was determined using transmission electron microscopy and ultra-small-angle X-ray scattering. A proportional decrease in cure and glass transition temperature for the particle addition of 10 wt% and above was reported for the increased silica percentages. For samples with particle additions less than 10 wt%, 25% increase in tensile modulus and 30% increase in fracture toughness were found. At relatively increasing particle additions, the elastic modulus increased, but the strength and fracture toughness decreased. Sahu and Broutman (Sahu and Broutman 1972) studied the mechanical properties of glass bead (30 μm) filled epoxy and polyester resins as a function of volume percentages of filler and the strength of the interfacial bond. The bonding between glass bead and resin varied with the chemical surface treatment of glass beads with a silane coupling agent. No effect of interfacial bonding on the elastic modulus was shown.

Purkanszky and Voros (Pukanszky B 1993) examined the particle size effect on the tensile yield strength of $CaCO_3$/Polypropylene composites and showed that the strength increased with decreasing particle size. This exhibited an increase in the strength with increasing the surface area of filled particles. The composite however showed decrease in strength with increasing particle volume percentages for the particles larger than 80 nm. Park and Pinnavaia (Park and Pinnavaia 2007) examined the epoxy polymer reinforced with mesoporous silica (1.0–9.0 wt%). Mesocellular foam structure exhibited very large cell sizes, 25–35 nm, window sizes, 7–18 nm, and high pore volumes up to 2.4cm^3g^{-1}. The modulus, strength, elongation and toughness of the composites increased with increasing silica weigh percentage addition. Radford (Radford 1971) examined the mechanical properties of 10 vol% alimuna trihydrate particle (1, 8 and 12 μm) filled epoxy composites. The tensile strength of the composite decreased with increasing mean particle size. Thio et al. (Thio, et al. 2004) examined the effect of interfacial adhesion on the mechanical properties of glass/PP composites. The glass particles (3.5 μm) were modified with two silane groups having distinct functional group, hydrocarbons and fluorocarbons. The adhesion strength between glass and polypropylene increased with increasing coverage of the hydrocarbon silanes and the tensile strength of the polypropylene composites increased with increasing

interfacial adhesion.

Nakamura et al. (Nakamura, et al. 1993) examined the fracture toughness of epoxy composites filled with 55 wt% angular shaped silica particles (2-47 μm). The fracture toughness increased with increasing mean size of silica particles. Adachi et al. (Adachi, et al. 2008) investigated the effects of particle size and volume fraction on the mode I fracture toughness of epoxy composites filled with spherical silica particles and various particle diameters ranging between 1.56 μm to 240 nm and volume fractions of 0 to 0.35. It was found that the modulus at a volume fraction of 0.35 was twice that of the neat epoxy resin. The fracture toughness increased as the volume fraction increased. Although the particle diameter had little influence on the fracture toughness at low volume fractions, the fracture toughness was found to be strongly dependent on the particle diameter at relatively high volume fractions. The fracture toughness at a volume fraction of 0.30 for a particle diameter of 240 nm was 1.7 times that for a particle diameter of 1.56 μm and 2.5 times that for epoxy resin. Singh et al. (Singh, et al. 2002) discussed the fracture toughness of the different mean sizes of alumina particle filled polyester resin with the particle addition between 0 to 4.4 vol%. It was found that the toughness increased monotonically with the increasing particle volume percent for the particle sizes between 3.5 μm and 20 μm. At the same particle addition, 4.4 vol%, the toughness increased by 51% and 22% compared to the neat resin, respectively. The toughness for the particles of 100 nm increased up to 2.3 vol% particle addition, then decreased. Whichman (Wichmann, et al. 2006) investigated the mechanical properties of fumed silica/epoxy composites. The fracture toughness significantly increased (54%) with 0.5 vol% of surface modified fumed silica addition. Kwon and Adachi (Kwon and Adachi 2007) discussed the effect of 240 nm and 1.56 μm silica particle addition on the strength and fracture toughness of the epoxy resin. An increase in the content of nano particles gave rise to an increase in the strength and fracture toughness and a decrease in the fragility of the composites. However, the mechanical properties of the composite were reported to increase regardless of glass transition temperature. In addition, although varying composition ratio of particles did not significantly affect the bending modulus, the bending strength and fracture toughness were found to be strongly dependent on the particle composition. The bending strength and fracture toughness of the composite with a high composition ratio of smaller particles were 1.3 and 2.5 times higher than those of epoxy resin, and 1.3 and 1.7 times higher than those of composite

with lower composition ratio, respectively (Kwon, et al. 2008). Guo et al. (Guo, et al. 2005) prepared neat and modified $CaCO_3$ particles filled polypropylene composite with the particle additions up to 40 wt%. $CaCO_3$ particles (40 nm) were covered with the lanthanum compound by the chemical deposition. The impact toughness of the composites increased with increasing the particle loading and with the addition of lantanium up to 15 wt%. Fu et al. (Fu Shao-Yun 2008) noted that increasing the particle matrix adhesion using coupling agents did not enhance the toughness of the thermosets. Strong adhesion caused high toughness in thermoplastic resins but not necessary in thermosetting matrices as the different failure mechanisms involved. Ma et al. (Jun Ma 2008) studied the effect of silica nano particles on the mechanical properties of epoxies cured by Jeffamine D230 (denoted J230) and 4,40-diaminodiphenyl sulfone (denoted DDS), respectively. Silica nano particle addition of 20 wt% resulted in 40% improvement in elastic modulus for both epoxies and increased the toughness of J230-cured epoxy from 0.73 to 1.68 $MPam^{-1/2}$. Guo et al. (Guo and Li 2007) investigated the quasi-static and high strain rate behavior of 0, 3 and 7 wt% SiO_2/epoxy nano composites. Results showed that strain-rate hardening played a dominate role in the stress–strain behavior of the composites. The performance of the composite depended on the loading rate and nano particle dispersion. The compressive strength of the composites was higher than that of pure epoxy at high strain-rates, whereas there was no obvious trend between the compressive strength and the particle contents at low loading rates. Zhao and Li (Zhao and Li 2008) investigated the effect of water absorption on the mechanical and dielectric properties of Al_2O_3/epoxy nano composites. The degree of dispersion of the Al_2O_3 nanoparticles was shown to be rather poor and the particle agglomerations were present, when the particle loading was up to 10.0 phr. In addition, the incorporation of nano- Al_2O_3 particles was found to have little influence on the water adsorption of epoxy matrix. Due to the plasticization effect of adsorbed water, the tensile elongation of neat epoxy and the composite increased. Zhang et al. (Hui Zhang 2008) prepared a series of epoxy-based nano composites with various nano silica loadings and determined the effect of nano particle loading and test temperatures (23-80 ^oC). Imanaka et al. (Imanaka, et al. 2001) investigated the effect of particle size and particle/matrix adhesion on the fracture toughness of epoxy/silica composites. Silica particles were prepared with the mean particle sizes in the range of 6–30 nm. The particles were treated with g-minopropyl methyldiethoxysilane and hexamethyl

disilazane. The g-minopropyl methyldiethoxysilane treatment demonstrated well-bonded interfaces between the particle and matrix. The experimental results showed that the fracture toughness increased with increasing particle size. The toughness of specimens of good particle/matrix adhesion was slightly greater than that of poor particle/matrix adhesion. Kinloch and Taylor (Kinloch and Taylor 2006) discussed the mechanical properties and fracture behavior of epoxy matrix filled with inorganic micro and nano particles, including mica and organically modified montmorillonites, with the concentrations of the silicate modifier up to 30 wt%. The effect of the morphology of the inorganic particles was also investigated. The modulus of the composites increased with increasing weight fraction of silicate. The morphology had a small effect on the modulus. The fracture toughness increased as the weight fraction of the silicate increased. Xing and Li. (Xing and Li 2004) investigated the wear behavior of epoxy matrix composites filled with uniform sized sub-micron (120 and 510 nm) spherical silica particles. The spherical silica particles improved the wear resistance of the epoxy matrix even though the content of the fillers was relatively low (0.5–4.0 wt%). Barra et al. (Barra, et al. 2006) investigated the effect of natural amorphous silica fibers (NASF) on mechanical properties of Polyurethane matrix. NASFs were produced by the processing of a mineral, called “espongolite” or “spongollite,” and were derived from the skeleton of sponges and related organisms. Fillers were classified as nonscreened NASF, screened below 200 mesh (short and fragmented fibers, NASF-S), screened above 200 mesh (long fiber, NASF-L) and glass fiber (GF) (as-received, GF). The influence of fiber lengths and chemical treatments on the mechanical properties was evaluated. The tensile strength and elongation of the composites increased up to 17 wt% of fiber addition. Above this value, a reduction in the mechanical properties was found. The NASF-L reinforced composites showed an increase up to 55% in the tensile strength and 69% in the elastic modulus as compared with fiber glass reinforced composite. In addition, the tensile strength of NASF-AS reinforced composites increased 10% as compared with non treated NASF reinforced composite.

Pilyugin (Pilyugin 2008a, Pilyugin 2008b) investigated the impact properties of Al_2O_3 micro particle filled and neat epoxy targets tested with spherical metal projectiles with impact velocities ranged between 0.6 and 1.1 km/s. Complete fracture of the occurred at above 1 km/s projectile velocity. It was shown the strength of the target increased by a factor of approximately 1.5–2 at 40 wt% particle addition.

CHAPTER 3

DIATOM FRUSTULES

3.1. Diatoms

Diatoms are single-celled algae, belonging to the class of Bacilariophyceae of the phylum Baciloriophyta (Parkinson and Gordon 1999, Wee, et al. 2005). These are unicellular microscopic plants and inhabit all aquatic and moist environments. The growth of diatoms is responsible for about 25% of the world primary food production. Diatoms possess an enzyme that supports the photosynthesis reaction of CO_2 with H_2O and sunlight to produce food, releasing O_2 as a product. Diatoms are reported to be slightly more effective in removing atmospheric CO_2 than all the world's rain forests (Fuhrmann, et al. 2004). They exist in nature as benthic (attached to a sediment surface) and planktonic (free-floating) forms. Motile diatoms can lift 1000 times of their own weight by a motility mechanism which is 99% energy efficient (Gordon and Parkinson 2005).

Each diatom cell develops an external cell wall known as frustules. The frustule is composite of amorphous silica and an organic material (Wee, et al. 2005). There are over 100 000 different species of diatoms classified by cell wall geometry (Parkinson and Gordon 1999, Wee, et al. 2005). Diatoms are classified in two major groups based on the frustules symmetry: pennate and centric (Figure 3.1) (Goldberg, et al. 1998). Pennate types of diatoms tend to be elongated and are usually bilateral symmetrical. Centric types of diatoms are radial symmetric. Pennate diatoms have parallel striae which are the rows of holes in the silica arranged normal to the long axis. The spacing between the striae typically ranges from 0.3 to 2 μm. The rows of silica between the striae are called costae. Costae are arranged in combs or honeycombs (Figure 3.2). Besides their symmetry, frustules reveals an unparalleled difference in structure (Parkinson and Gordon 1999).

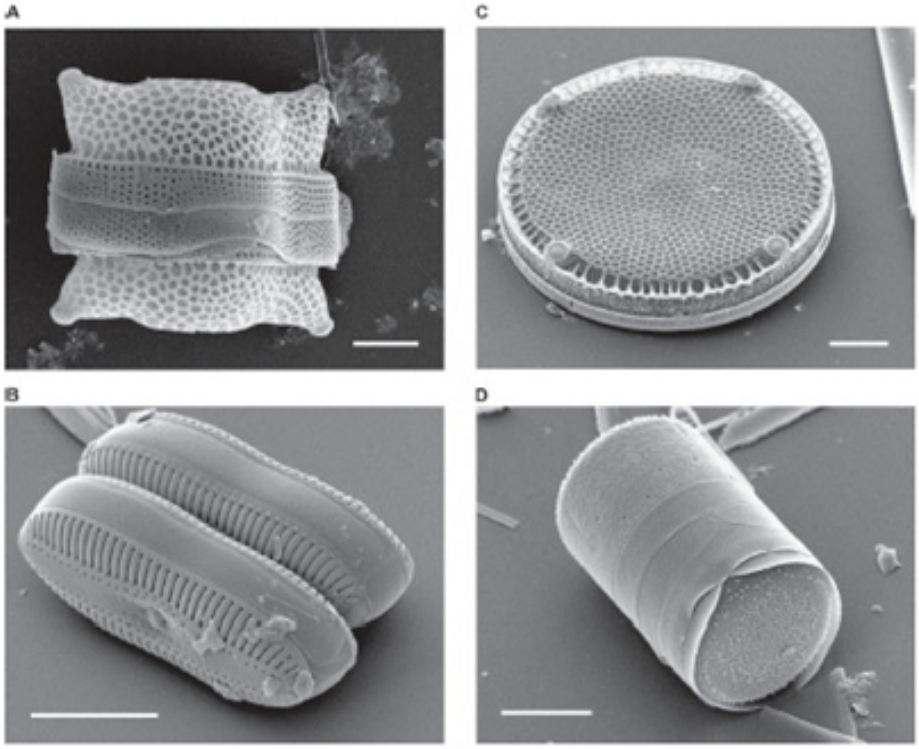

Figure 3.1. Scanning electron micrographs of diatoms (a) *Biddulphia reticulate*, the frustules of a centric diatom showing valves and girdle bands (size bar: 10 µm), (b) *Diploneis sp*. Two whole pennate diatom frustules (size bar: 10 µm), (c). *Eipodiscus radiates*. The single valve of a centric diatom (size bar: 20µm), (d). *Melosira varians*. Centric diatoms (size bar:10 µm). (Source:Bradbury 2004).

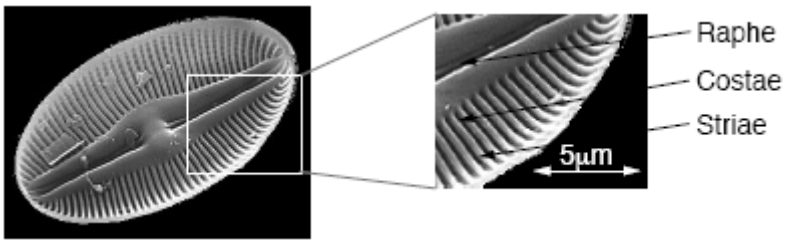

Figure 3.2. The pennate diatom showing the central raphe, the costae and the striae (Source: Parkinson and Gordon 1999).

The schematic of the components of diatom cell walls is shown in Figure 3.3. The diatom frustules are composed of two almost equal halves that fit together like a Petri dish, surrounding the bulk of the single cell within (Figure 3.3). The inner frustule is known as the hypotheca and the outer one as the epitheca (Figure 3.4). Each half (theca) consists of a valve which forms the larger outer surface and several ring-like silica structures known as girdle bands (Figures 3.3 and 3.4). Each diatom species forms

uniquely-shaped frustules with fine features such as pores, ridges and protuberances arrayed in intricate and species-specific patterns. The dimensions of amorphous silica skeletons range from ~1-500 µm, while the regular features distributed on the frustules wall possess characteristic dimensions of 10-200 nm (Fuhrmann, et al. 2004, Gaddis and Sandhage 2004).

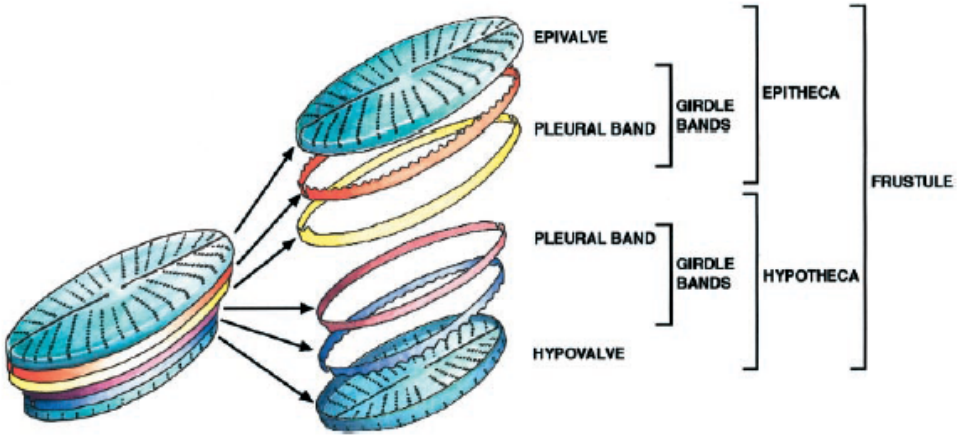

Figure 3.3. Schematic of the siliceous components of diatom cell walls (Source: Zurzolo and Bowler 2001).

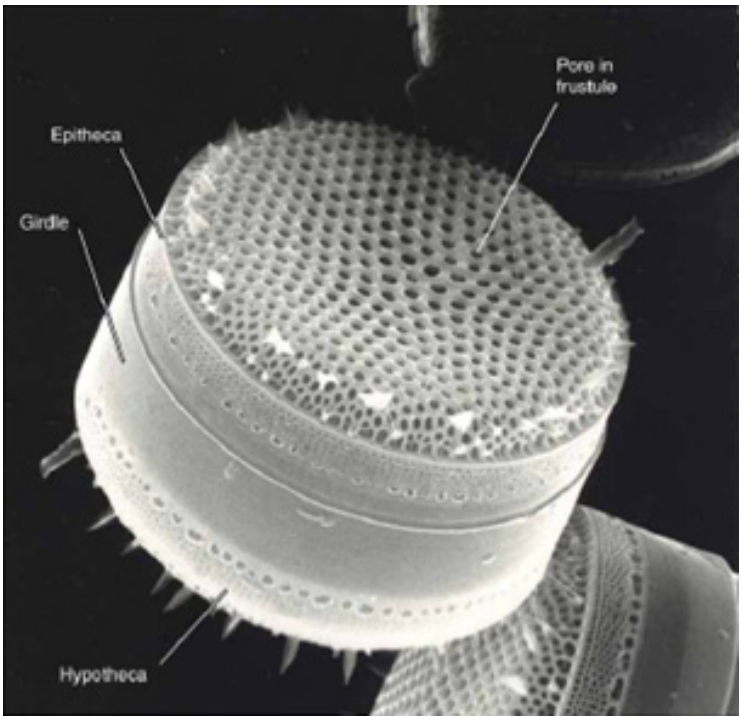

Figure 3.4. An SEM picture of *Thalassiosira* (Source: Crawford, et al. 2001).

The process of frustule formation is not well understood. It is thought that the mechanism involves the diffusion-limited precipitation of silica (Gordon and Drum 1994). The cell division does not occur unless there is sufficient bio-available silica for frustules formation and the silica necessity for frustules formation causes the growth of silica-dependent control points in diatom mitosis. The silica transport vesicles accumulate silica at intracellular concentrations up to 250 times higher than in the surrounding media. Cell-wall formation occurs primarily in SDVs, intracellular organelles in which an unpolymerized, soluble form of silicate. Amorphous silica particles of relatively low molecular weight and ~1–10 nm in diameter are thought to be transported to the perimeter of the SDV by silica transport vesicles (Figure 3.5). The particles released inside the SDV diffuse until they meet part of the growing aggregate, to which they adhere (Parkinson and Gordon 1999).

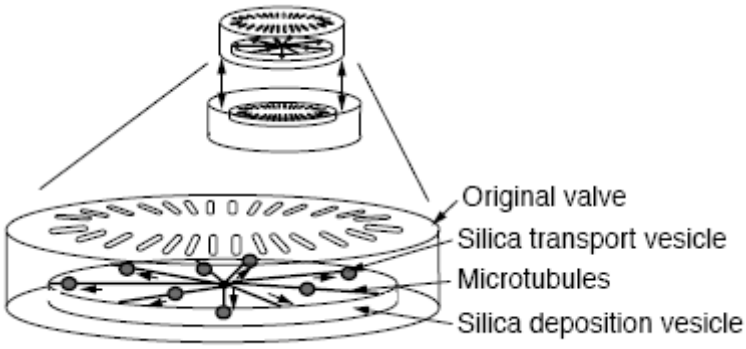

Figure 3.5. Proposed mechanism of diatom morphogenesis by Parkinson and Gordon (Source: Parkinson 1999).

The surface of the particles is proposed to be composed of mainly silanol groups [$Si(OH)_2$ or Si–OH], which allow the particles to diffuse over the surface of the aggregate in a process called sintering. This surface movement enables the molecules to reorganize their positions towards thermodynamic equilibrium, usually resulting in a smoothing of the aggregate surface. Sintering has been revealed to be influenced by the factors such as pH and temperature, which may illustrate the differences in frustules morphology observed when a single diatom species is grown under varying conditions (Conley, et al. 1989, Presising 1994).

Although not too much is known about the silica transportation to the SDV, microtubules have been discovered to be associated with the growing SDV (Pickett-

Heaps, et al. 1990). Microtubules associated with the periphery of the SDV localize the deposition of silica within the SDV via the silica-transport vesicles. The order of the microtubules may explain for the complete morphological characteristics of the frustules.

Diatom cell division proceeds with asexual mitotic divisions (Figure 3.6). For many species, the Petri-dish nature of the frustules results in a reduction in size during sequential divisions in one of the daughter cells. Therefore, the diatom populations decrease in mean size over the time. A critical size threshold is reached, typically 30–40% of the maximum size. Below this critical size, the mitotic cell division is not possible. Diatom reproduction can occur several times, ~ 8 divisions, per day, so that a large number of similarly-shaped frustules can be obtained in a short period of time (Parkinson and Gordon 1999, Scala and Bowler 2001). During the division process, two daughter cells forms inside the parent cell. One of them forms in the side of epitheca while the other forms in the hypotheca.

The nucleus of each cell is located in the side of valves and a microtubule center occurs between the nucleus and plasma membrane. SDV is formed in a region between the microtubule center and the plasma membrane. The SDV elongates into a tube, extends perpendicularly and eventually forms a huge vesicle along the one side of the cell. A new valve is formed within the SDV by the targeted transport of silica, proteins, and polysaccharides. During this process, the SDV becomes acidic due to the silica polymerization process (Vrieling, et al. 1999b). Few organic components form a coat around the silica framework, whereas the others are involved in silica deposition. Then, the valve biogenesis is completed and exocytosed by the combination of the SDV membrane (the silicalemma) with the plasma membrane. As a consequence, the inner face of the silicalemma is thought to become the new plasma membrane. Following the separation, the daughter cells can expand unidirectionally along the cell division axis by the biogenesis of girdle bands. These structures are also formed within SDVs in a manner analogous to that described above. The reproduction process explained above is similar for both pennate and centric diatoms. However, the underlying mechanisms controlling these events are not fully cleared (Van Den Hoek, et al. 1997). Although, it has been proposed that much of the early biomineralization process can proceed via physico-chemical space filling of silica (Gordon and Drum 1994), this is certainly not sufficient to explain the exquisite species-specific designs that are ultimately generated.

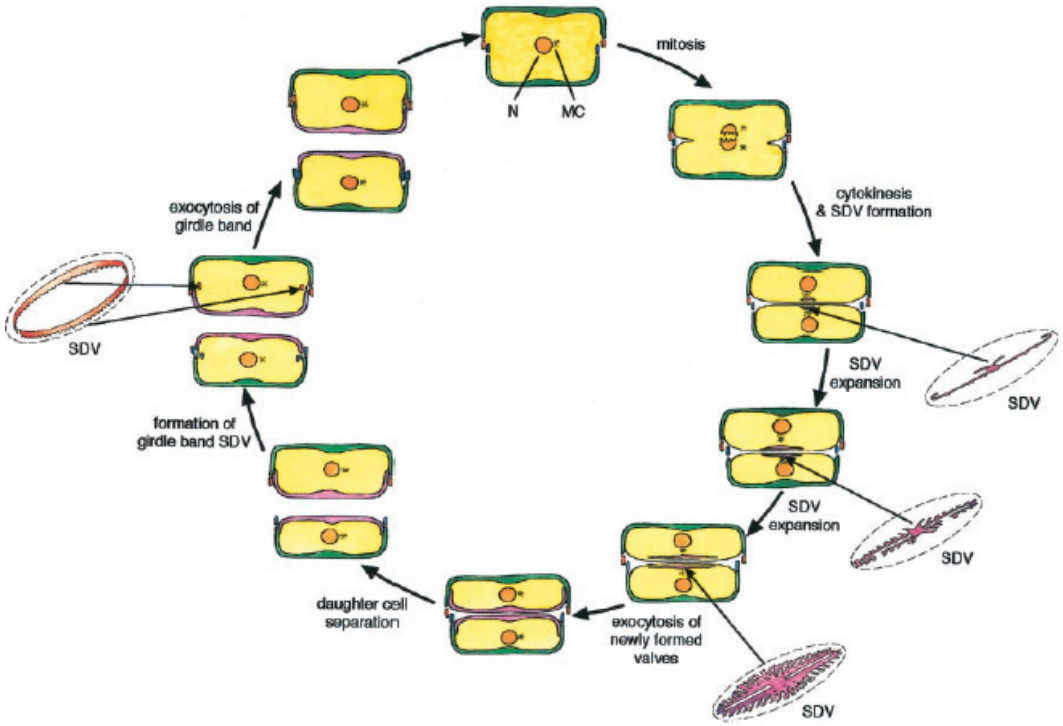

Figure 3.6. Schematic overview of mitotic cell division and hypovalve and girdle band formation (N, Nucleus; MC, microtubule center; SDV, silica deposition vesicle) (Source: Zurzolo and Bowler 2001).

3.2. Diatomaceous Earth

When diatoms cells die and the remnant silica cell wall collect at the floor of the ocean, forming fossils. These fossilized cell walls are called diatomite or Diatomaceous Earth (DE) or Kieselguhr. The porous structure of DE has attracted the attention for the industrial applications. The characteristics that make DE suitable for industrial uses are the low density, high porosity, low thermal conductivity, high melting point (1400°C to 1750°C depending on impurities), solubility only in strong alkaline solutions and hydrofluoric acid, and chemical inertness. Furthermore, DE is an abundant, extremely cheap material and extensively used in sound and heat insulation, chemical reactions as catalyst, sensor components, dynamites, pool water ,beer and wine filtration, absorption and gel filtration (Cai, et al. 2005, Parkinson and Gordon 1999, Scala and Bowler 2001, Stoermer E F 2004, Wee, et al. 2005). The first commercial application and perhaps the most significant use of diatomite were in the production of dynamite, discovered in 1867 by Alfred Nobel. Today, the filtration is the main application of diatomite (73%)

followed by use as a filler (14%). The principal markets for filtration are in alcoholic beverages (beer and wine), sugars, oils and water treatment. Most diatomite mining operations are surface excavations from open pits, with the selection of individual strata of different grades for specific treatment and application. The raw materials are crushed, sorted and dried, and often calcined in the kilns to limit the insoluble impurities and remove the organic material.

3.3. Potential Applications of Diatom Frustules

3.3.1. Filtration

DE is classified into a number of grades according to its permeability. Due to its potential in filtration, DE has been examined for the use in the water purification (Ongerth and Hutton 1997). Diatom frustules were also used in a number of specialized filtration processes such as gel filtration and biosensor filter. As the size of the pores in the medium determines permeability of DE, the filtration properties of DE are dependent upon the packing of the siliceous material. If the properties of diatom frustules that lead to a decrease in the size of inter frustules pores can be identified and selected, it is possible to design a range of diatom frustules capable of acting as filtration media with a potentially increased range of grades. The use of diatoms for filtration would have advantages over DE. Due to the homogeneous nature of the culture used to obtain the siliceous material, the permeability will be constant and will depend upon the species (Parkinson and Gordon 1999).

3.3.2. Microfabrication

Self-assembly 3D nano particle structures attract much attention in many device applications. The use of natural diatom frustules in device applications is limited by the properties of amorphous silica. Therefore, attempts have been made to alter the frustules composition with other suitable materials for a variety of catalytic/chemical, biological, electrical, thermal, mechanical, or other applications (Gordon and Parkinson 2005). Recent studies have shown that silica based diatom frustules can be completely

converted into magnesium oxide based microstructures using the shape preserved gas-solid replacement reactions with magnesium gas (Cai, et al. 2005, Dudley, et al. 2006). This approach has recently been demonstrated for converting diatom frustules into frustules shaped TiO_2 and $BaTiO_3$ (Dudley, et al. 2006, Unocic, et al. 2004). Magnesia based diatom frustules were shown to be converted to nano crystalline zirconia replicas using the oxidation-reduction reaction with zirconium tetrachloride gas (Shian, et al. 2006). Losic et al. (Losic, et al. 2005) fabricated gold structures using the centric diatom frustules as a template. Moreover, intricate micro/macro porous polymeric and ceramic structures obtained by relatively simple processing steps using the diatom frustules as transient bioscaffolds (Anderson, et al. 2000, Gaddis and Sandhage 2004).

3.3.3. Engineering and Medical Applications

The potential engineering and medical applications of diatom frustules have also recently proposed, including metal film membrane, pinpoint drug delivery and nano powder silica (Wee, et al. 2005). The first application is to build a strong, continuous diatom-based membrane that is both permeable and selective. A continuous membrane can be created using a unique process of casting amorphous silica diatom frustules in a continuous metal film. By culturing the diatom frustules, a target pore diameter, frustules size, and chemical affinity can be achieved. They can be used as gas-selective membranes in the equipments such as gas filter masks. The second application involves the magnetization of frustules. For that, diatoms can be cultured in an iron-rich environment. The magnetized frustules can be used in micron-scale electrical motors. Magnetized frustules can also be used to move drug for the treatment of diseases such as cancer. The third application is the processing SiO_2 nano powders from diatom frustules. Frustules are primarily amorphous agglomerations of very small silica particles in the order of a few ten nanometers. Although silica crystals are very strong, the bonds between crystals in diatom frustules are presumed to be weaker than the intra-particle bonds. It was proposed that various techniques including high-energy ball milling, ultra-sonic waves similar to those used to crush kidney stones, and electric and thermal shock can break the relatively weak bonds between the diatom particles. The frustules and purified silica powders obtained from frustules can be used to reinforce composites (Wee, et al. 2005).

3.4. The Mechanical Properties of Frustules

The mechanical properties of individual diatom frustules (*P. viridis*) have been studied recently using atomic force microscopy (Crawford, et al. 2001). The surface was found quite smooth, although high resolution images showed some small-scale granularity. The surface force curves confirmed noncompressiblity of the frustule. The silica in the cross-sections was found in particulate and granular form, in contrast to the smooth material at the valve surface. Images from height data indicated that the silica was loosely packed. Hamm et al. (Hamm, et al. 2003) performed hardness tests on centric and pennate diatom cells using calibrated glass micro needles. The forces necessary to break single, living cells of three representative, bloom-forming diatom species, the centric species *Thalassiosira punctigera*, the *Coscinodiscus granii* and the pennate species *Fragilariopsis kerguelensis* were determined. It was shown that the frustules were remarkably strong by virtue of their architecture and the material properties of the diatom silica. Mechanical strength was found to change with the size of a single species and different species of frustules. *T. punctigera* cells resisted forces up to 260 μN and 180 μN for cells of 50 μm and 100 μm in size. *C. granii* cells (130 μm diameter) were crushed at lower forces (up to 90 μN) than *T. punctigera*. *F. kerguelensis* (730 μN). The elastic modulus of diatom frustule of *T. punctigera* was reported 22.4 GPa and the frustules exhibited fully elastic deformation up to 2.5% strain. The hardness and elastic properties of centric diatom frustules, *Coscinodiscus concinnus*, were determined using nano indentation (Subhash, et al. 2005). The elastic modulus of frustules changed from 0.591 to 2.768 GPa in the center and 0.347 to 2.446 GPa at the locations away from the center. Similarly, frustule hardness varied between 0.033 and 0.116 GPa in the center and between 0.076 and 0.12 GPa away from the center. It was also reported that the porous surface of the frustules made it difficult to extract the mechanical properties accurately at each location. The modulus of N. pelliclosa was found between 7-20 GPa and 20-100 GPa depending on the location, while the hardness ranged between 1 and 12 GPa (Almqvist, et al. 2001). The nanostructure of N. pelliculosa was described as shallow hillocks, 10–20 nm in diameter. The hardness of *Coscinodiscus sp*. species was found to vary between 0.059 and 0.53 GPa and the elastic modulus between 1.7 and 6.51 GPa, depending on the location (Losic, et al. 2007).

The surface area of diatomaceous earth was reported to be relatively high, 22 m^2/g (Hamm, et al. 2003) and it decreased slightly with the applied heat-treatment. The BET specific surface area of kieselguhr was reported to be 3.6 m^2/g (Strzelczyk, et al. 1998). Tsai et al. (Tsai, et al. 2006) found that the BET surface area of diatomaceous earth as 3.81±0.01 m^2/g and this value increased with the etching to 10 m^2/g.

CHAPTER 4

THE CHARACTERIZATION OF FILLER MATERIALS

4.1. Materials, Methods and Characterization of Diatom Frustules

Two different types of diatom frustules were used to investigate as filler in polymeric resins. The first type of diatom frustules was a calcined diatomite (CD), obtained as diatomaceous earth filter material, Celatoms FW-60 grade (Eagle Picher Filtration & Mineral Inc, USA), received from a local vendor. The second was a natural diatomite (ND) received from Alfa Aesar, Johnson Matthey Co., England. The CD frustules were calcined above 1000°C for one hour by the producer. A fluxing agent was usually added during calcination in order to achieve high flow rates. After calcination, the product was milled and classified before it was packaged. The color of as-received CD is light pink, near to white color, while the color of ND frustules is yellowish in color as depicted in Figures 4.1(a) and (b), respectively.

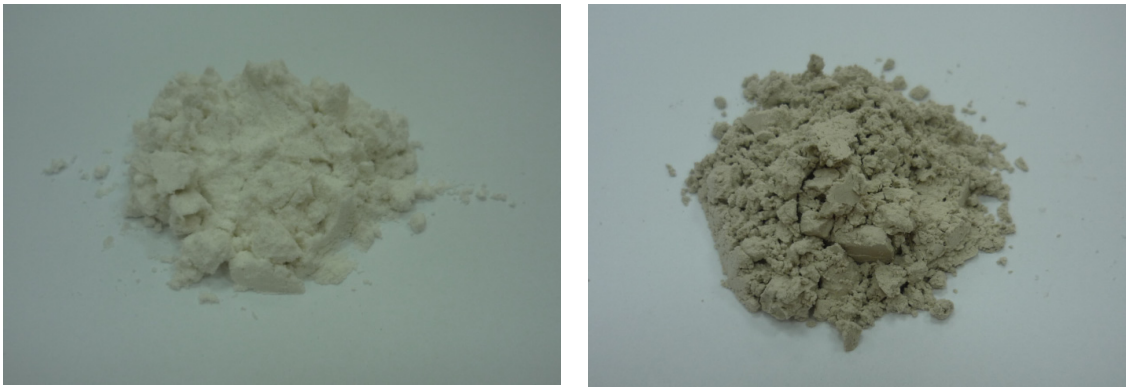

(a) (b)

Figure 4.1. The as-received diatom frustules: (a) calcined diatom frustules (CD) and (b)natural diatom frustules (ND).

Initially, both frustules were dried in a laboratory oven at 120°C for 2 h. Following the drying, frustules were heat-treated for 2 h in a temperature range of 100 and 1200°C at the intervals of 100°C in order to assess the effect of the temperature on the crystal structure of frustules. The morphology of both diatom frustules was

investigated using a XL-30S FEG Philips scanning electron microscope. X-Ray diffraction (X'Pert Pro, Philips, Holland) of the frustules was performed with Cu-Kα radiation (λ=1.54 A°) at 40kV in the 2θ intervals of 5-70°. The chemical composition of frustules was determined using an energy dispersive X-Ray Florescence spectrometer (XRF), (Spectro IQ II). The chemical contents of frustules were determined by Fourier transform infrared spectroscopy, (FTIR 8601 PC spectrometer, Shimadzu, Japan). FTIR analysis was performed in a range of wave number between 4000-400 cm^{-1}. The particle size of as received frustules was determined using a Malvern Mastersizer 2000 particle size analyzer in water.

Calcined frustules or calcined diatomite are of the freshwater type and predominantly composed of *Melosira granulata* (85-90%). This species is characterized by a natural, filter-like, cylindrical shape with a high mechanical strength (EPMinerals 2010). The CD frustules are observed under SEM (Figure 4.2(a)) and found mostly cylindrical in shape. The frustules appear as short tubes with the rows of fine pores, aligned parallel to the tube-axis (centric type). Figure 4.2(a) also proves that the most of diatom frustules in CD belong to the genera *Melosira granulata*, with the short diameters of 5-20μm. One of the ends of the frustules possesses a circular hole with a protruding outer rim, while the other end is closed with either a dense or porous layer and possesses finger-like protuberances as shown in Figure 4.2(a). The finger-like protuberances are observed to intercalate with other frustules forming paired chains of frustules (Tasdemirci, et al. 2008). The pore size of frustules is measured from the magnified SEM pictures and found to range between 200 and 600 nm. ND frustules mostly consist of pennate and centric types of diatoms as depicted in Figure 4.2(b). The pore diameter of ND frustules is measured to change between 200 and 1000 nm depending of the species of diatom frustules. It is also noted few of the frustules were broken probably during the milling operation applied by the producer.

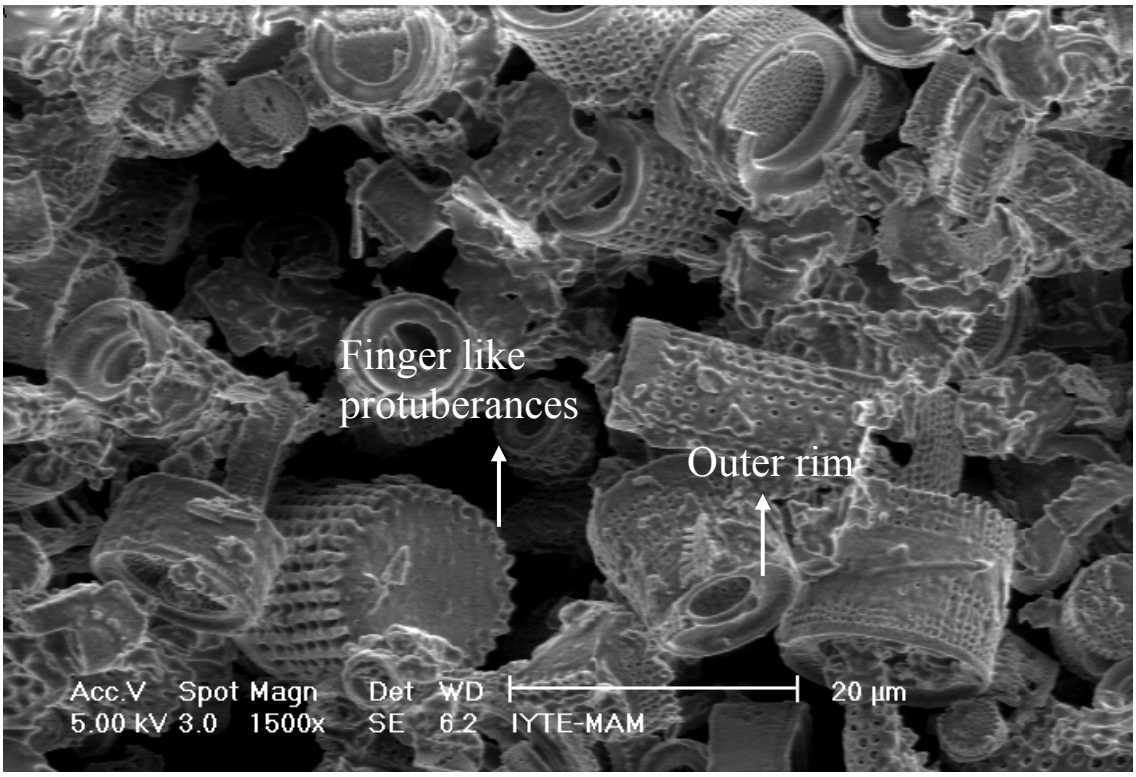

(a)

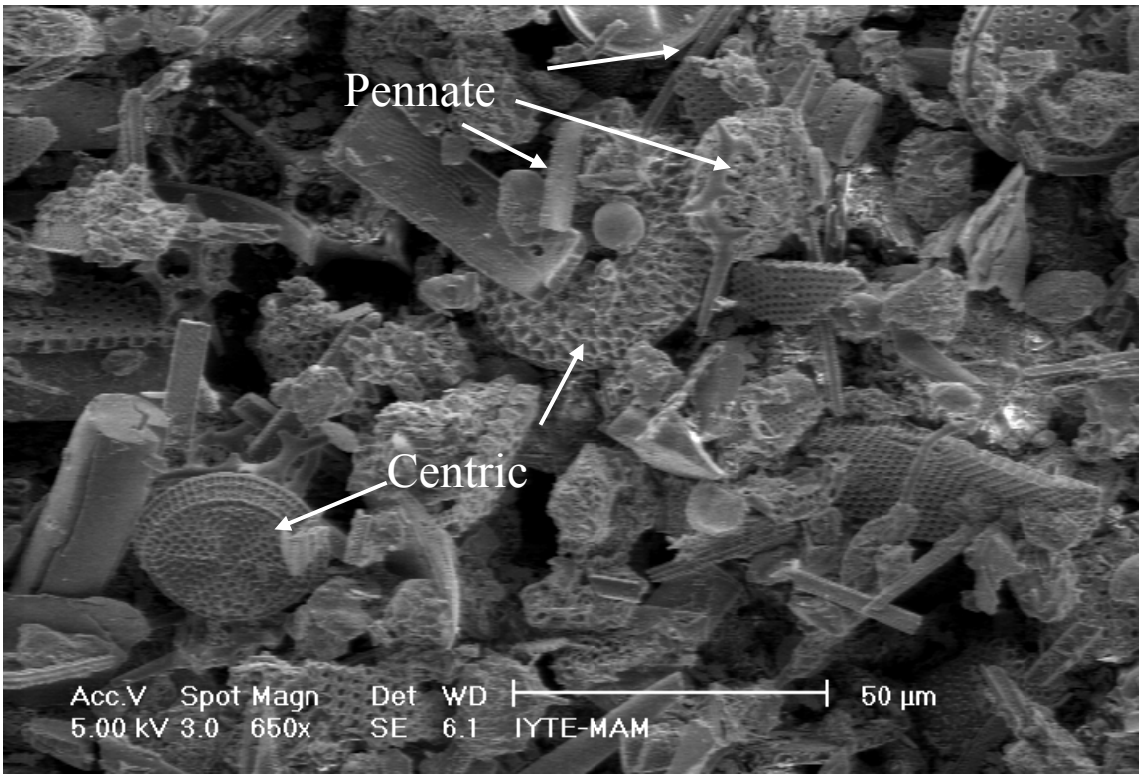

(b)

Figure 4.2. SEM micrograph of diatomites, (a) CD frustules and (b) ND frustules.

The standardless XRF analysis results of CD and ND frustules are tabulated in Table 4.1. Both frustules are found to be composed of silica mineral (88-90%) and small amount of other oxide components. The higher Na content of CD frustule is mostly probably resulted from the flux addition in the calcination process.

Table 4.1 Chemical composition of the frustules.

Constituents	CD (wt%)	ND (wt%)
SiO_2	88.16	90.08
Al_2O_3	5.02	5.53
Fe_2O_3	1.83	1.52
CaO	0.6	0.51
MgO	0.41	1.03
TiO_2	0.19	0.21
Na_2O	2.78	<0.02
P_2O_5	0.02	0.23
MnO	<0.002	<0.002
K_2O	0.031	0.48
Cr_2O_3	0.084	0.089
Loss on ignition	1	

XRD spectrum of the CD frustule is shown in Figure 4.3. The structure is low crystalline cristobalite (SiO_2, Ref. 76-0940), which is tetragonal form of silica. X-Ray diffraction pattern of ND exhibits opal structure (SiO_2, Ref .38-0448), which is hexagonal silica, with quartz (SiO_2, Ref. 82-0511) (Figure 4.4). According to Yuan, et al. (Yuan, et al. 2004), Diatomaceous silica, the amorphous silica with Opal-A structure, exists in the form of frustule in the natural mineral assemblage of diatomite. X-ray diffraction pattern of ND further confirms that the frustules consist of predominantly amorphous silica. CD structure represents the Opal C structure which is a well-ordered form of the silicate mainly in the α-cristobalite. Figure 4.5 shows the XRD pattern of as-received and heat treated CD frustules. The XRD spectra of the heat treated CD frustules between 100 and 1200°C show the same crystalline cristobalite silica peaks with those of as-received frustules. This confirms the stability of the as received CD frustules.

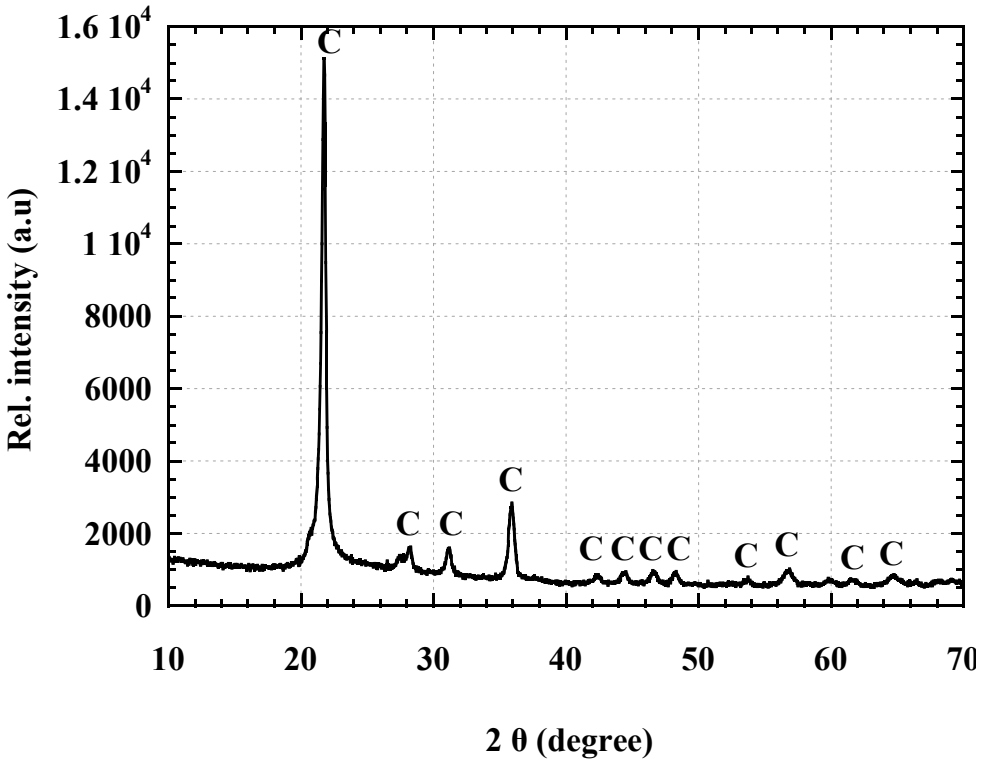

Figure 4.3. XRD pattern of CD (C: Cristobalite,low).

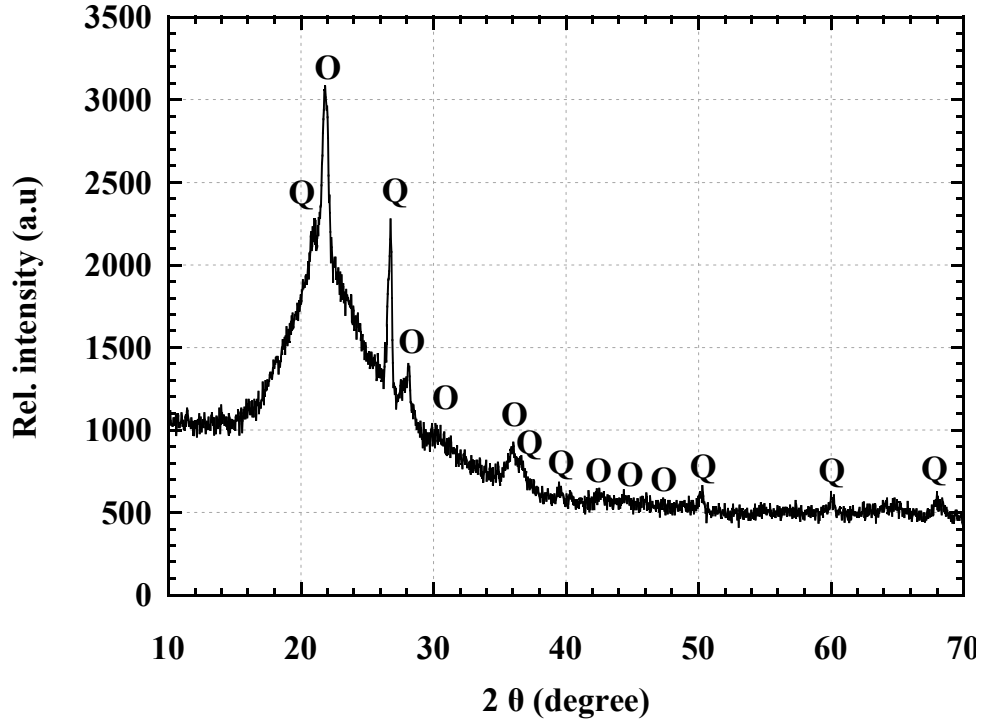

Figure 4.4. XRD pattern of ND (Q: Quartz, O: Opal).

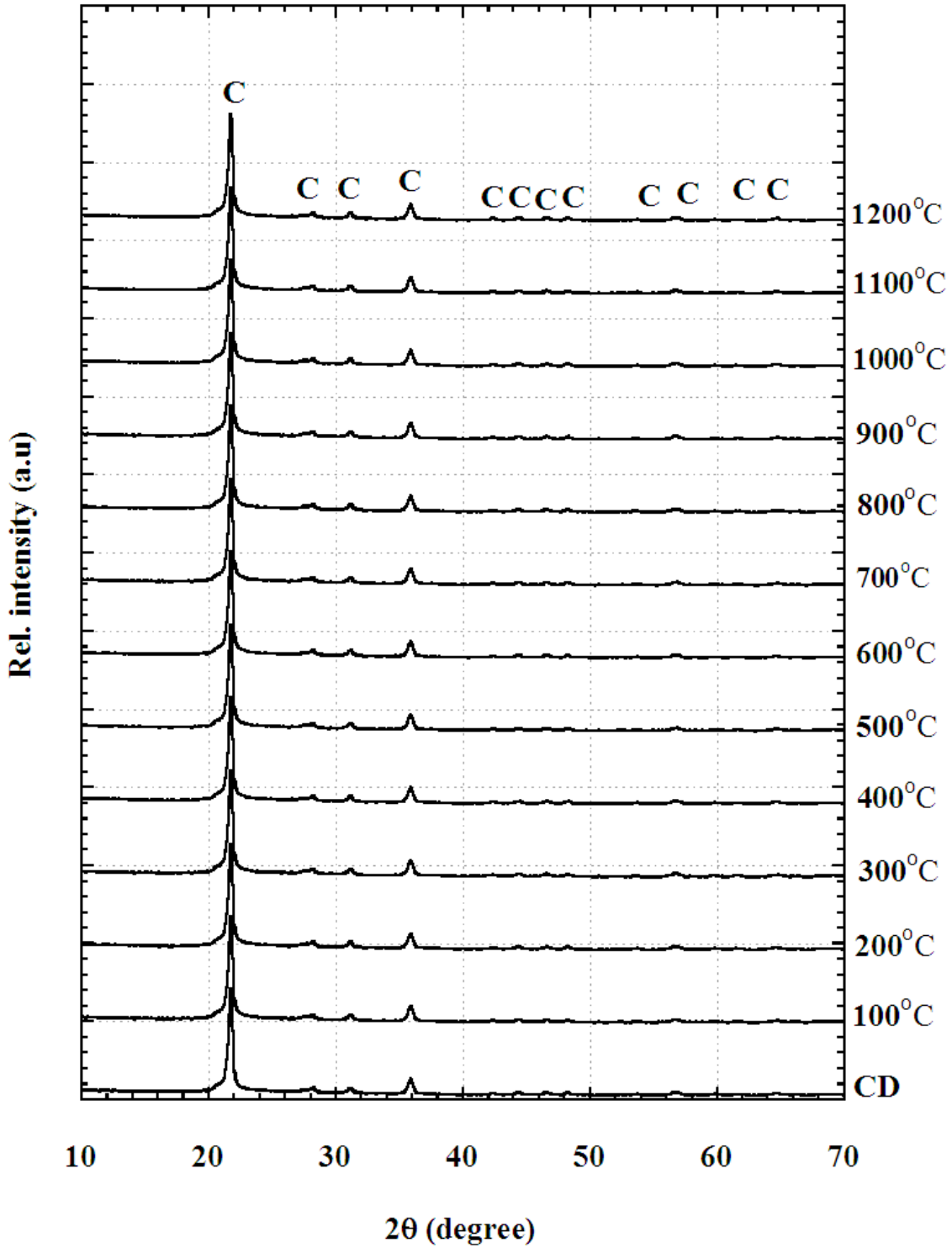

Figure 4.5. XRD patterns of as-received and heat treated CD (C: Cristobalite).

The XRD patterns of as-received and heat treated ND are shown in Figure 4.6. When the heat-treatment temperature of ND frustules increases to 900°C, the peak intensity of quartz at about 2θ=26° decreases and the transformation of amorphous

phase into crystal structure starts (Figure 4.6). The X-ray diffraction pattern of ND heat-treated at 1200°C exhibits crystalline cristobalite phase.

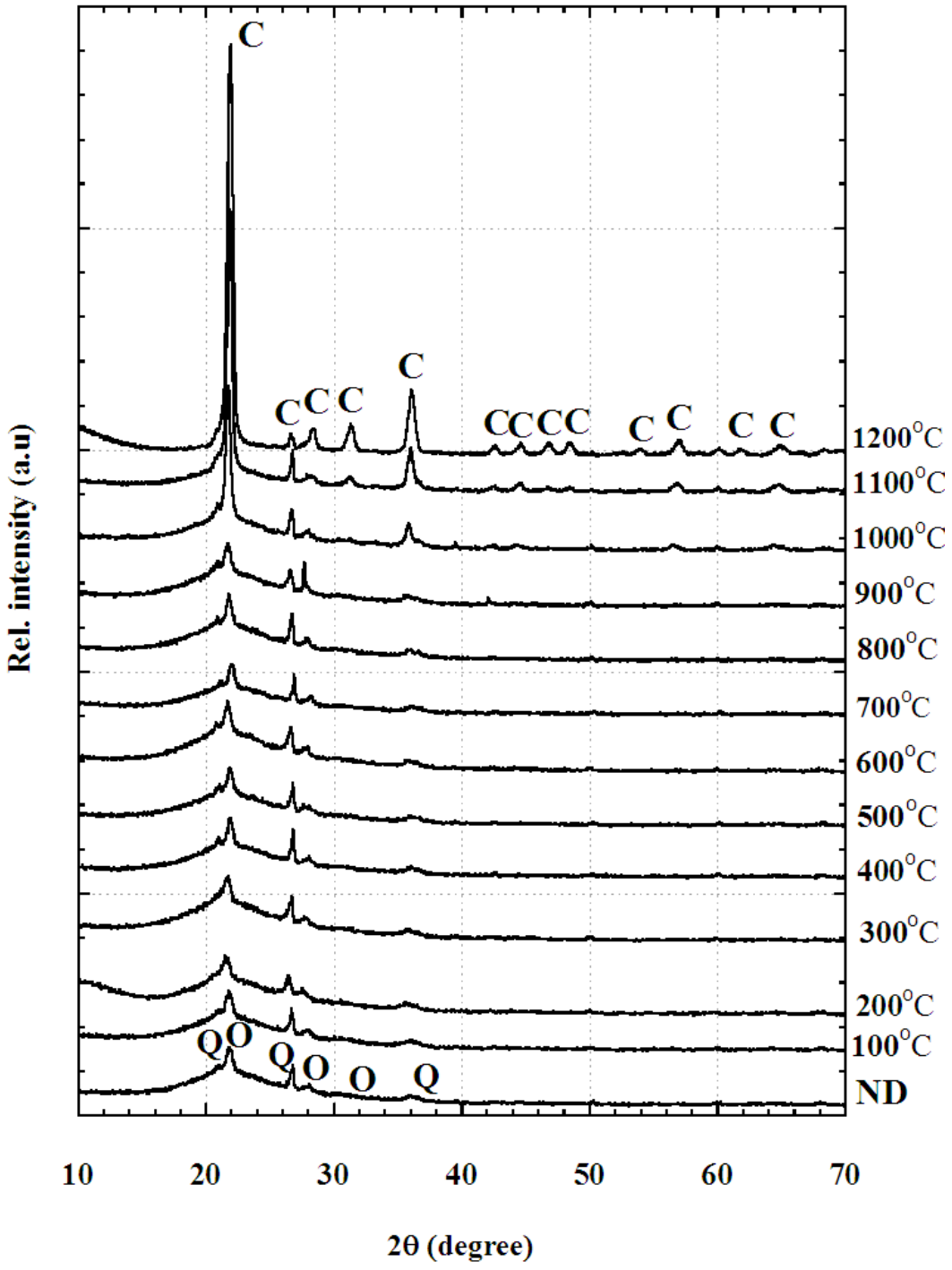

Figure 4.6. XRD patterns of as-received and heat treated ND (C: Cristobalite, Q:Quartz, O: Opal).

The FTIR charts of as-received CD and ND frustules are shown in Figure 4.7.

Both frustules show the same three characteristic broad bands at 1096, 797 and 471 cm^{-1}. The band detected at 1076-1100 cm^{-1} is assigned to Si-O-Si anti-symmetric stretching mode. The adsorption band at 750-850 cm^{-1} represents the symmetric Si-O-Si stretching mode. The wave numbers of 618 and 450 cm^{-1} symbolize the bands characteristic of the Si-O-Si framework. There is one different peak at about 617 cm^{-1} in CD frustules due to its crystal structure.

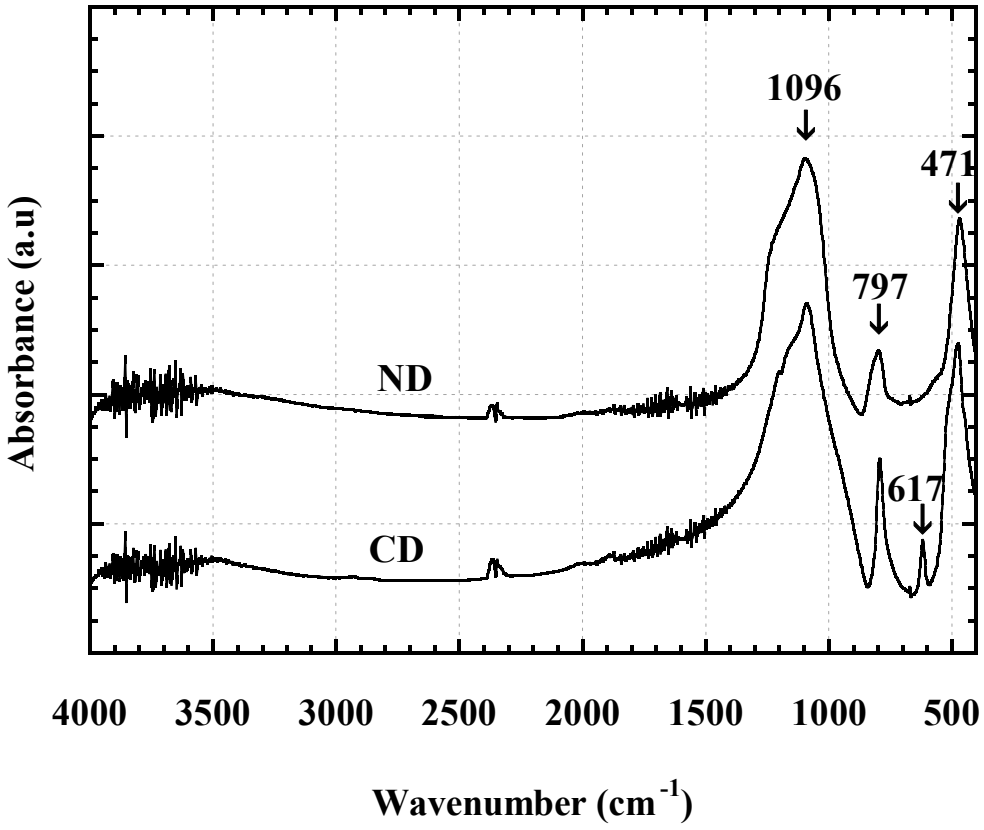

Figure 4.7. FTIR charts of ND and CD frustules.

Figure 4.8 shows the FTIR analysis of as-received and heat treated CD frustules. There is no differences between the characteristic band of cristobalite phase from 400 to 1800 cm^{-1}. In the range from 400 to 1800 cm^{-1}, the spectra of as received and treated ND samples show the same characteristic peaks at 1096, 797, and 471 cm^{-1} (Figure 4.9), which are similar to amorphous silica. In addition to the above three bands, the spectrum of ND frustule treated at 1200 °C demonstrates a new band at 618 cm^{-1}, which indicates the transforms to cristobalite phase (Xiao, et al. 2004).

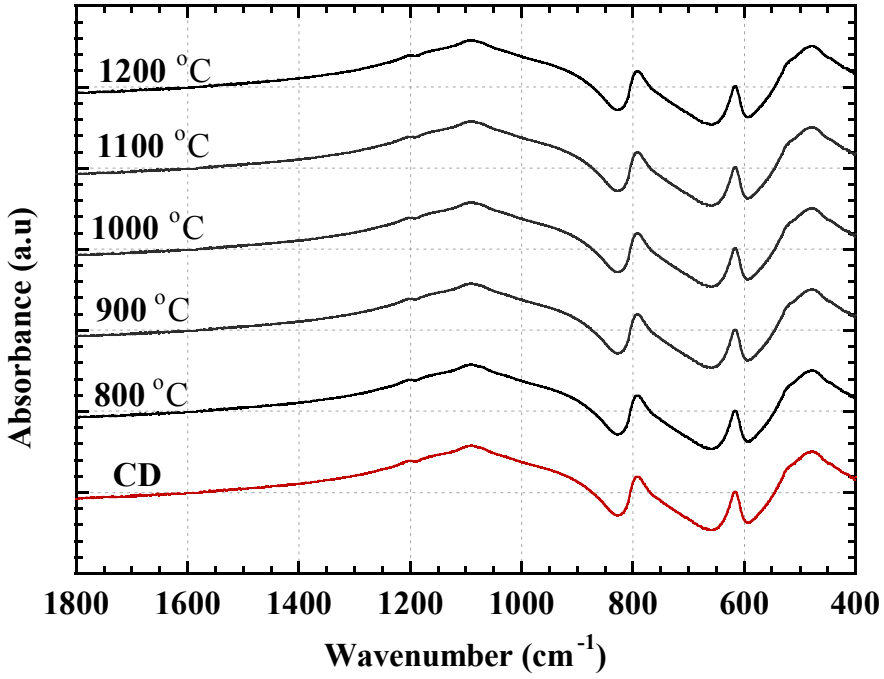

Figure 4.8. FTIR analysis of as-received (red) and heat treated (black) CD frustules.

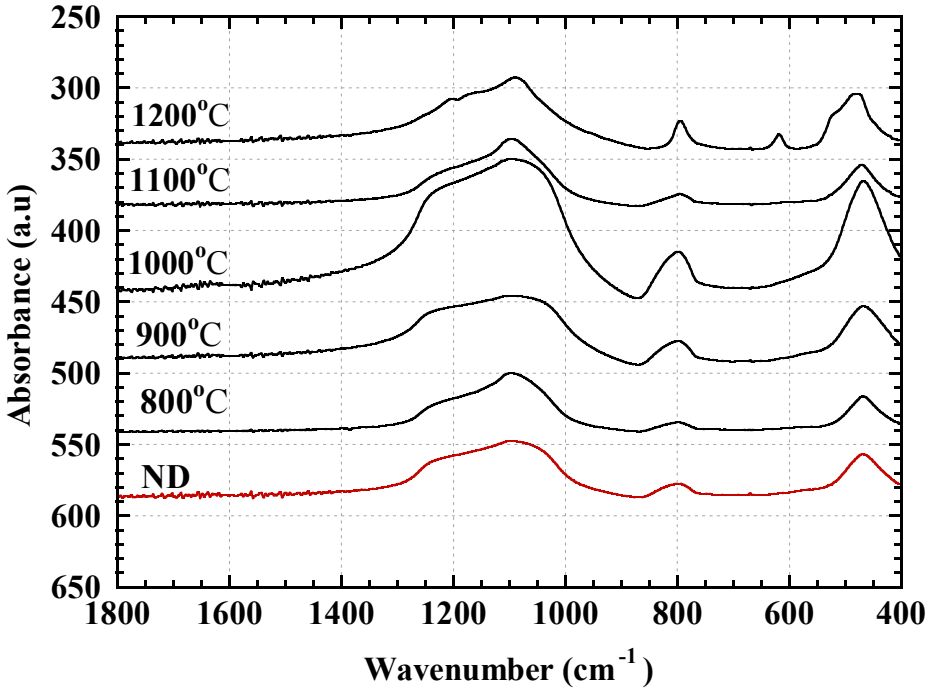

Figure 4.9. FTIR analysis of as-received (red) and heat treated (black) ND frustules.

4.2. Particle Size Measurements of Frustules

The particle size distributions of CD with or without ultrasonic dispersions are shown in Figure 4.10. Ninety percent of the CD frustules diameters are seen in the same figure less than or equal to 113.7 μm, 10% is less than or equal to 12.4 μm. The mean particle size is 42.6 μm without dispersion. After the application of ultrasonic treatment for 2 min, the mean size of CD frustules decreases to 37.5 μm and 90% of CD frustules diameters is reduced to 84.8 μm and 10% to 9.8 μm. The reduction in mean size is due to the elimination of the agglomeration of frustules. The size distribution of CD is considered to be nearly mono model although the existence of few percentages of relatively small particles. The mean particle size of as-received and dispersed ND are shown in Figure 4.11. Ninety percent of the ND frustules diameters are less than or equal to 54.4 μm, 10% is less than or equal to 3.9 μm. After the dispersion, the mean size of ND decreases from 16.8 to 15.1μm, and 90% of ND frustules diameters are reduced to 44.4 μm and 10% to 3.6 μm. Similar to CD frustules, small percentage of small ND particles is found in size distribution.

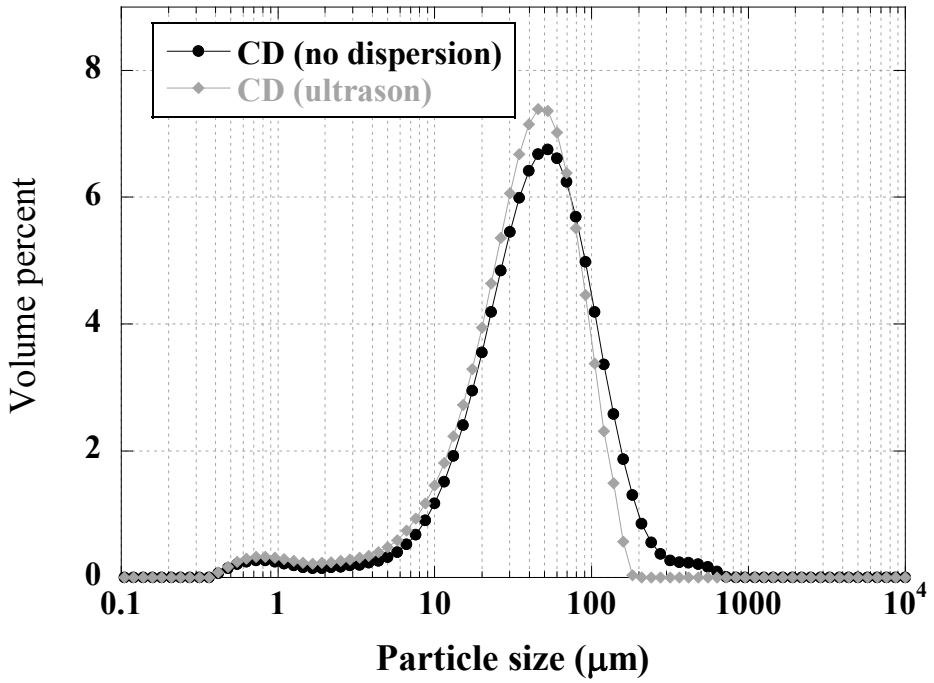

Figure 4.10. The particle size distribution of CD.

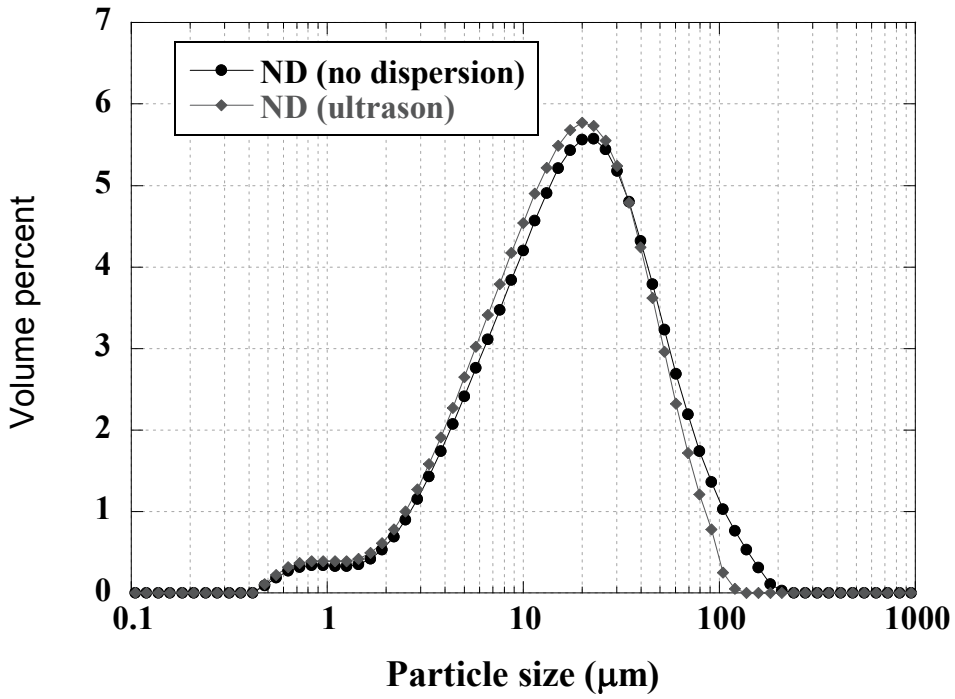

Figure 4.11. The particle size distribution of ND.

CHAPTER 5

SILICA POWDER PROCESSING FROM FRUSTULES

There different processing routes were applied to process silica powder from diatom frustules. These included (i) leaching the frustules directly in HF, (ii) incorporating thermally treated frustules in to the liquid nitrogen and (iii) ball milling. The acid leaching was performed on ND and CD frustules at 1N hydrofluoric acid concentration for one hour to assess the effect of HF on frustules. Before leaching, ND frustules were heat treated at 600^{o}C for 2 h. Amorphous ND and CD frustules were treated at different HF concentrations (1, 2, 3, 5, 7 and 9 N) for 7 days for distinct etching times (15 min, 30 min and 1, 24, 72, 120, 168 h). The solution containing frustules and HF was prepared as 1/10 frustules and HF ratio (g/mol) in the polypropylene (PP) plastic bottle at ambient temperature. The solution was filtered in a vacuum filter flask and washed with deionized water to remove the ions and other residues. The resulting solid was finally dried at 110 ◦C for 2 h, and stored in the desiccators after drying. Thermal treatment was performed to determine the resistance of the frustules to sudden changes in temperature. The natural diatom frustules were heated to temperature in the range of 700 -1200°C for about half an hour and then plunged into the liquid nitrogen. Finally, the frustules were dried and examined by using SEM. Both frustules were milled with different milling times in RETSCH 200 Ball mill machine. Milling was performed in an agate pot of 125 ml capacity using 10 mm diameter agate balls. The frustules/ball volume ratio was 1:2. Two types of diatom frustules were crushed at 500 rpm for different grinding time (15 min, 30 min and 1, 2, 3, 4 and 5 h). The particle size of all grinding powders was dispersed with ultrasonic treatment and measured with Malvern Mastersizer particle size measurement equipment.

5.1. Acid Leaching

SEM micrographs of untreated CD frustules and treated frustules (1N and one hour leaching) are shown in Figures 5.1(a) and (b), respectively. One hour acid leaching, as seen in Figures 5.1(a) and (b), result in destruction of frustule wall structure. Figures 5.1(c) and (d) show the surface structure of HF treated frustules at higher magnifications. The chemical treatment revealed the variety of rigid shapes and pores. The silica particles about 200-600 nm in size are clearly seen on the surface of frustules at higher magnifications. The completely open pores and silica particles on the surface of frustules are seen in Figure 5.1(e). The dissolution of the frustule initially occurs between the grain boundaries.

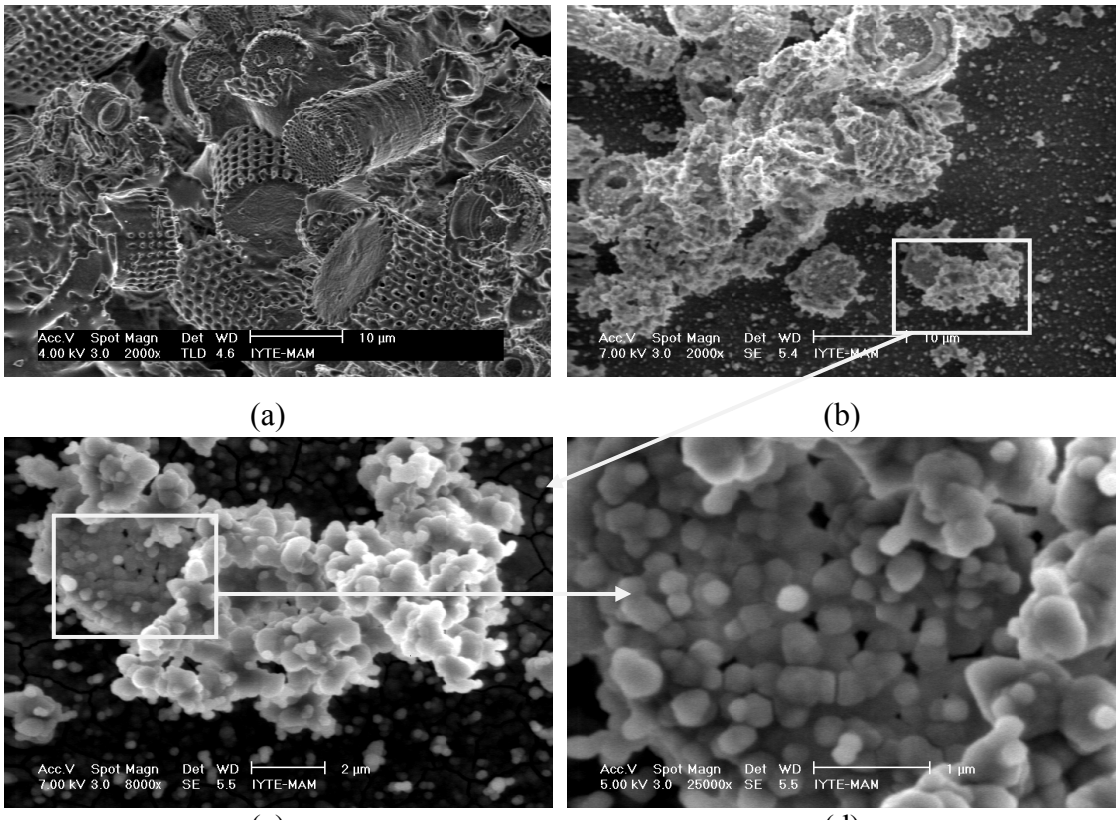

(a) (b)

(c) (d)

Figure 5.1. SEM micrographs of CD frustules (a) before leaching, (b), (c), (d), (e) and (f) after 1N HF leaching for 1hour **(cont. on next page).**

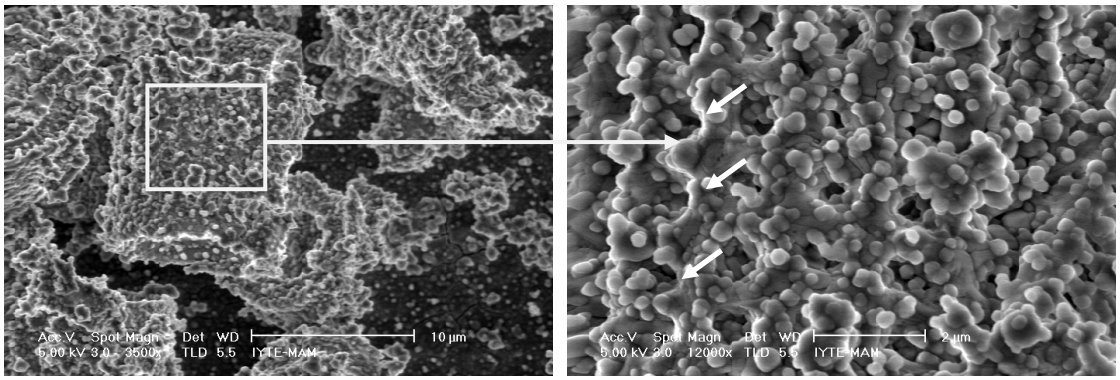

(e) (f)

Figure 5.1. **(cont.).**

Figure 5.2(a) shows the ND frustules before acid leaching and Figures 5.2(a-h) after one hour HF leaching. As seen in Figures 5.2(a-h) acid leaching has less effect of the dissolution of the ND frustules than CD frustules. However, acid leaching is seen to increase the surface roughness of ND frustules by forming 10 nm to 100 nm pores on the surface (Figures 5.2(d) and (h)). It is believed that the pores are formed as a result of dissolution and/or separation of the individual silica particles from the surface.

The SEM pictures of ND frustules exposed to different HF concentration for seven days are shown in Figures 5.3(a-h). As seen in Figures 5.3(a-h) a results, ND frustules exhibit more rough and irregular surface structure with increasing HF concentration. At increasing HF concentrations a large attack on the exterior surface and interior pore wall are seen. HF significantly etches toward the inside the existing pore structure in diatom frustules due to their high content of silica. HF leaching effectively creates new pores and increases the pore properties. This phenomenon was also previously reported (Tsai, et al. 2004).

The mass loss of ND with HF concentration and leaching time are shown in Figures 5.4(a) and (b), respectively. While the mass loss is about 23% with increasing etching time, this value increases to 90% with increasing HF concentration. This observation shows a good agreement with the SEM observations as the surface area of modified frustules is rougher and larger. These results prove that HF concentration is more effective parameter to mass loss of ND frustules than leaching time.

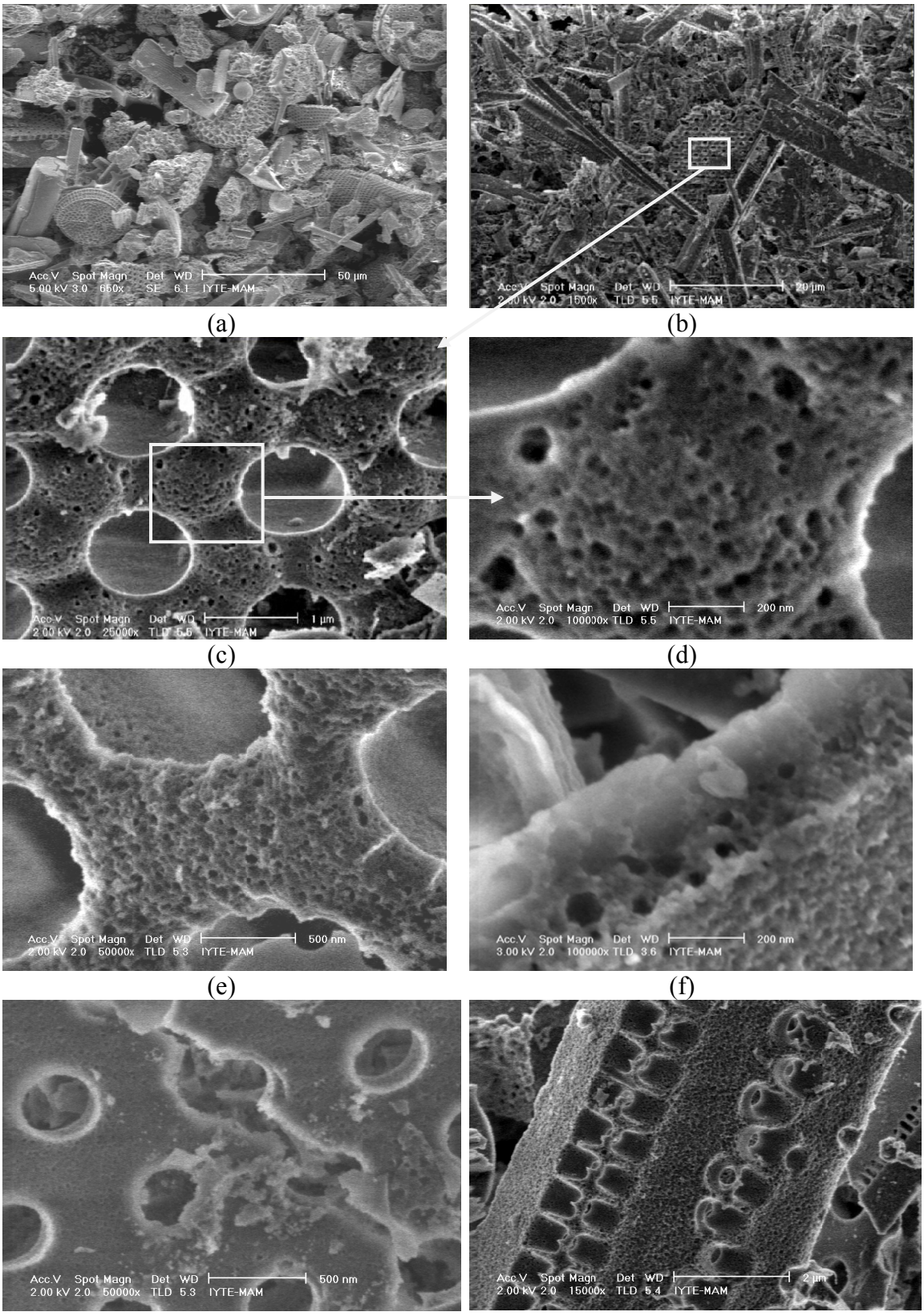

Figure 5.2. SEM micrographs of ND frustules (a) before leaching, (b), (c), (d), (e), (f), (g) and (h) after 1N HF leaching for 1hour.

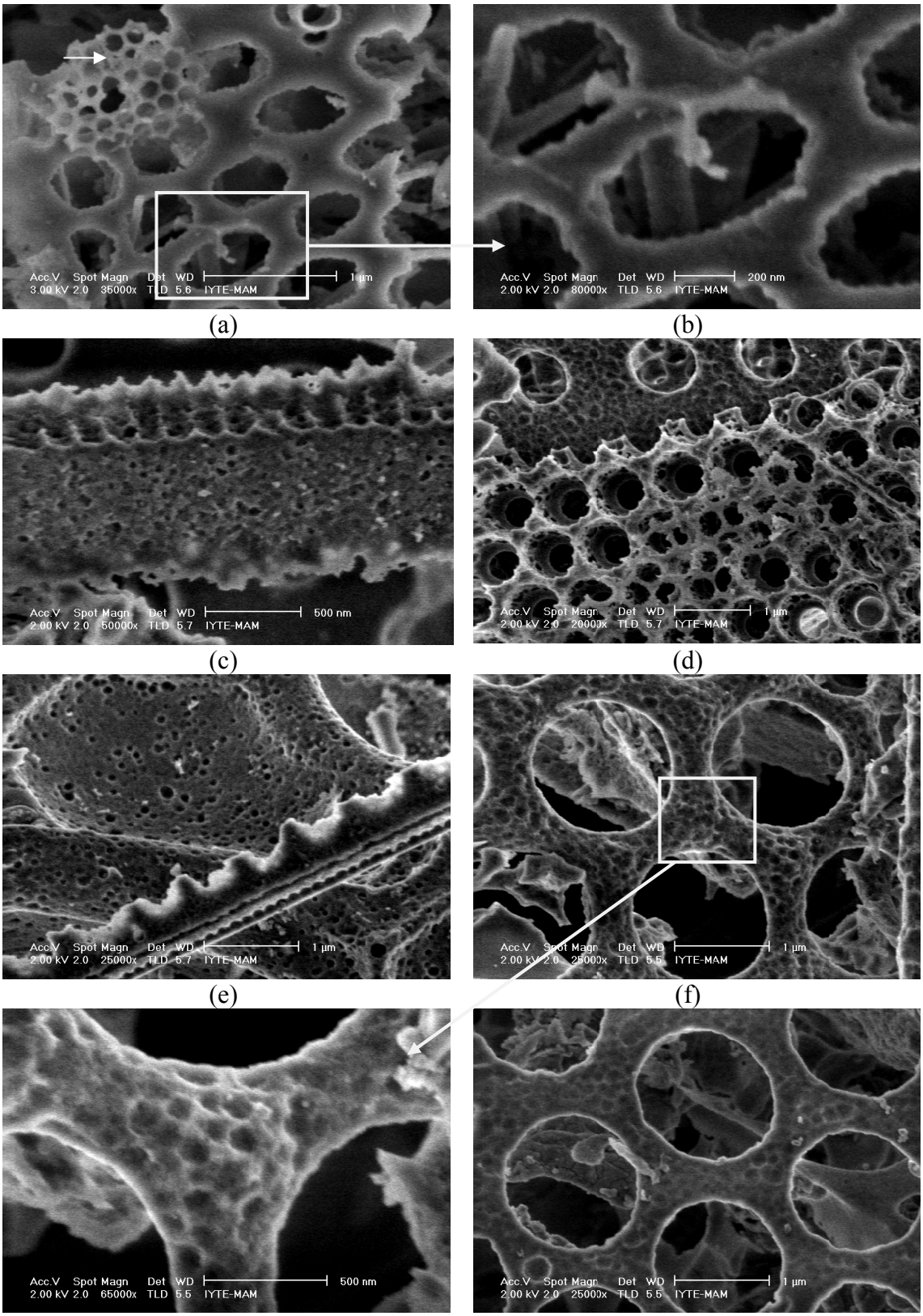

Figure 5.3. SEM micrographs of ND frustules with treated (a), (b) 1N, (c) 2N, (d), (e)3N, (f), (g) 5N and (h) 9N HF for 7 days.

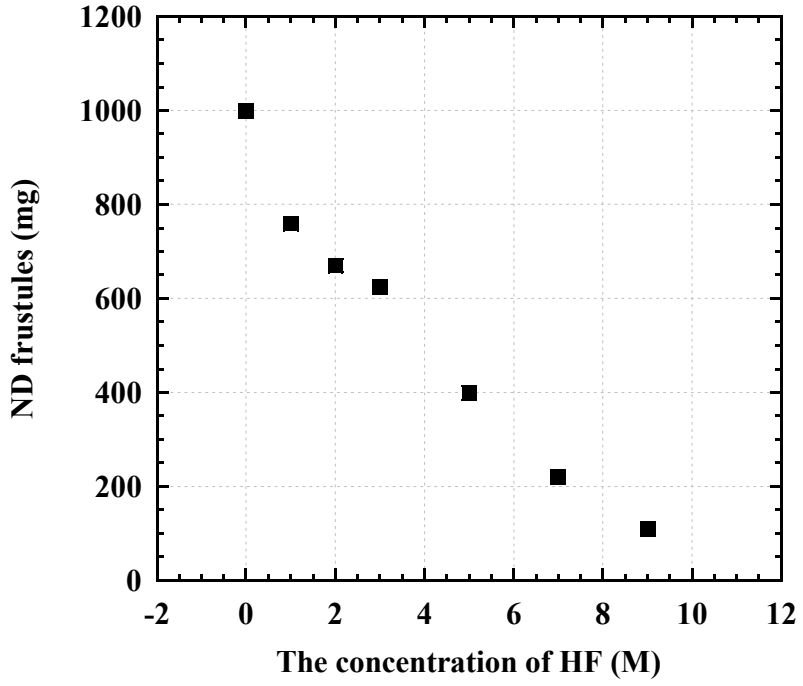

(a)

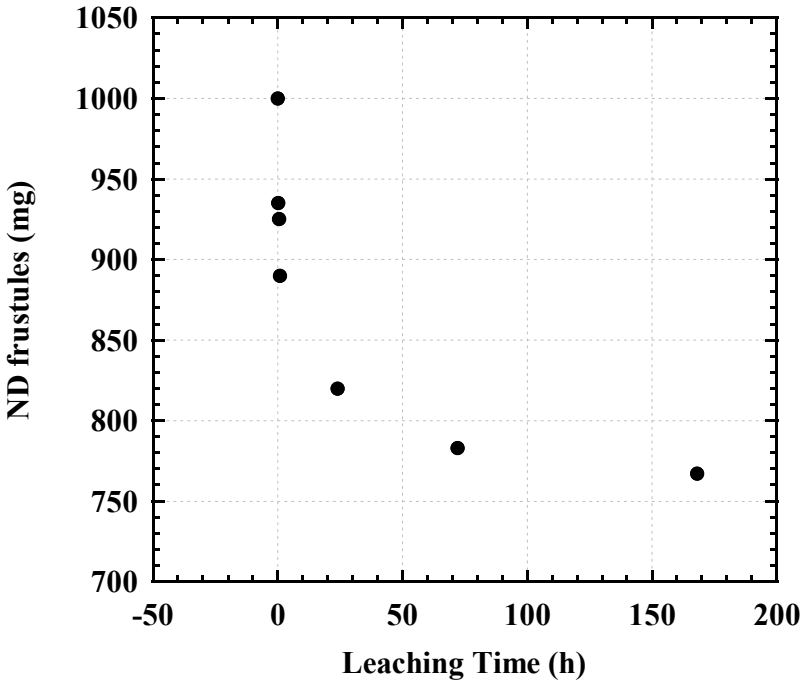

(b)

Figure 5.4. The mass loss of ND (a) at different HF concentration for 7 days and (b) at 1N HF for various leaching times.

5.2. Thermal Treatment

The numbers of cracks between the pores are generally seen in ND samples after the thermal shock (Figures 5.5(a-d)). However, the original geometry of the pores is preserved after the thermal shock. The SEM micrographs of ND frustules quenched from 700°C show that the porous valve structure of frustules are more affected from the thermal shock than the girdle band structure (Figure 5.5 (b)).

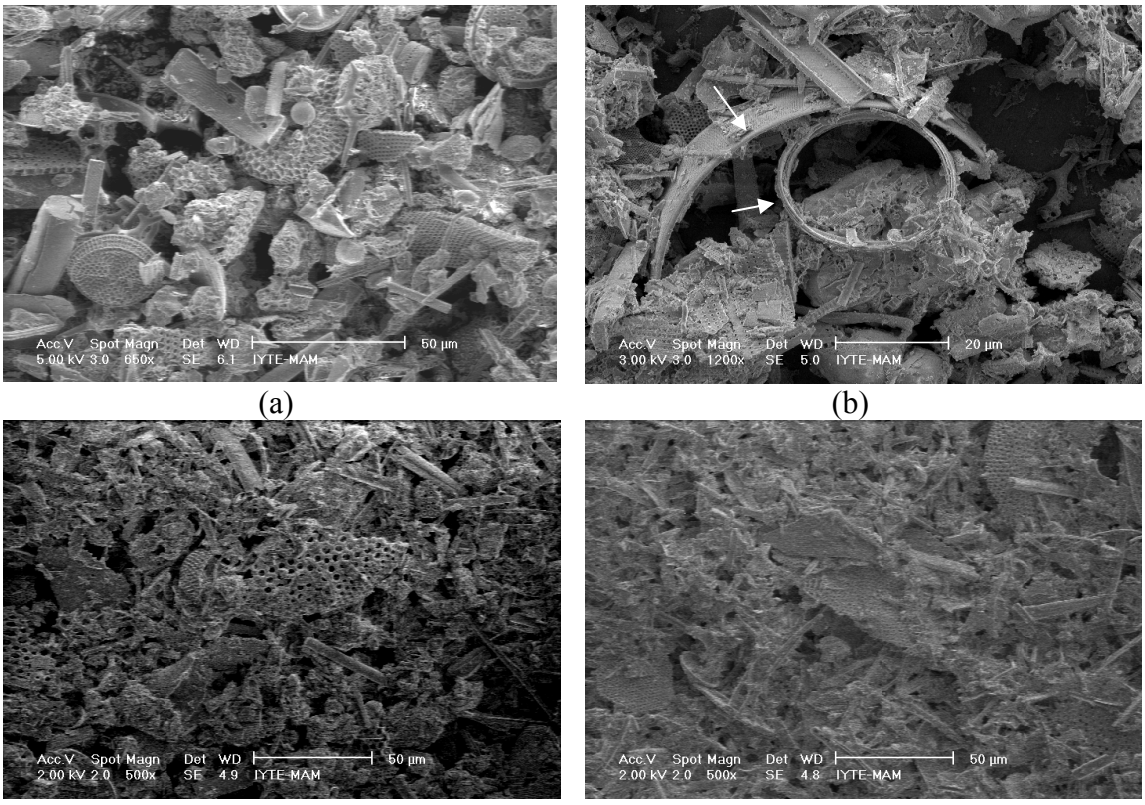

Figure 5.5. The ND frustules (a) as received and thermal shocked from (b) 700°C, (c) 800°C and (d) 1200°C.

The crack propagation is seen in Figures 5.6(a) and (b) for ND frustules quenched from 800°C. Despite the absence of plastic deformation and the smooth fracture surfaces of the broken frustules, the cracks are seen to propagate between pores the pores of ~400nm as seen in Figures 5.6(a) and (b). In ND frustules heated to 1200°C, the smoother surfaces of the fractured pieces are due to the transformation of the amorphous structure into cristobalite structure (Figures 5.6(c) and (d)). The effects of heat treatment temperature on the structure of the frustules are shown in Figures

5.7(a-d). Although no transformation is seen at 900°C (Figure 5.7(a)), the heat treatment at 1200°C results in smother surface and the appearance of grain boundaries Figures 5.7(b-d).

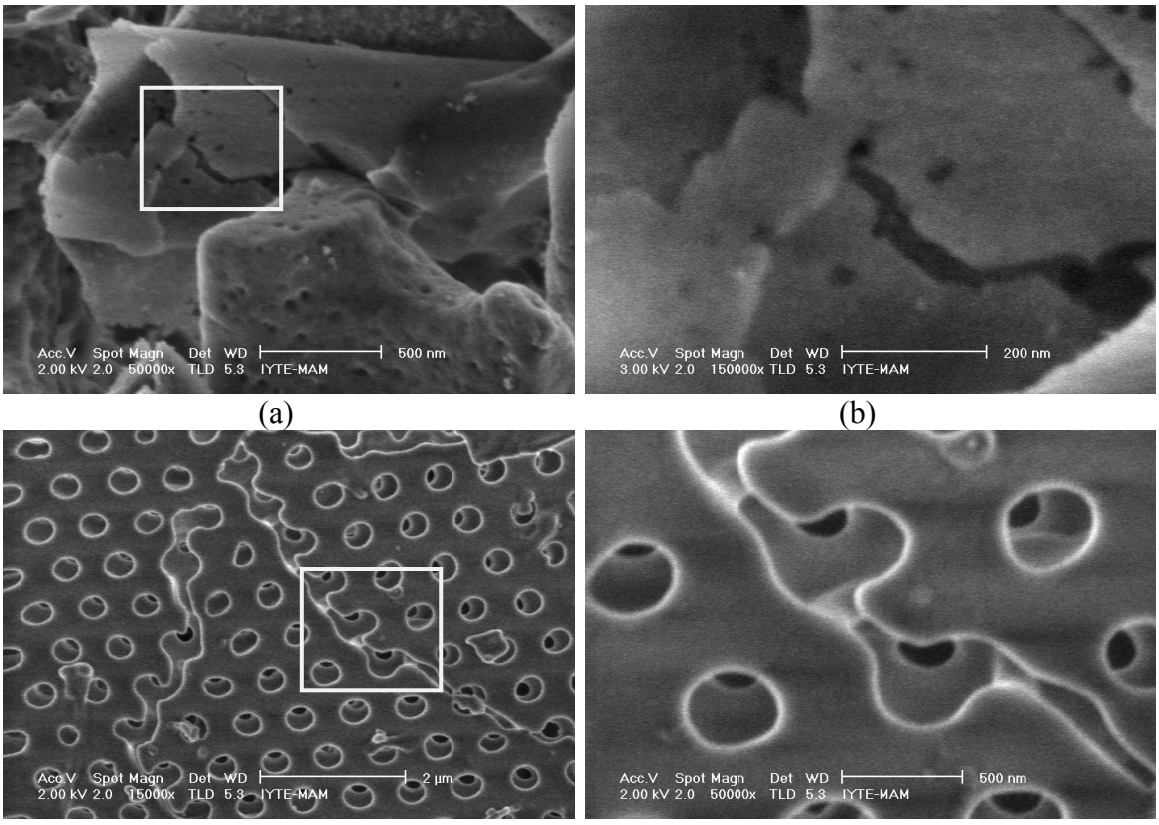

Figure 5.5. The crack propagation in ND frustules quenched from (a), (b) 800°C, (c) and (d) 1200°C.

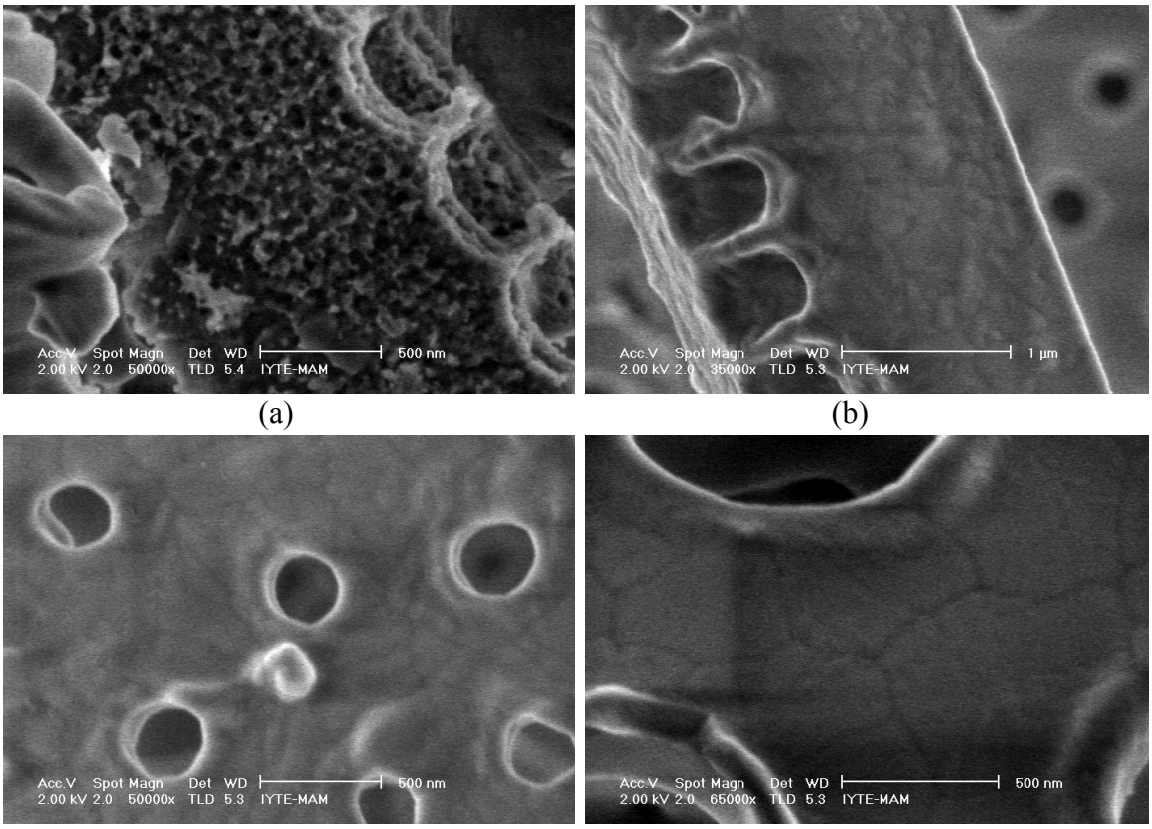

Figure 5.6. The surface of ND frustules heat treated at (a) 900°C, (b), (c) and (d) 1200°C.

5.3. Ball Milling

The particle size distribution of as-received frustules is previously given in Chapter 4. The comparison of the particle size distribution of both frustules is shown in Figure 5.8. The mean sizes of CD and ND are 15.1 and 37.5 µm, respectively and both frustules have relatively large frustules pieces. The effect of ball milling time at 500 rpm on particle size distribution of ND and CD frustules are shown in Figure 5.9 and Figure 5.10. The reduction of mean particle size for both frustules continues with the increasing grinding time. The mean particle size of ND decreases from 15.1 µm to 4.9 µm after one hour milling, and the particle size changes vary between 1.4 and 13.9 µm. The particle size distribution ranges between 1.2 and 12.9 µm and 1.3 and 14.9 µm for 2 and 4 h ball milling, respectively. At the end of 10 h ball milling, the particle size distribution ranges between 0.8 and 23.9 µm. The mean particle size of CD frustules decreases from 37.5 µm to 4.6 µm after one hour ball milling. At the end of 10 h ball milling, the particle size distribution ranges between to 0.9-19.1 µm. The mean particle

sizes of ND and CD frustules with 10% and 90% sizes are listed in Table 5.1. The variation of the mean particle size with milling time is further shown in Figure 5.11. The diameter of frustules decreases to below the 12 μm after the 2 h ball milling. With increasing milling time, the distribution ranges increase and the bimodal particle distribution occurs after the milling time of 8 h. The large particles are due to the agglomeration of the silica powder. Powder in the dry state can be in two forms: aggregated (hard bonds between primary particles due to sintering) and agglomerated (particles held by weaker van der Waals forces). When agglomerated particles are added to a liquid, the particles can be separated by overcoming the weaker attractive forces by several methodologies, whereas the aggregated nano particles cannot be separated (Jiang, et al. 2009). Different ultra-sonication techniques (bath and probe) can distinguish agglomerates from aggregates. The bimodal region on the size distribution of the frustules is found to not be eliminated with the ultrasonic treatment. It is likely that the agglomeration of silica powders occurs due to silica powders of high energy such as friction or heat during ball milling.

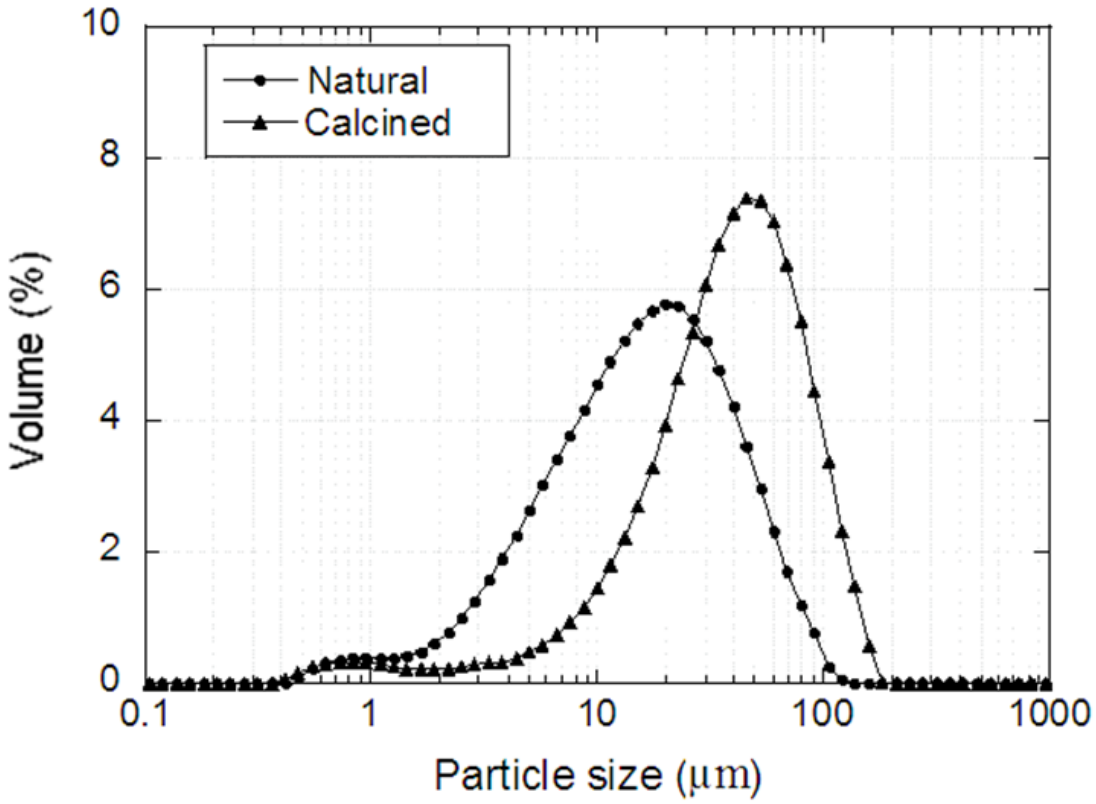

Figure 5.7. Particle size distribution of ND and CD frustules.

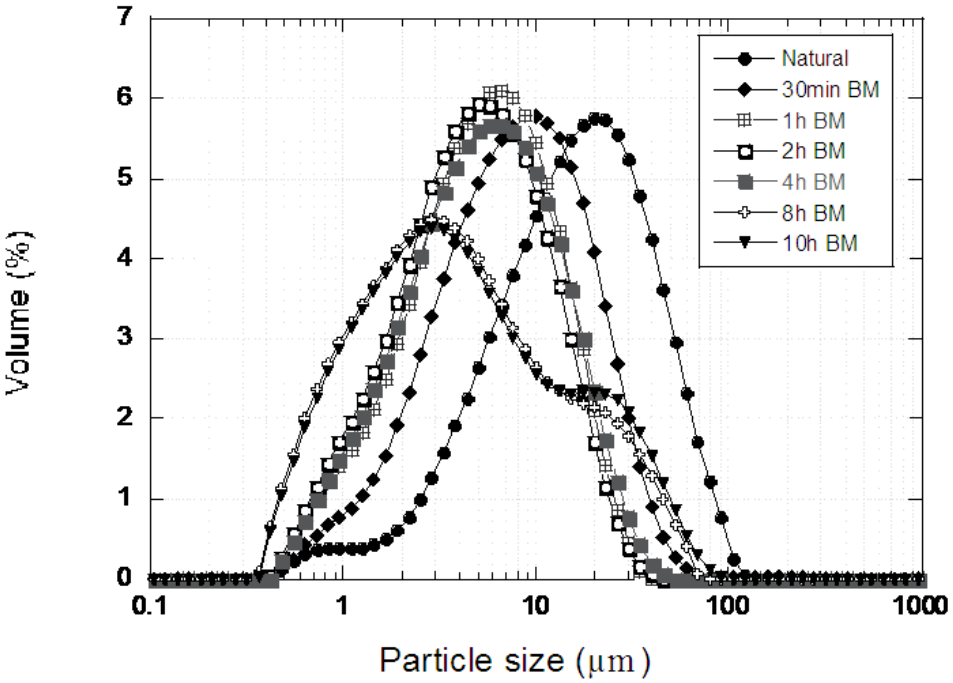

Figure 5.8. The effect of milling time on the particle size distribution of ND.

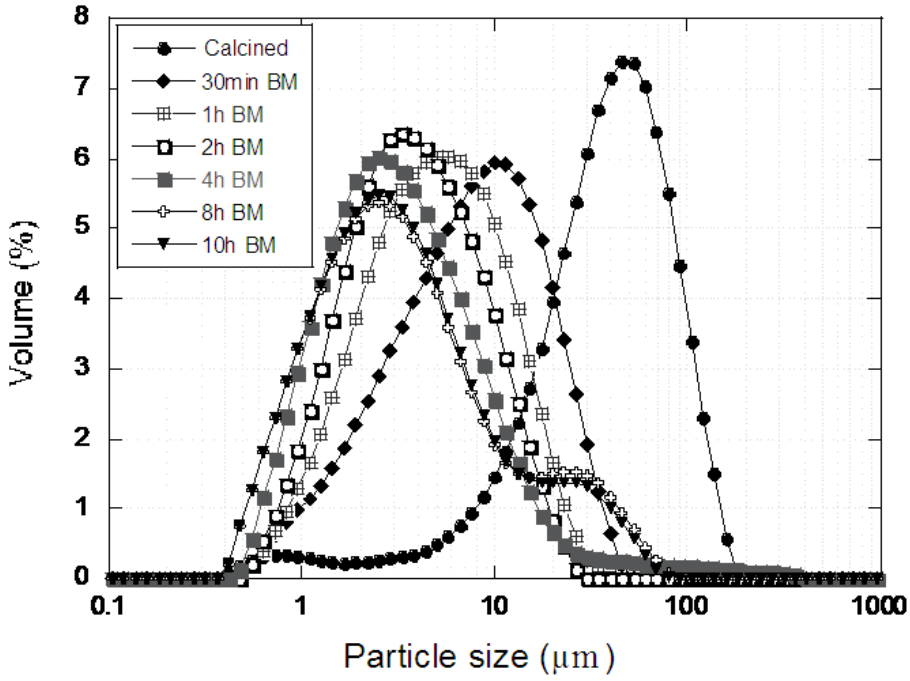

Figure 5.9. The effect of milling time on the particle size distribution of CD.

Table 5.1. The mean particle sizes of ND and CD frustules with milling time.

Ball milling time (h)	Natural diatomite			Calcined diatomite		
	D (0.1) µm	D (0.5) µm	D (0.9) µm	D (0.1) µm	D (0.5) µm	D (0.9) µm
0	3.6	15.1	44.4	9.8	37.5	84.8
0.5	1.7	6.7	18.9	1.8	7.2	19.9
1	1.4	4.9	13.9	1.5	4.6	12.8
2	1.2	4.4	12.9	1.2	3.5	10.1
4	1.3	5.0	14.9	1.0	2.9	10.4
8	0.8	3.3	21.0	0.9	2.8	19.1
10	0.8	3.5	23.9	0.9	2.8	16.5

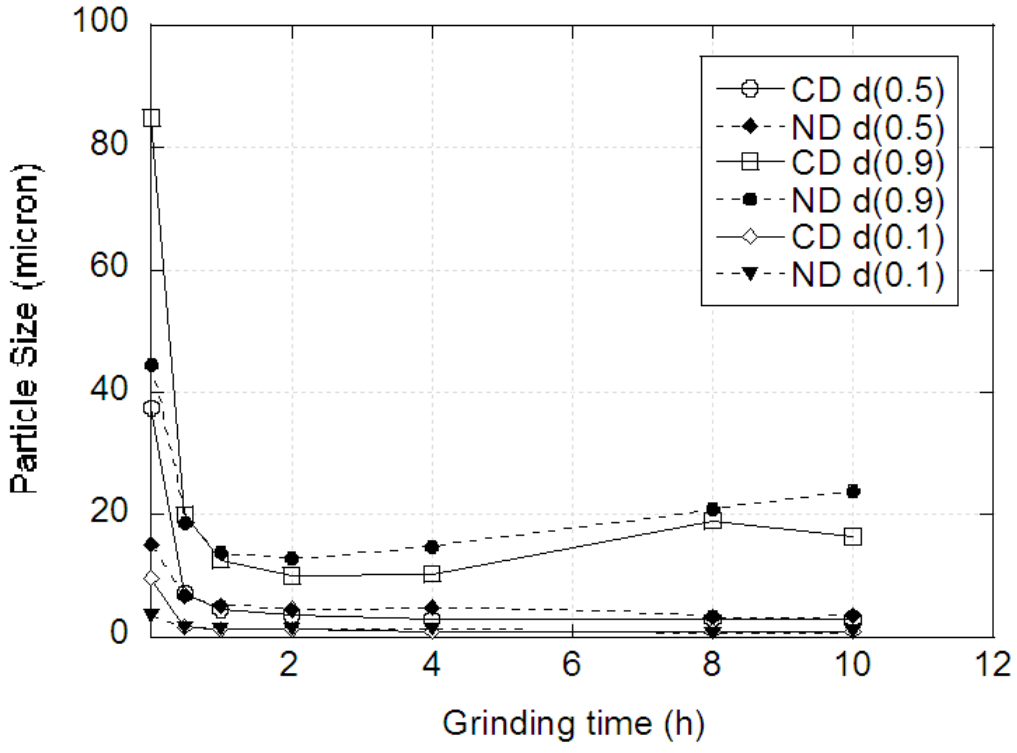

Figure 5.10. The mean particle size and diameter of CD and ND frustules.

Water glass and Darvan C are further used as dispersants. The resultant particle size distribution of ball milled ND and CD frustules with and without dispersant are

shown in Figures 5.12 and Figure 5.13, respectively. The bimodal region disappears and the region below 3 µm becomes larger using both dispersant in both milled frustules. This confirms the annihilation of agglomerated silica particles. The mean size of both frustules after dispersion process is found 2.8 µm for both frustules with a large particle size distribution.

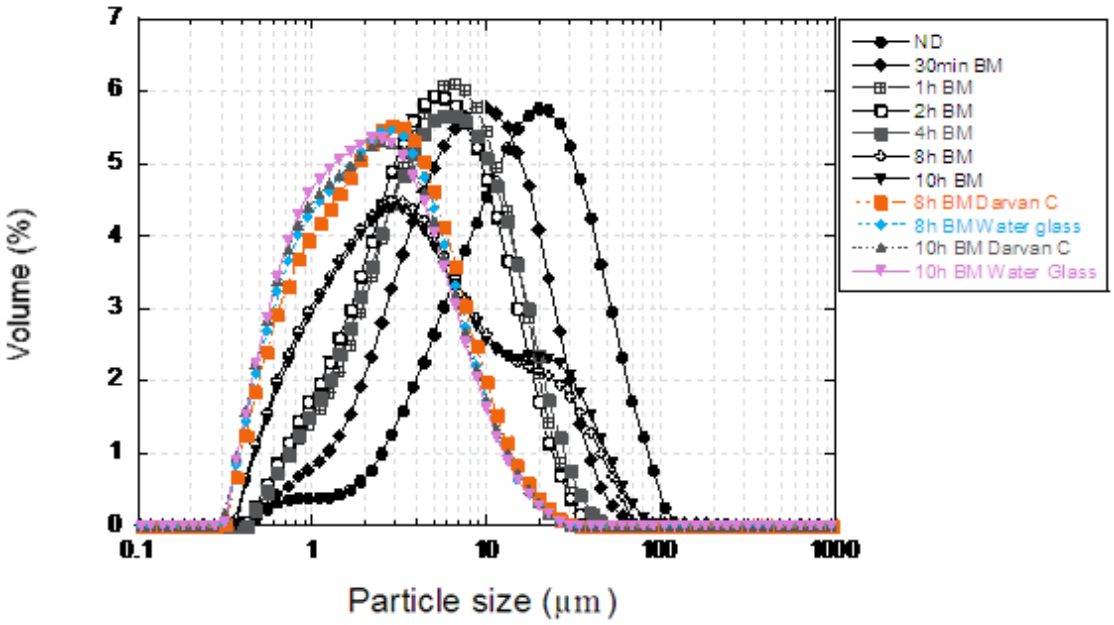

Figure 5.11. The effect dispersants on the particle size distribution of ND frustules.

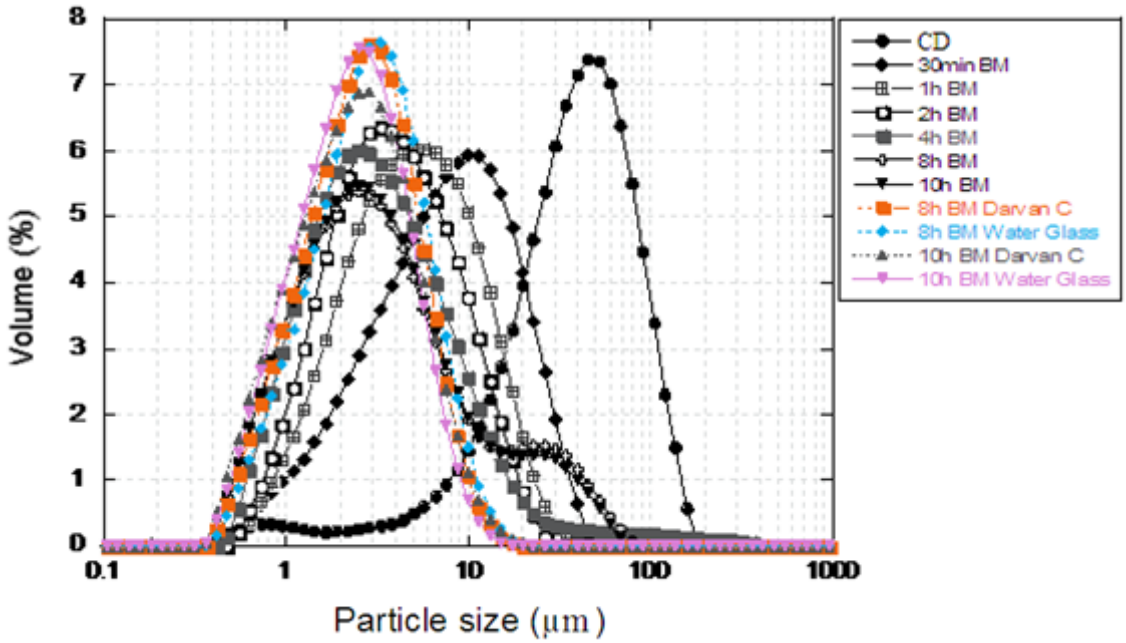

Figure 5.12. The effect dispersants on the particle size distribution of CD frustules.

The SEM images of ball milled ND and CD frustules before and after 2 and 10 h ball milling are shown in Figures 5.14(a-d) and Figures 5.15 (a-d), respectively. The SEM images show clearly that as-received CD and ND frustules crush efficiently with ball milling. However, the particle size measurement shows that the particle size range after 10 h milling is larger than that of 2 h milling. This finding suggests the probability of agglomeration of silica particles with increasingly higher milling times.

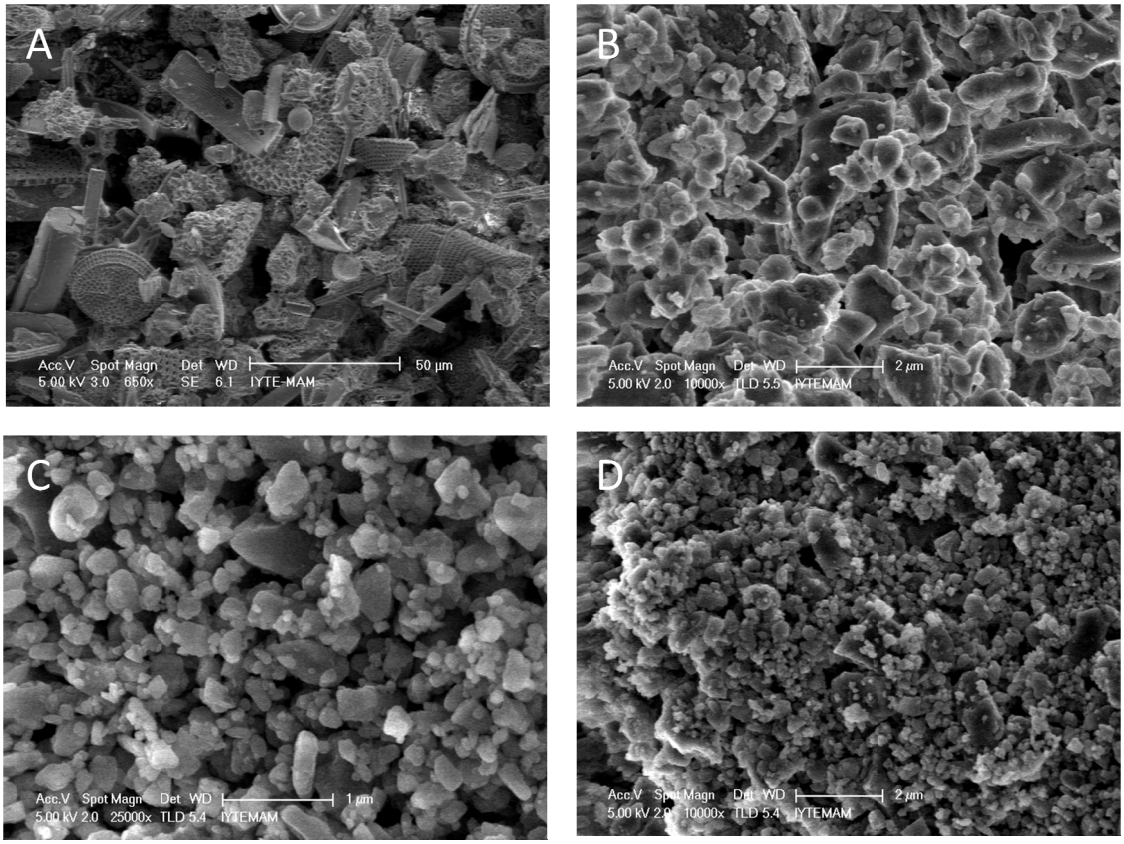

Figure 5.13. SEM pictures of ND frustules (a) before and after (b) 2h, (c) and (d) 10 h ball milling.

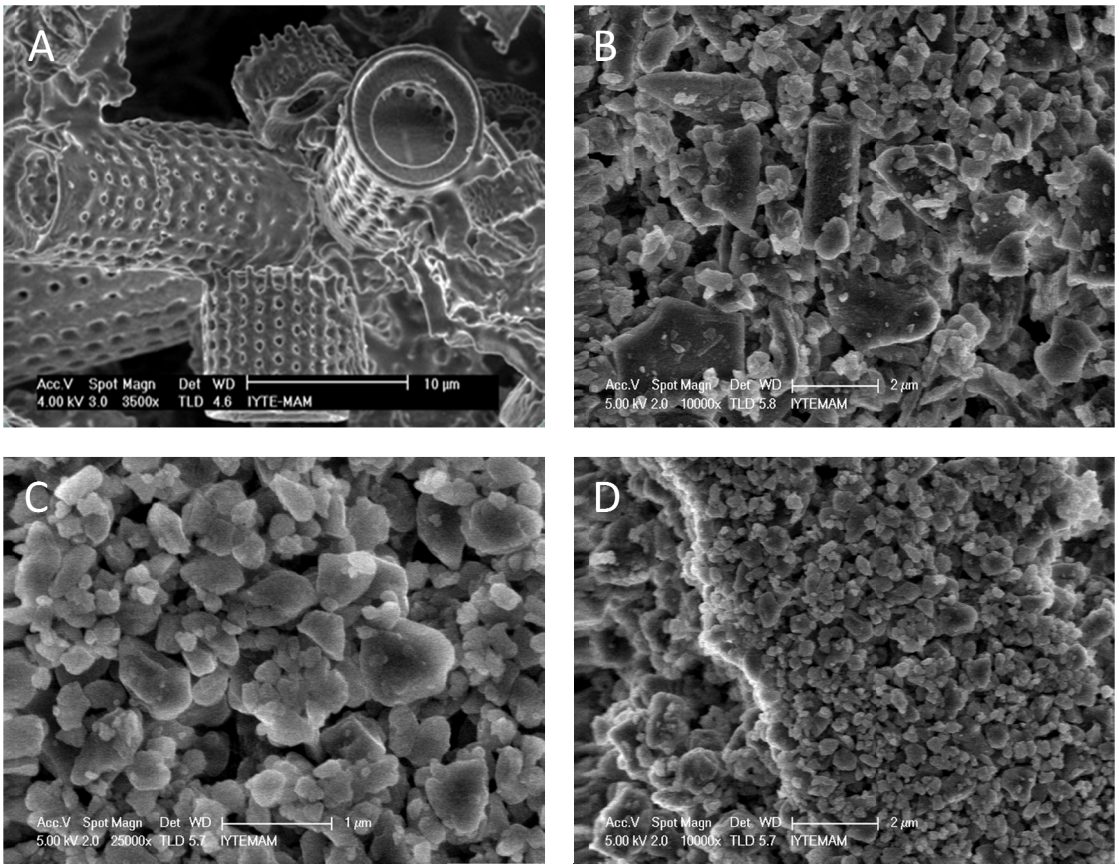

Figure 5.14. SEM pictures of CD frustules (a) before and after (b) 2h, (c) and (d) 10h ball milling.

CHAPTER 6

DIATOM/EPOXY COMPOSITE PROCESSING AND TESTING

6.1. Processing Frustules Filled Epoxy

A Digitial disperser (Ultra-Turrax T 25, IKA® Werke GmbH & Co. KG, Germany) was used to disperse homogenously diatom frustules in epoxy (Figure 6.1). It is well known that the control of curing process is important to achieve the optimum cross-linking. Curing can be achieved at room temperature, but it is usual to use a cure schedule which consists of heating at one or more temperatures. An isothermal time-temperature-transformation (TTT) cure diagram for thermosetting systems as shown in Figure 6.2 has been developed to aid in understanding the cure process and the properties after cure (Hourston 2006). The diagram summarizes the temperature of cure (T_{cure}), the time to gelation, vitrification, phase separation, full cure, and thermal degradation. Before gelation, the material shows a viscous behavior. Gelation causes to slow down macroscopic flow and limits the growth of a dispersed phase. After vitrification, the material passes to the glassy state. The gelation and vitrification curves intersect at T_g, a critical temperature in between T_{g0} and $T_{g\infty}$. At a temperature above T_g, gelation occurs before vitrification, while below T_g vitrification occurs first. The vitrification curve is generally S-shaped, passing through a maximum and a minimum in vitrification time when the temperature is raised.

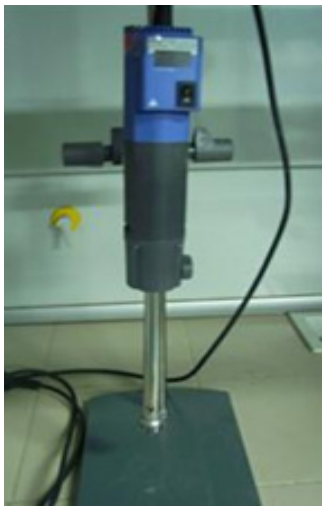

Figure 6.1. Ultra-Turrax mechanical disperser.

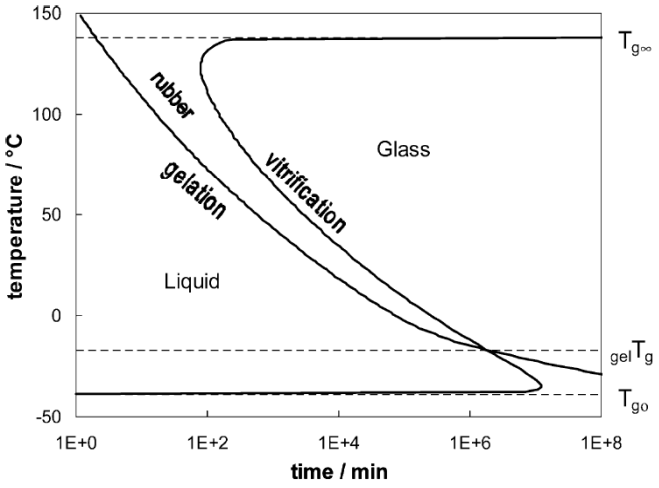

Figure 6.2. Schematic TTT cure diagram for a thermosetting system (T_{g0}, and $T_{g\infty}$ are the glass transition temperatures of the uncured and fully-cured resin, respectively. and T_g is the temperature at which gelation coincides with vitrification) (Source: Hourston 2006).

In thermosetting polymers, low molecular weight liquid is converted into high molecular weight amorphous solid polymer by chemical reaction which leads to three dimensional network. As the chemical reaction proceeds, the molecular weight and glass transition temperature (T_g) increase, and if the reaction is carried out isothermally below the glass transition temperature, the polymer will eventually reaches the reaction temperature (T_{cure}). T_g is regarded as the most important parameter for evaluating the mechanical properties of the polymers and the polymer-matrix composites as T_g generally represents the degree of cross-linking.

One of the easiest and most widely practised methods of determining T_g is to follow the change in heat flow, as a function of temperature by differential scanning calorimeter (DSC). This calorimetric method has the advantage of requiring the least amount of sample and can usually be carried out in much less time than most of the other methods. A plot of heat flow against temperature is shown in Figure 6.3, shows a more or less abrupt stepwise increase in the glass transition region and remains almost constant below and above the transition. It is very important to understand cure kinetics of resins to predict structure and behavior of their resulting reinforced composites. The cure kinetics give information about the final network structure in matrix resins, which has a significant effect on the properties of the final product (Bae, et al. 2002).

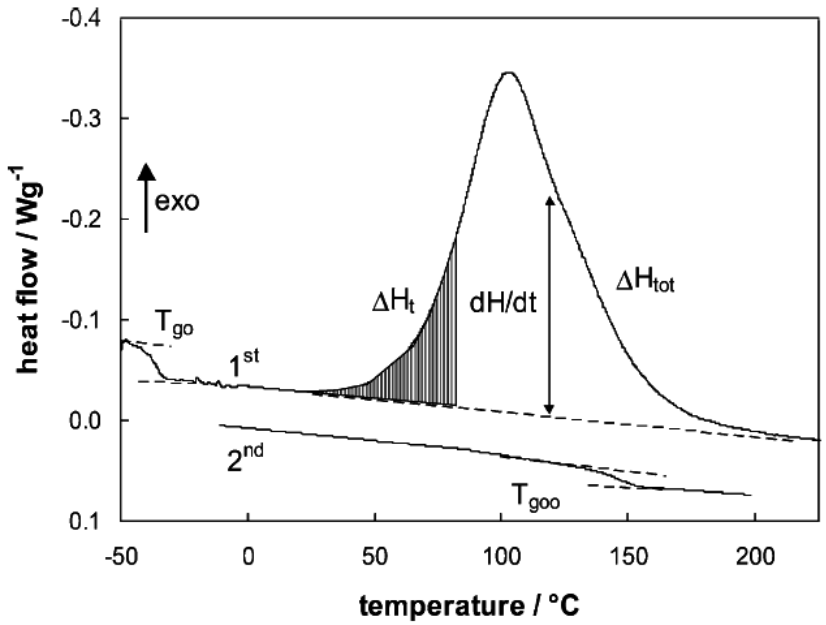

Figure 6.3. DSC heat flow signal as a function of temperature representing the non-isothermal cure of a thermosetting system: 1st and 2nd heating (Source:Hourston 2006).

The curing temperature of the used epoxy was determined using a DSC, (DSC-50, Shimadzu, Japan). Heat treated epoxy resin at 110°C for 3 h were scanned at a range of the temperature between 40°C to 140°C at a heating rate of 10°C/min. The first heating showed first stepwise shift of the baseline around 50°C and the exothermic cure reaction started near 85°C and ended at about 130°C (Figure 6.4). The theoretical overall conversion attained at this point. This reaction represented the residual cure in the resin because in the second heating, only one step was observed at 105°C. This was

glass transition temperature of fully cured epoxy (Figure 6.4). As a result, the curing process for the studied epoxy was performed at 110°C for 5 h.

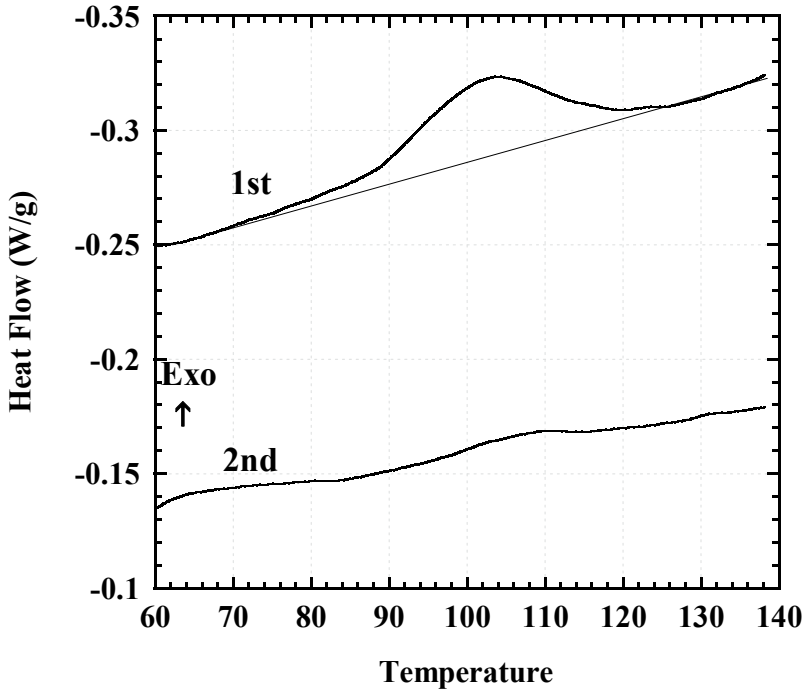

Figure 6.4. The DSC exotherm of neat epoxy.

The epoxy resin used was the diglycidyl ether of bisphenol-A (DGEBA). This resin is widely used as it has many attractive properties such as fluidity, low shrinkage during cure and ease of processing. A hardener, a Grandmer VN-111, (Süper Selva Sti, Izmir, Turkey) was used in conjunction with epoxy resin. The as-received CD contained relatively large pieces of various types of minerals and salts and relatively small broken frustules pieces. The CD was wet-sieved below 325 mesh in order to remove the insoluble large particles. ND was heat treated at 600°C for 2 h to remove the possible organic matter from the surface of frustules. Like CD, ND was then wet-sieved below the 325 mesh. The remnant was dried at 120°C for 2 h in an oven before mixing with epoxy resin to prepare the filled epoxy matrices.

The tension test specimens with 1 wt% of CD frustules were initially produced at different mixing speeds (3400, 8000, and 12000 rpm) and mixing times (5, 10, and 15 min). The test results showed that there were no significance differences in the strength values between the samples processed at different mixing speed and times. Then, the tension specimens were prepared with different weight fractions of CD (7 and 15 wt%)

using the two distinct mixing speeds (12000 and 20000 rpm) for 2 min. The tension stress-strain curves of the specimens and the tension test specimen filled with 7 and 15 wt% CD at different mixing speeds are shown in Figures 6.5(a) and (b), respectively. The tensile test specimens processed with the higher speed show higher fracture stress as seen in Figure 6.5(a) and therefore, the mixing speed was chosen 20000 rpm. The differences between the colors of samples with processing mixing speed at the same weight fraction may be related to the frustules distribution in the matrix.

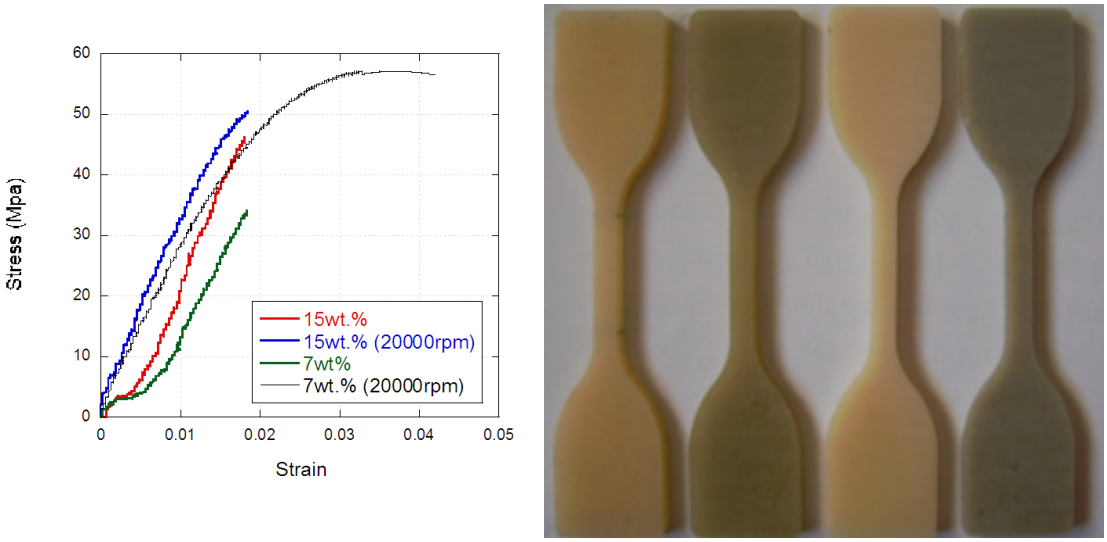

(a) (b)

Figure 6.5. (a) Stress-strain curves of 7 and 15 wt% CD filled epoxy samples processed at 12000 rpm and 20000 rpm and (b) tension test specimens (dark: 20000 rpm and bright: 12000 rpm).

Composite test samples were prepared at 5, 10, 15 and 20 wt% of ND and CD frustules. CD and ND containing epoxy suspensions were mixed by hand and then using a Digitial disperser at 20000 rpm. After degassing the solution mixture under vacuum, the hardener was added, and the solution was gently mixed in order to avoid gas bubble formation. Finally, the mixture was poured in to the tensile test specimen Teflon molds (Figure 6.6(a)). The thickness of the tension specimens was reduced to standard size (4±0.1 mm) by grinding of the surfaces of the samples (Figures 6.6(c) and (d)).

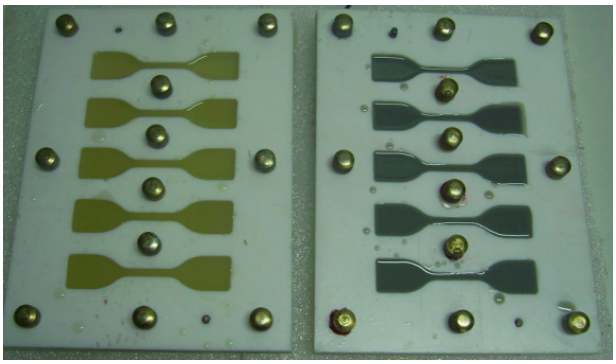

(a)

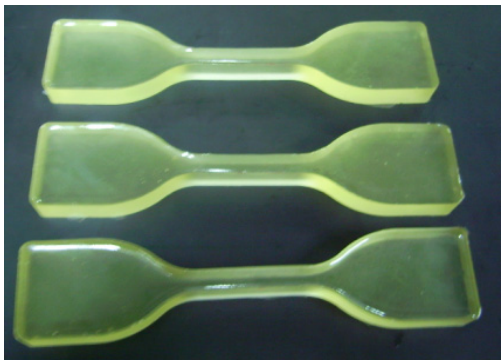

(b)

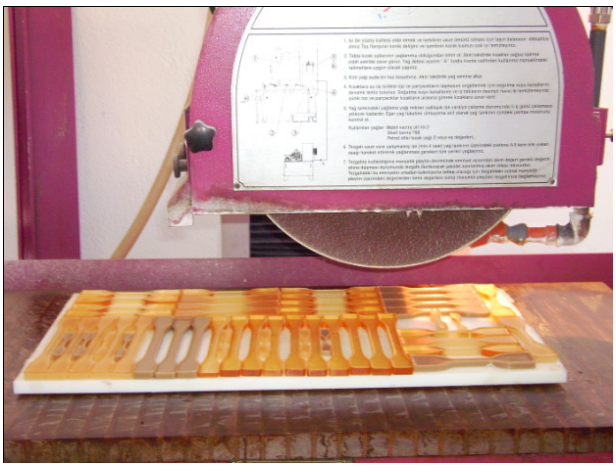

(c)

(d)

Figure6.6. Tension test specimens: (a)molded, (b) after molding and (c) and (d) after grinding process.

A rectangular Teflon mold was used to produce the compression test specimens. Cylindrical samples of 9.78 mm in diameter and 14 mm in length were core-drilled from the rectangular plates of filled epoxy. Tension and compression specimens were cured at room temperature for 24 h followed by a post curing process at 110°C for 5 h in an oven.

The weight fraction of CD and ND filled epoxies was determined from percent weight loss of TGA analysis. The volume percent of frustules in the composites was determined using the following equation

$$V_f = \frac{dW_f}{W_f + (1 - W_f)\dfrac{\rho_f}{\rho_m}} \tag{6.1}$$

Where, W_f is the frustules weight fraction of the composites samples, ρ_f and ρ_m are

the densities of the CD and ND (2.33 gr/cm^3) and pure epoxy (1.135 gr/cm^3), respectively. The thermal behavior of the neat epoxy and CD and ND filled composites were conducted using a Thermal Gravimetric Analyzer (TGA) (Shimadzu, Japan). TGA analyses were applied from at room temperature up to 500°C at heating rates of 10°C/min. These analyses were performed in a dry nitrogen atmosphere. The flow rate of nitrogen was 40 ml/min and kept constant throughout the experiments.

The chemical content of the composites was examined by Fourier transform infrared spectroscope (FTIR), (PerkinElmer Spectrum BX, USA) in the range of wave number between 4000-400cm^{-1}. The epoxy and filled epoxy specimens were analyzed by potassium bromide (KBr) technique.

6.2. Tensile and Compression Tests

The quasi-static neat and frustules filled epoxy tensile test specimens were prepared according to ASTM D638M-91a standards and the tests were conducted in an AG-I Shimadzu quasi-static mechanical testing machine. Tension tests were performed at the strain rates of 1x10^{-1} s^{-1}. The elongation of the test samples was measured using a video extensometer directly connected to the test machine. Each test was repeated at least three times and the strength and modulus values were reported as the average of these tests Quasi-static compression tests were performed in the same quasi-static mechanical testing machine at the strain rates of 1x10^{-3} and 1x10^{-1} s^{-1}. The same sample sizes were also used in the high strain rate tests. The quasi-static compression tests were applied seven specimens and the test results were averaged.

High strain rate compression tests were performed in a compression type Split Hopkinson Pressure Bar (SHPB) apparatus at the strain rate regimes of 300-600 s^{-1}. The schematic of the SHPB and the picture of the SHPB apparatus used are shown in Figures 6.7.(a) and (b), respectively. The SHPB apparatus consists of 19.45 mm diameter Inconel 718 bar, a 3109 mm long incident bar and 2050 mm long transmitter bar, and a 50 mm long striker bar. The striker bar produces a constant amplitude elastic compressive wave in the incident bar; this wave propagates down the bar to the bar/specimen interface where it is partly reflected back into the incident bar as a tensile pulse and partly transmitted to the transmitter bar as a compressive pulse. The reflected pulse (ε_r) yields information on the strain rate involved in the specimen and the

transmitted wave (ε_t) gives the stress in the specimen. The strain rate ($\dot{\varepsilon}$), strain (ε) and stress (σ) in the specimen in SHPB testing are calculated using the following equations based on one-dimensional wave propagation in long bars:

$$\dot{\varepsilon}(t) = \frac{-2C_b}{L_s}\varepsilon_r(t) \tag{6.2}$$

$$\varepsilon(t) = \frac{-2C_b}{L_s}\int_0^t \varepsilon_r(t)dt \tag{6.3}$$

$$\sigma(t) = \frac{E_b A_b}{A_s}\varepsilon_t(t) \tag{6.4}$$

where, C_b is the elastic wave velocity of the bar, L_s is the sample length and A_s and A_b are the sample and bar cross-sectional areas respectively. The reflected and transmitted strains measured from strain gages on the bar, respectively. At least three compression tests were performed at quasi-static and high strain rate tests.

The above equations are based on the assumption that the forces at sample-bar interfaces are equal. The experimental force equilibrium for the same incident and transmitter bars diameter is expressed as

$$\sigma_t(t) = \sigma_i(t) + \sigma_r(t) \tag{6.5}$$

Where, σ_t, σ_i and σ_r are the transmitted, incident and reflected stresses, respectively. The left and right sides of this equality are used in the so-called "one-wave" and "two-wave" analyses, respectively. Stress equilibrium within the sample is considered to be reached after 3-4 back and forth reflections of the wave in the sample and the time at which equilibrium is established depends on the wave transit time of the sample. Since the transmitter bar of the used SHPB is shorter than the incident bar, the tensile wave reflected from the transmitter bar end separates the bars and, therefore, the sample deforms only once under compression. Composite samples, compressed to various strains and up to failure at quasi-static and high strain rates, were metallographically

prepared for the microscopic analysis.

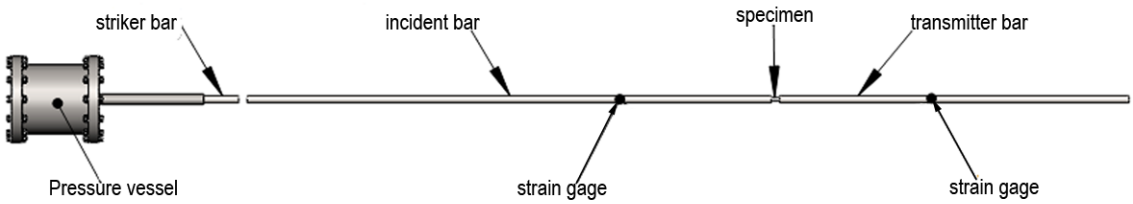

(a)

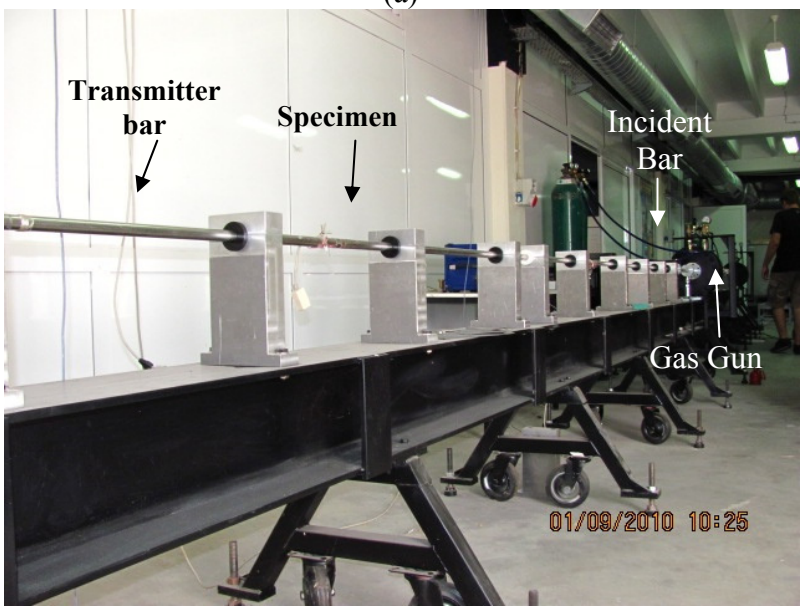

(b)

Figure 5.15. (a) Schematic and (b) picture of compression SHPB set-up.

Typical SHPB incident and transmitted wave record as function of time is shown in Figure 6.8(a). The time window of the incident wave with used striker bar is about 300 μs. The corresponding stress-strain and strain rate-strain graphs are further shown in Figure 6.8(b). As noted the strain rate varies during a test; therefore, an average strain rate is calculated between the strain corresponding to the maximum strain rate and the final attained strain in Figure 6.8(b). The compressive strength is taken as the maximum stress in the stress-strain curve and the Elastic modulus (E) is measured from the slope old the stress-strain curve as depicted in Figure 6.8(b). The samples for SHPB were prepared by core-drilling the prepared cast composite plates. The typical core-drilled compression test sample is shown in Figure 6.9(a). The interface between the bar surface and specimen surfaces were lubricated before each test. Figure 6.9(b) further shows the picture of a test sample just before the SHPB compression testing.

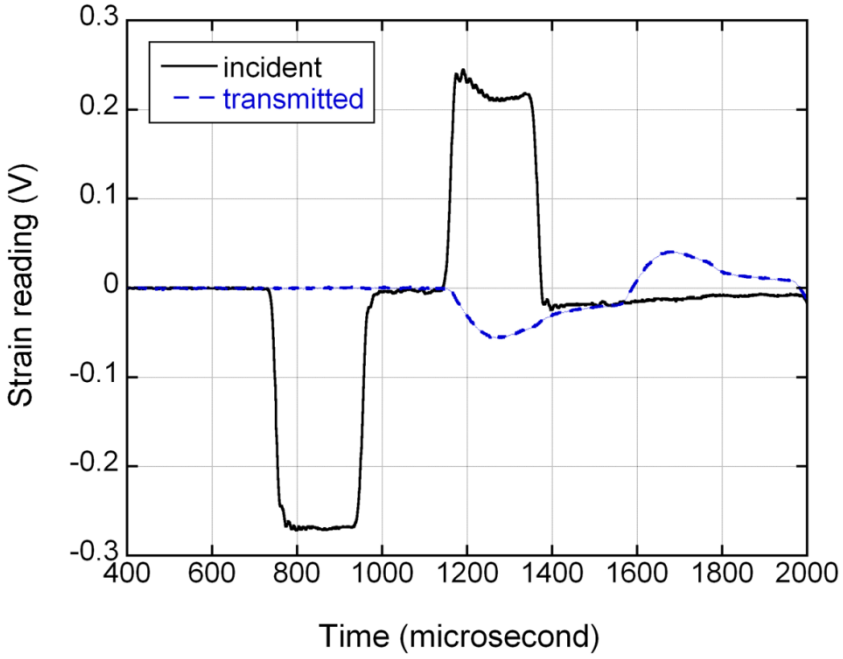

(a)

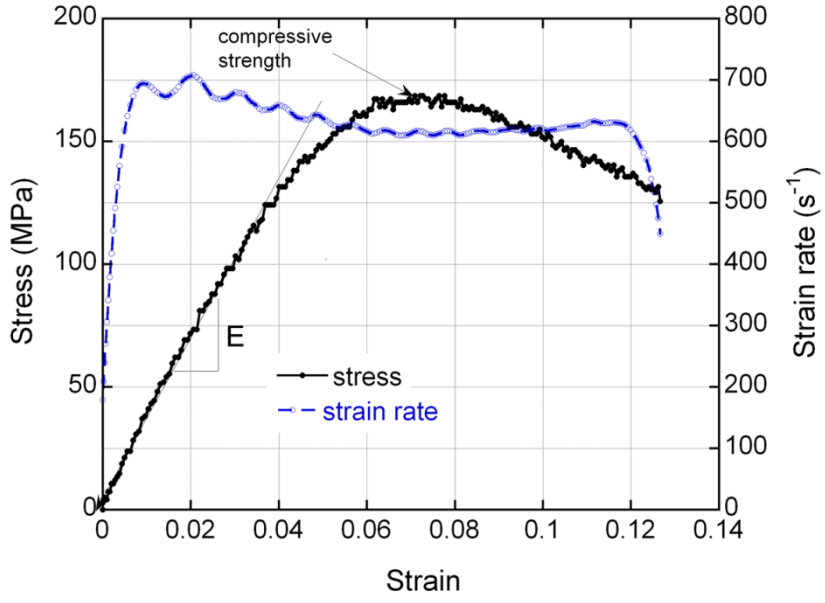

(b)

Figure6.8. Typical (a) incident and transmitted wave-time and (b) stress-strain rate-strain graphs of neat epoxy.

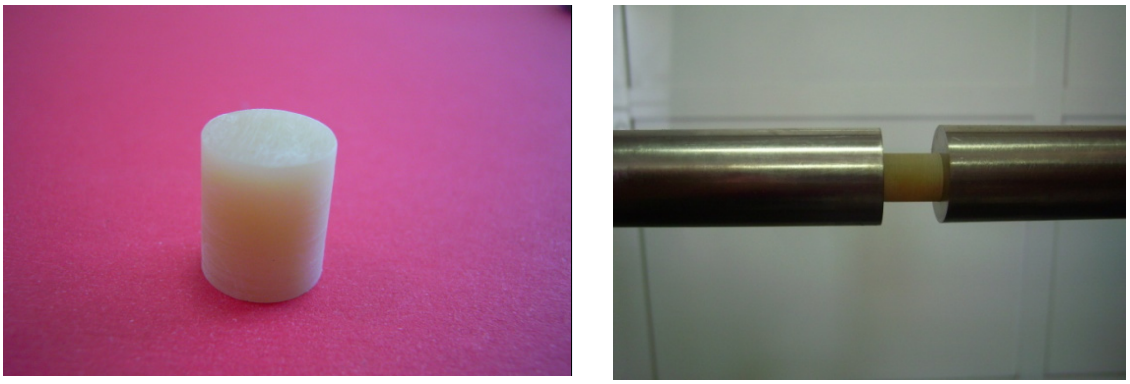

(a) (b)

Figure6.9. (a) SHPB compression test specimen and (b) the specimen inserted in between the bars.

6.3. Projectile Impact Test

The projectile impact resistances of neat and filled epoxy matrices plates were determined using a projectile impact tester as seen in Figures 6.10 (a) and (b). The impact apparatus consists of gas chamber, barrel, sabot and specimen chamber.

Neat epoxy and frustules filled composite plates, 25x25x1cm, were fixed into a rigid frame in the specimen chamber. The projectile used was a 30 mm diameter marble sphere which had a weight of 110 g. A Fast-Cam high speed video camera was used to monitor and record the impact of the projectile to the plates. All tests were performed under ambient conditions at impact velocities of 100, 160 and 200 m s^{-1}.

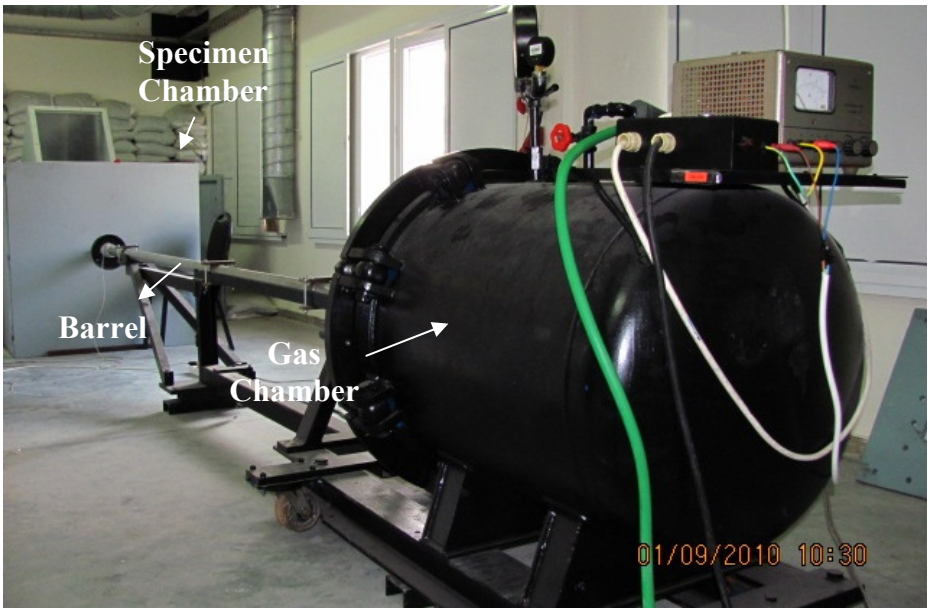

(a)

(b)

Figure 6.10. (a) Projectile impact tester and (b) specimen frame.

6.4. Microscopic Examination

Frustules filled epoxy samples, compressed to various strains and up to failure at quasi-static and high strain rates, were metallographically prepared for microscopic analysis. Typical damage mechanisms operative prior to and during the failure were determined using SEM. Fracture surfaces of tensile and compressive specimens failed under loading were examined to determine the effects of diatom frustules on the damage mechanisms.

6.5. Contact Angle Measurements

Solid–liquid contact angle is defined as the included angle made between the liquid–vapour surface and liquid–solid surface along a three phase contact line (Hunter 1991). The liquid wets the surface when contact angle decreases and will spread readily across it, whereas liquid does not wet the surface and will tend to form beads when high contact angles increases Contact angle of liquid was given by Laplace-Young equation (Iveson, et al. 2000).

$$\cos\theta = \frac{\gamma_{SV} - \gamma_{SL}}{\gamma_{VL}} \tag{6.6}$$

where, γ_{SV}, γ_{SL} and γ_{VL} are the solid-vapour, the solid–liquid, and the vapour–liquid interfacial tensions (or the interfacial free energies per unit area), respectively. The contact angle measurement and the solid-liquid-vapour interfacial tensions were shown in Figure 6.11.

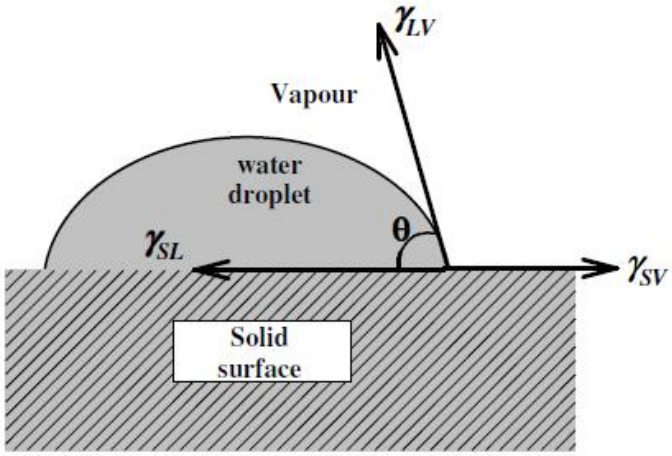

Figure 6.11. Contact angle measurement (Aksoy, et al. 2006).

The contact angle (θ) measurements were applied using a contact angle meter to determine quantity the degree of wettability. Therefore, a distilled water droplet of 5 µl was placed on the surface of the ND and CD frustules pellet and neat epoxy samples. Five different angle were measured and the average value was then taken as the contact angle (θ). The mean values of contact angles of ND, CD frustules and neat epoxy are

given in Table 6.1. Results showed that neat epoxy is hydrophobic while both frustules are hydrophilic and CD frustules are more hydrophilic.

Table 6.1. Contact angle of frustules and epoxy.

Specimens	ND frustules	CD frustules	Neat epoxy
Contact angles (°)	19.24±0.84	14.60±0.87	80.21±1.72

CHAPTER 7

THERMAL BEHAVIOR OF DIATOMITE FILLED EPOXY

TGA curves of both diatom frustules are shown in Figure 7.1. Almost no weight loss is observed in CD frustules, while ND frustules show 2% weight loss probably due to the adsorbed water on the frustules. Figure 7.2 shows TGA curve of neat epoxy. The initial thermal decomposition temperature of neat epoxy is determined 372°C. Figure 7.3 and Figure 7.4 further show the typical TGA curves of neat epoxy and CD and NDfilled epoxy composite of different wt% of frustules, respectively. The shapes of the TGA curves of CD and ND filled epoxy resins are very similar to that of neat epoxy as seen in Figure 7.3 and Figure 7.4. The initial thermal decomposition temperature decreases to 369°C with the addition or 1 wt% CD frustules. The thermal decomposition temperatures are determined as 310, 310 and 322°C for 7, 15 and 21 wt% CD frustules content at 10% weight loss, respectively (Table 7.1). At the same weight loss the decomposition temperature of neat epoxy is 307°C. These show that CD frustule addition has almost no effect of the thermal stability of the polymer at 10 wt% loss. The increase in thermal decomposition temperature at 50% weight loss is about 21°C for 21 wt% CD frustule addition. The TGA curves of the ND filled epoxy are also very similar to that of neat epoxy. This is reasonable since thermal weight loss of the ND/epoxy is results from the epoxy resin part. The increase in thermal decomposition temperature at 50% weight loss is about 12°C for 21 wt% ND frustule addition, respectively. Consequently, it is concluded that the thermal stability of neat epoxy is insignificantly affected with the addition of CD and ND frustules. TGA curves also show that the degradation of epoxy resins occurs at temperatures between 400 and 500°C. The percentage of weight loss of neat epoxy is measured 11.03 from TGA curves. The residual may be due to the differences between the thermal degradation behavior of neat epoxy and hardener. It is assumed that this weight loss of neat epoxy (11.03) at 500°C as reference and the weight fraction of frustules in epoxy matrix is calculated. Table 7.2 tabulates the experimental and calculated weight fractions and matched volume fractions of the filler.

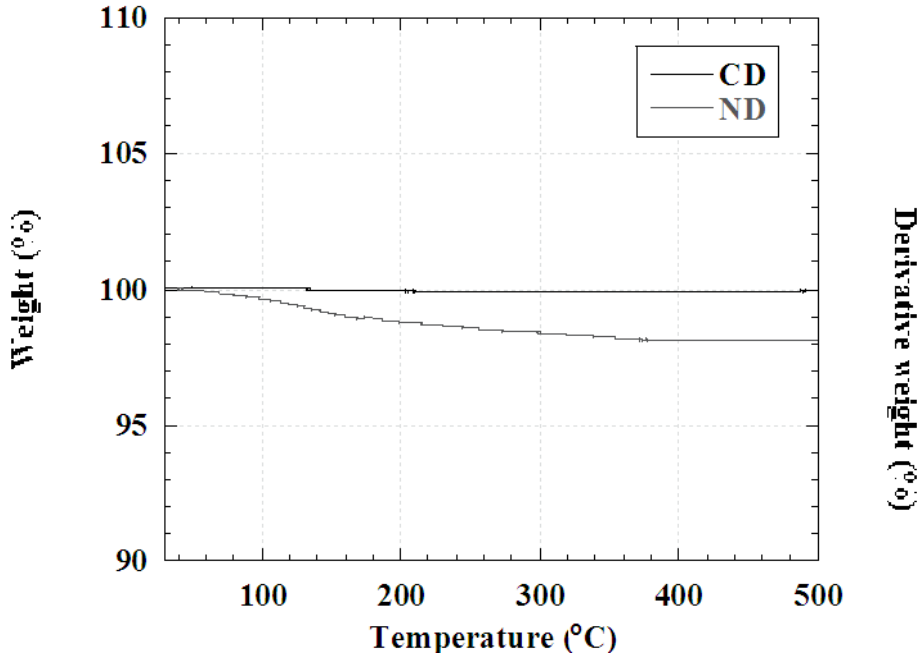

Figure 7.1. TGA curves of CD and ND frustules.

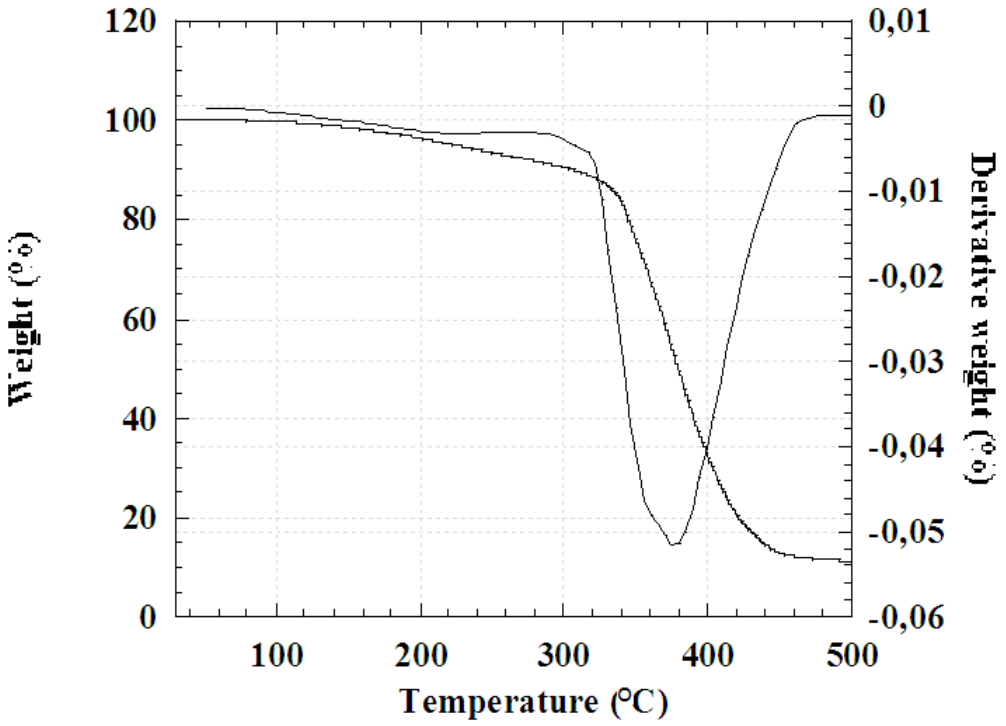

Figure 7.2.Thermogravimetric mass loss of neat epoxy.

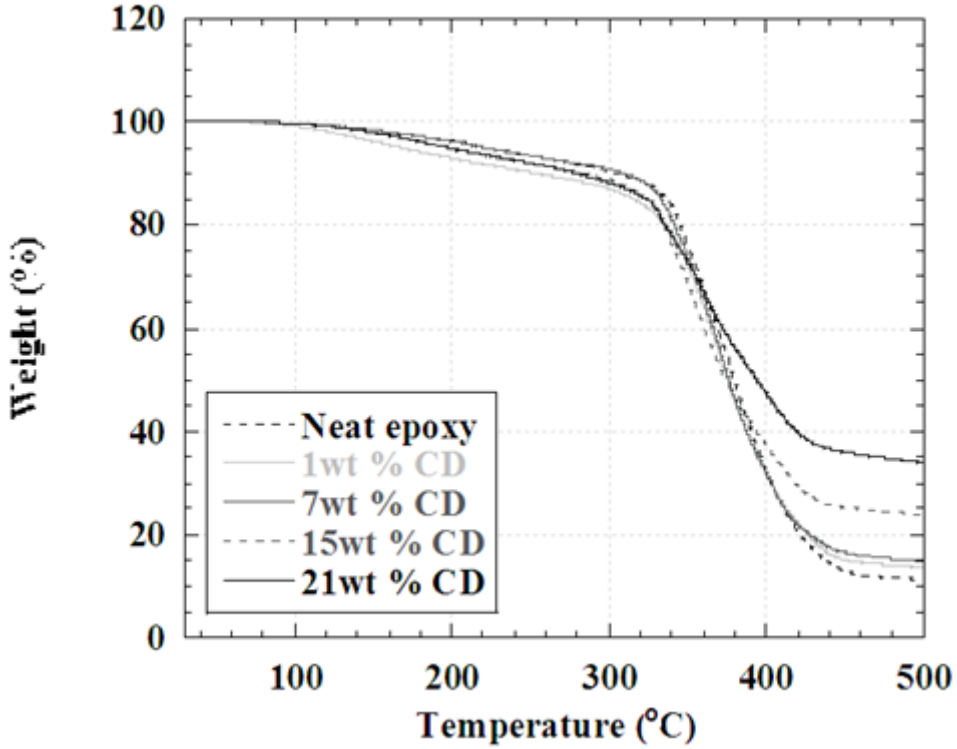

Figure 7.3. TGA curves of CD filled epoxy composites.

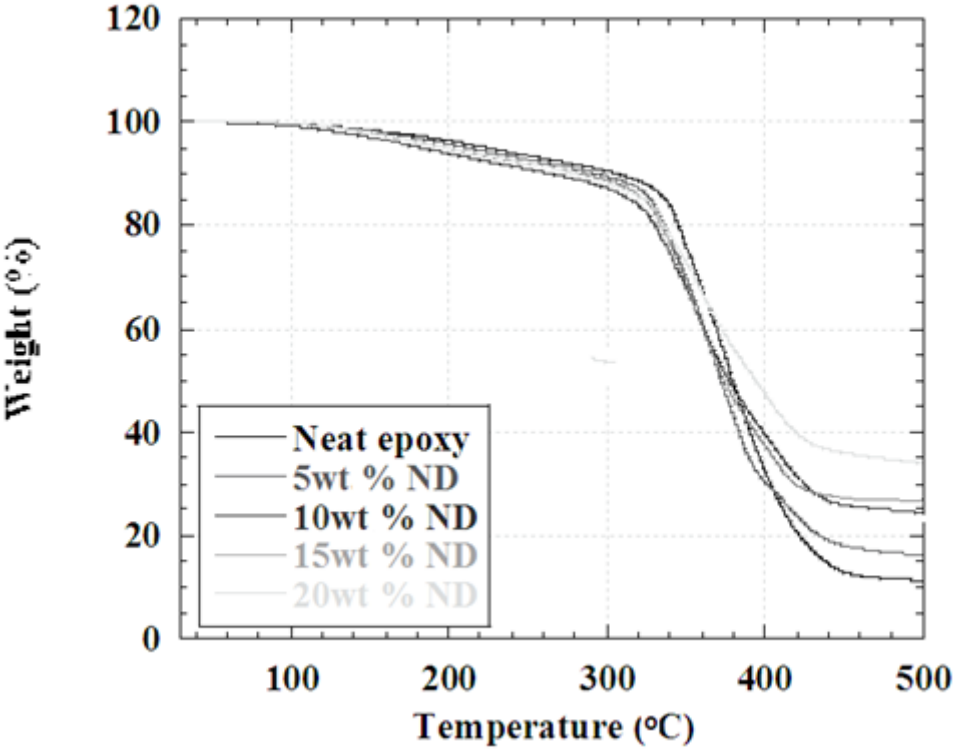

Figure 7.4. TGA curves of neat ND filled epoxy composites.

Table 7.1. IDT values of CD and ND filled epoxy.

Sample		IDT(°C)	T at weight loss (°C)	
			10%wt	50% wt
Neat epoxy		372.8	307.3	374.83
CD filling (wt%)	1	369.2	255.4	370.5
	7	371.6	310.2	371.0
	15	366.3	310.0	375.8
	21	362.3	322.1	395.5
ND filling (wt%)	5	363.4	295.1	366.5
	10	357.1	268.5	377.1
	15	357.1	287.4	368.2
	20	358.5	282.3	386.8

Table 7.2. The volume fraction of composites.

Filler materials	Experimental (wt%)	Calculated (wt%)	Vol%
CD	1	2.36	1.2
	7	3.5	1.7
	15	14.75	7.7
	21	20.86	11.3
ND	5	4.96	2.5
	10	8.38	4.3
	15	13.05	6.8
	20	21.45	11.7

FTIR spectra of the epoxy cured at room temperature for 24 h and at 110°C for 5h are shown in Figure 7.5. Both FTIR spectra show the similar peaks. The strong absorption peaking at 3380 cm^{-1} corresponds to the vibration of –OH. The bands at 1510 and 830 cm^{-1} are due to p-phenylene groups (Fraga, et al. 2008). The peaks at 1600, 1500, and 1450 $cm^{-1}$are assigned to the stretching vibration of the aromatic C=C bond and the peaks at 1000–1200 cm^{-1} to the in-plane deformation vibration of the hydrogen atom on an aromatic ring (Harada, et al. 2003). The peak at about 1292 cm^{-1} represents OH hydroxyl groups. The absorbance at 3055 and 2997 cm^{-1} show tension of

–CH group of the epoxide ring and stretching of the $–CH_2$ of the epoxide ring, respectively. The different vibration bands of the epoxy groups at 760, 915, and 970 cm^{-1} decreases during the curing reaction (Fraga, et al. 2008). The vibration band at 760, 915 and 970 cm^{-1} are examined as reference bands. The gradual decrease of these peaks reflect the reaction of epoxide rings to form ether linkages (Ramis, et al. 2004),(Fraga, et al. 2001). Figure 7.6 further shows the FTIR spectra of as-received and room temperature cured epoxy. As is noted, the intensity of the vibration bands of epoxy group decreases at the cured condition. The disappearance of the band at 915 cm^{-1} is associated with the oxirane ring indicating the epoxide polymerization. This further demonstrates that epoxy is cured largely at room temperature in 24 h. The effect of post curing on the cure behavior of epoxy is shown in Figure 7.7. After post curing, the reduction of the band of the epoxy groups at 760 cm^{-1} indicates the continue reaction with the epoxide group. The FTIR spectra of neat and CD frustules filled epoxy are shown in Figure 7.8. The presence of broad overlapping bands between 1000 and 1200 cm^{-1} and 618 and 450 cm^{-1} in the spectra of 7 and 21 wt% CD filled epoxy confirms the existence of a silicon-oxide network, which results from the addition of diatom frustules into epoxy matrix. FTIR spectra ND filled epoxy samples also show the similar results as depicted in Figure 7.9. It may be concluded from FTIR results that the introduction of diatom frustules forms a silica network in the epoxy matrix and has no negative influence on the curing behavior of epoxy.

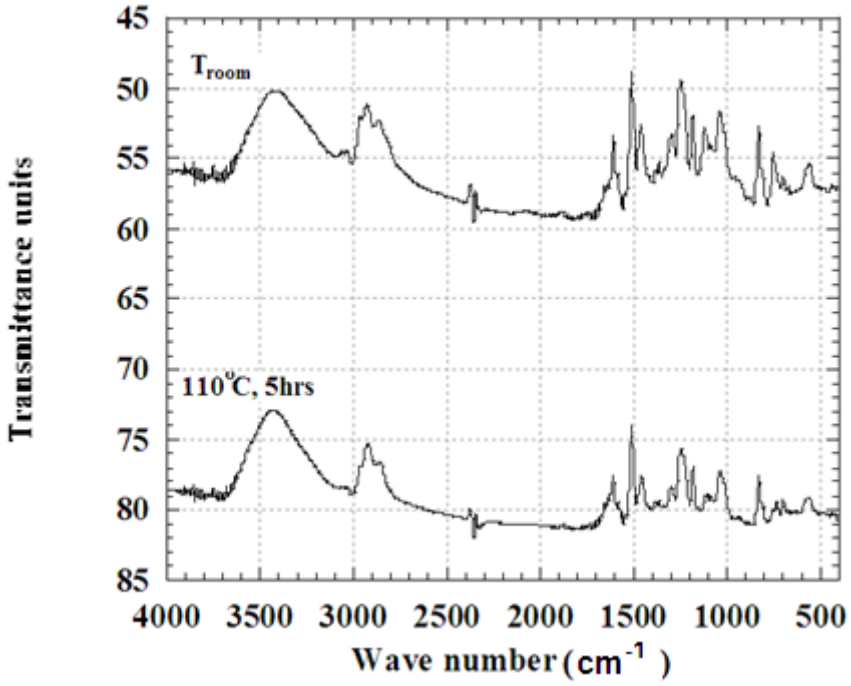

Figure 7.5. FTIR spectra of epoxy cured at room temperature and 110°C.

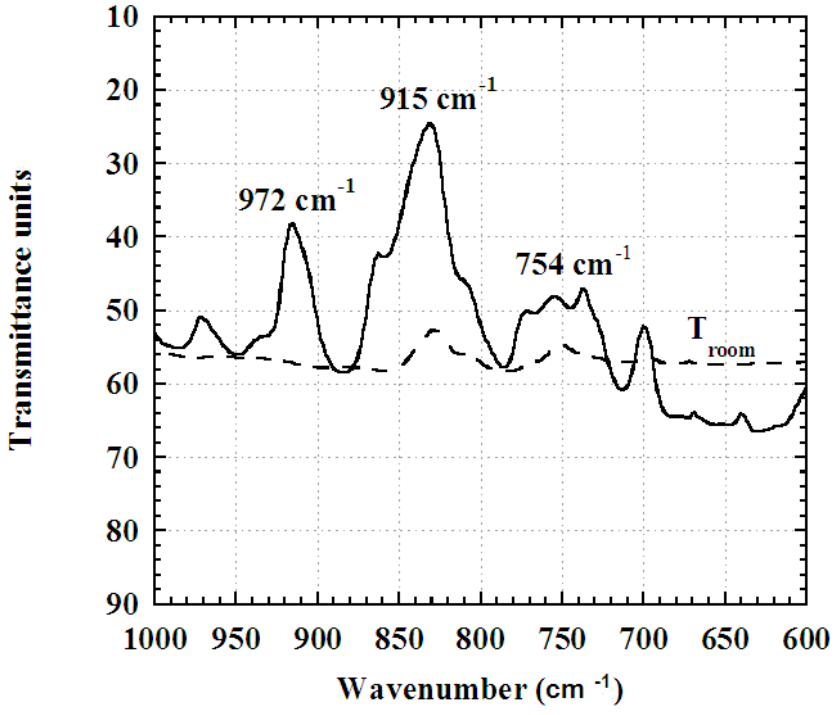

Figure 7.6. FTIR spectra of as-received and room temperature cured epoxy.

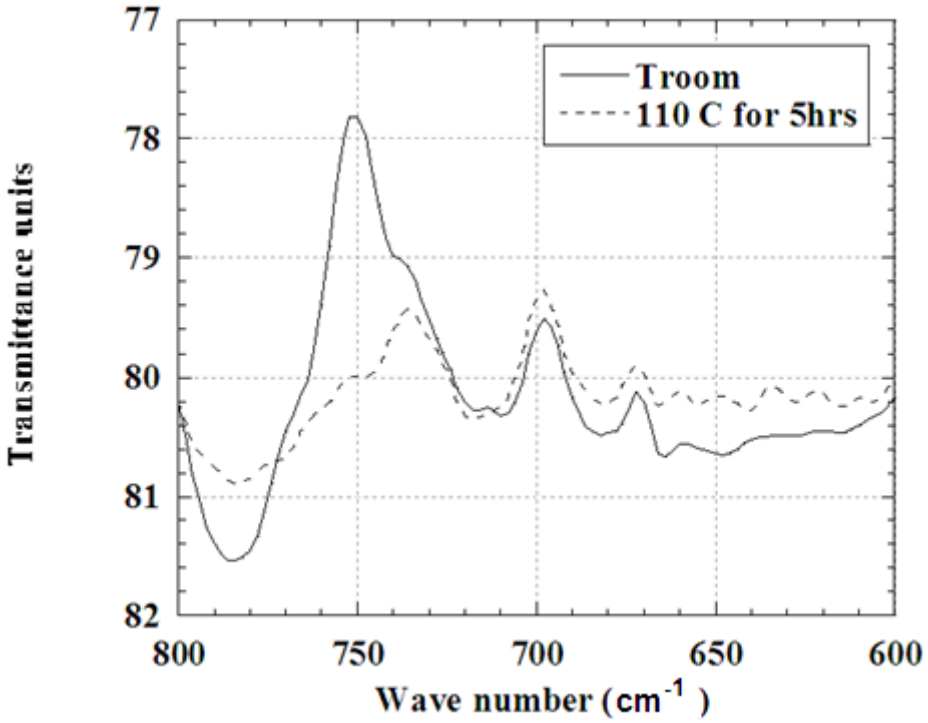

Figure 7.7. Intensity of the vibration band of the epoxy group at 760 cm^{-1} after post curing.

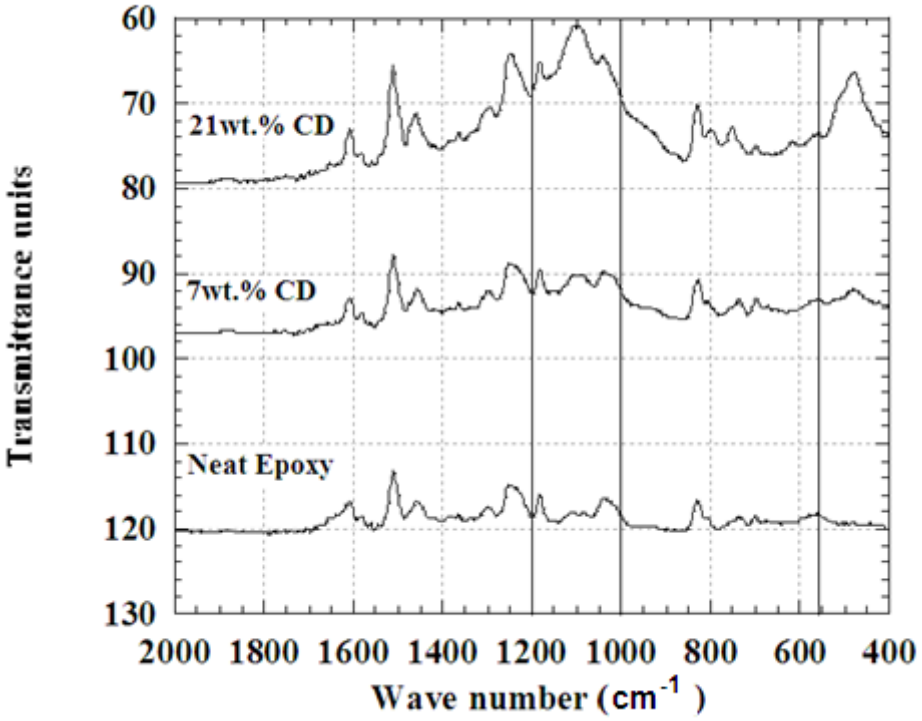

Figure 7.8. The FTIR spectra of neat and CD frustules filled epoxy.

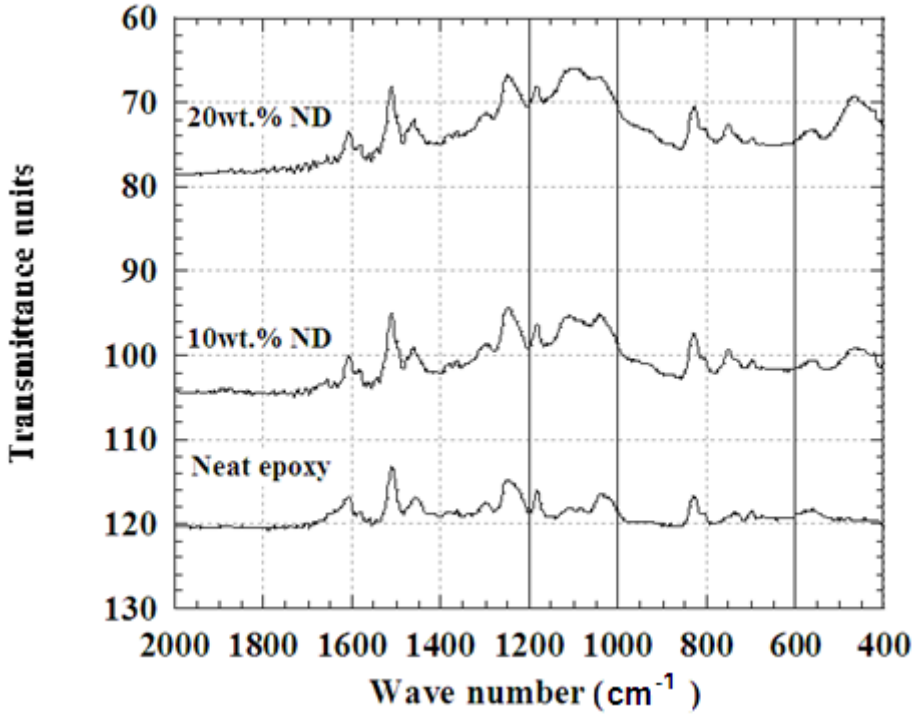

Figure 7.9. The FTIR spectra of pure and ND frustules filled epoxy.

CHAPTER 8

QUASI-STATIC AND DYNAMIC MECHANICAL BEHAVIOR OF FRUSTULES FILLED EPOXY

8.1. Compression Behavior

Figure 8.1 shows diatom frustules distribution through the thickness of the prepared 15 wt% (≈8vol%) frustules-filled epoxy plate. In this (contrast inverted) SEM micrograph, C and T refer the compression axis and thickness directions, respectively. It is noted in Figure 8.1(a) that the frustules' tube-axes are preferentially aligned in the plane normal to the thickness of the plate as relatively few are aligned through the thickness, showing a nearly planar random tube-axis distribution in the plane normal to the plate thickness. The compression tests were, therefore, conducted parallel to the planar random plane. Figure 8.1(b) shows two diatom frustules whose tube axes were aligned normal to the thickness of the plate. It is also seen in the same figure (b and c) that the interiors of the tubes are completely filled with epoxy resin.

The effects of strain rate on the compression stress-strain curves of CD and ND frustule filled epoxy matrices are shown in Figures 8.2(a) and (b), respectively. Increasing strain rate increases the stress values of both neat and filled epoxy matrices, depicted in Figures 8.2(a) and (b). While, the compression failure strains decrease significantly with increasing strain rate in the neat and filled epoxy matrices. A higher strengthening of ND frustule filled epoxy matrix with increasing strain rate is noted in Figures 8.2(b).

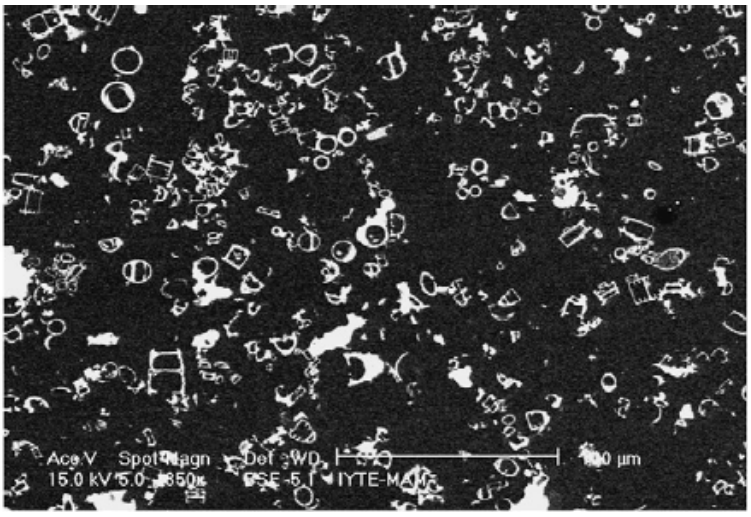

(a)

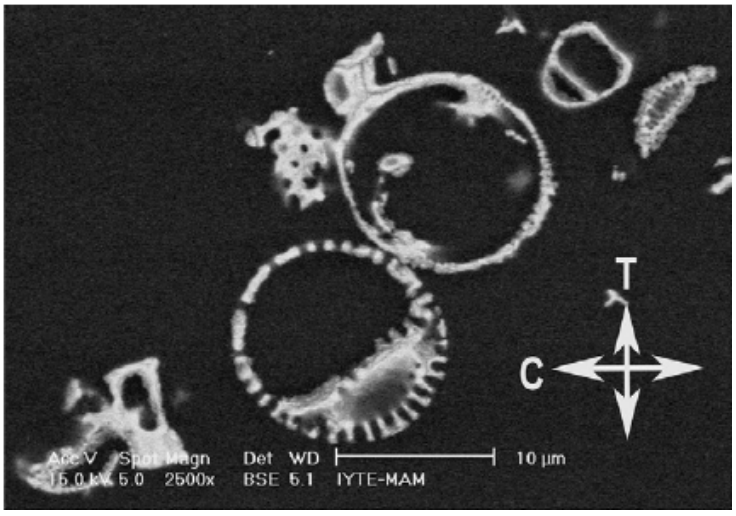

(b)

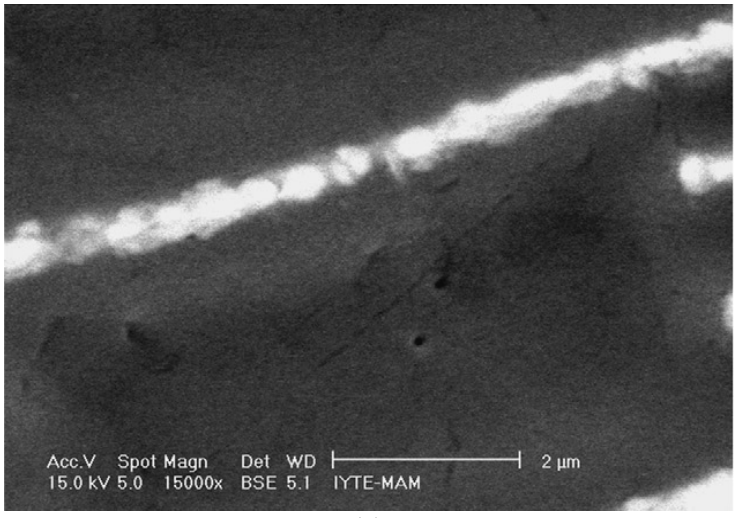

(c)

Figure 8. 1. SEM micrographs of the CD/epoxy matrix showing (a) distribution of the frustules in the matrix, (b) completely filled frustules (normal to the frustule tube axis), (c) the wall of a frustule.

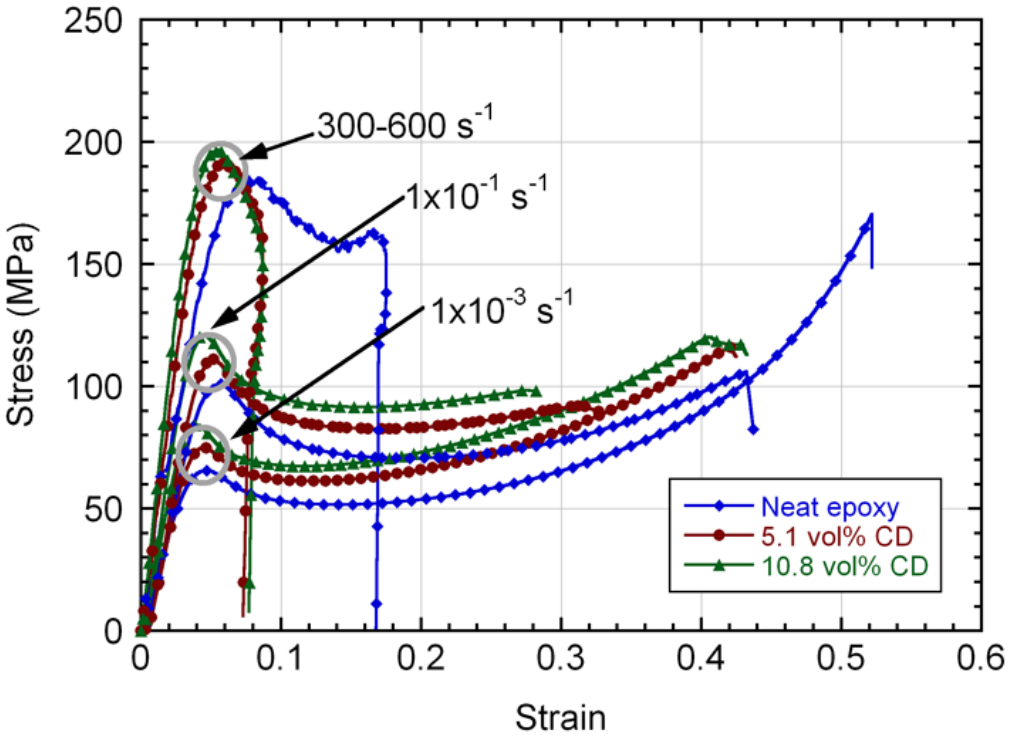

(a)

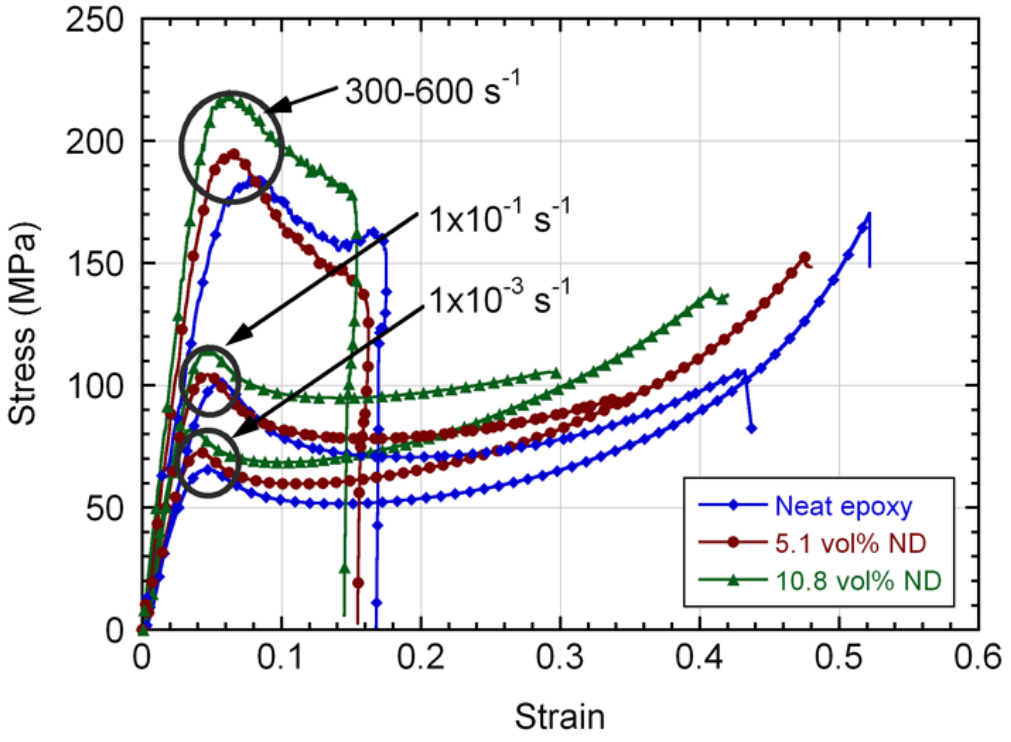

(b)

Figure 8.2. The effects of strain rates on the compression stress-strain curves of (a) CD and (b) ND frustules filled epoxy.

The stress-strain curves of polymer based composites can be separated in to five stages: initial linear elasticity, non-linear transition to global yield, strain softening, flow at constant stress and strain hardening, which are the typical features of many glassy polymers (Mulliken and Boyce 2006). Stress-strain curves of frustules filled and neat epoxy reveal typical compression characteristics at quasi-static strain rates. As the strain rate increases, the strain hardening effect decreases for both ND and CD filled epoxies. Despite the fact that this is a secondary factor compared with the strain-rate effect to the stress–strain behavior of the composites, it should not be ignored. The decrease in strain-hardening effect may be related to the micro damage during loading in the composites. At high loading rates, more breakage occurs to adapt the deformation of the specimen due to decrease the mobility of polymer chains. Another reason for the reduction of strain hardening effect with the increasing strain rate is related to the heating. Heat is produced at high strain-rate during loading, causing the weakness (Guo and Li 2007).

The reduction of the failure strains of the epoxy and frustules-filled epoxy at high strain rates as compared to the quasi-static strain rates may also be a strain rate effect and the micro damage accumulation in the composites. The reduction in the failure strain is caused by an embrittlement effect as the stiffness of the composites increases when the frustules volume percentage is increased (Fu, et al. 2000). Clearly, compressive yield stress of the composites increases with increasing strain rate and volume percent of frustules. The increase in the stress values with strain rate is mainly related to the secondary molecular process (Chen and Ravichandran 1994). Increasing strain rate and frustules addition restrict the movement of polymer chains and the stiffness increases.

Figures 8.3(a) and (b) show the variation of the compressive strength values (the initial maximum stress) with the strain rate for CD and ND frustules filled epoxy matrices, respectively. At low strain rates, there is a linear relationship between compressive strength and the logarithm of the strain rate. On the other hand, sharp increase in the strain rate sensitivity is shown at high strain rate. The same observation was previously reported for silica filled epoxy composites (Guo and Li 2007). The compressive strength values (σ_c) in these figure are fitted with the following relation,

$$\sigma_c = \sigma_0 + K \ln\left(\frac{\dot{\varepsilon}}{\dot{\varepsilon}_0}\right) \tag{8.1}$$

where, σ_o is the strength at the reference strain rate, K is the strain rate parameter and $\dot{\varepsilon}$ and $\dot{\varepsilon}_o$ are the strain rate and reference strain rate. The strain rate parameter of the neat epoxy is found 8. In CD frustule filled epoxy matrices the strain rate parameter increases to 8.75 and in ND frustule filled epoxy to 10.2 when the frustule volume increases to 10.8%. These confirm a higher strain rate sensitivity of the ND filled epoxy matrices. Figures 8.4(a) and (b) show the variation of the elastic modulus of CD and ND frustules filled epoxy matrices with the strain rate, respectively. The modulus values are fitted with equation 8.1. Again an increased strain rate parameter is found in filled epoxy matrices. The strain rate parameter for neat epoxy is found 2120, while the strain rate parameter increases to about 3200 for ND and CD filled epoxy matrices.

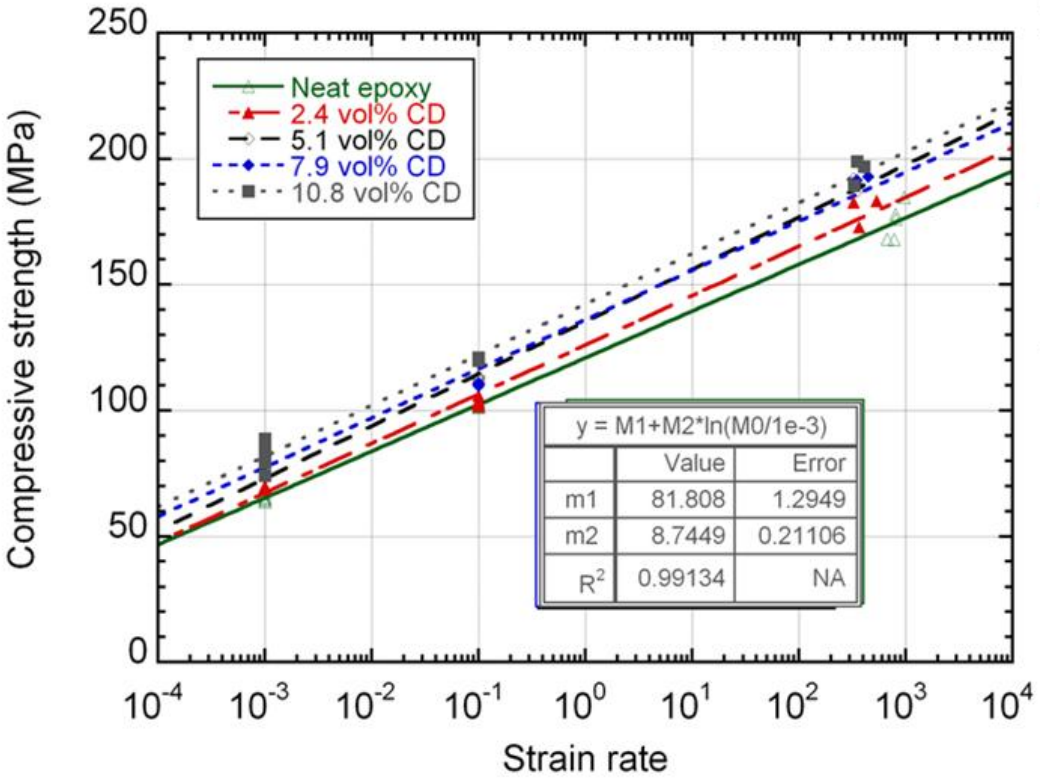

(a)

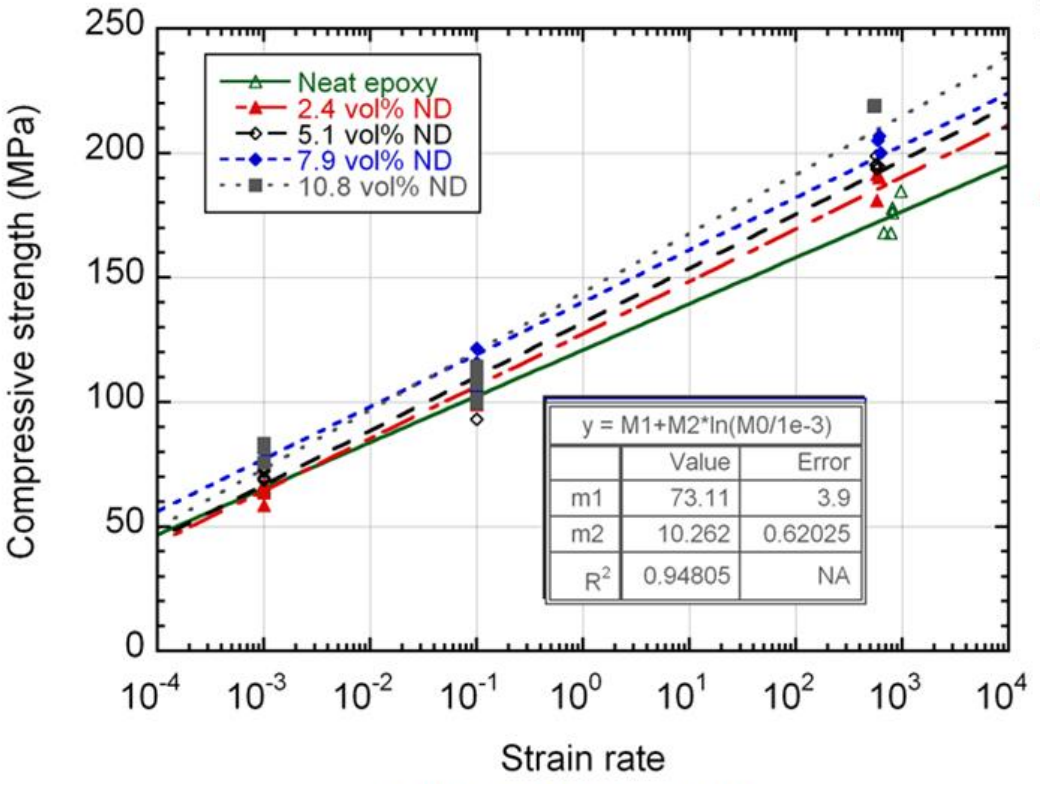

(b)

Figure 8.3. The compression strength as a function of frustules volume fraction of epoxy composites at different loading rates.

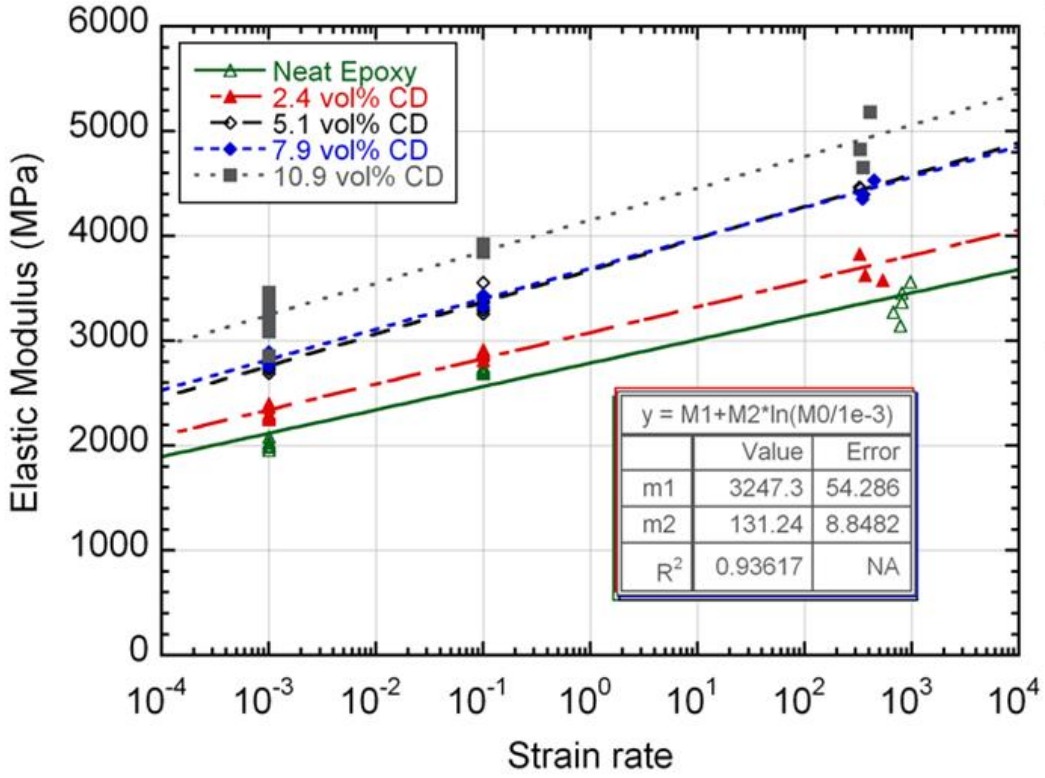

(a)

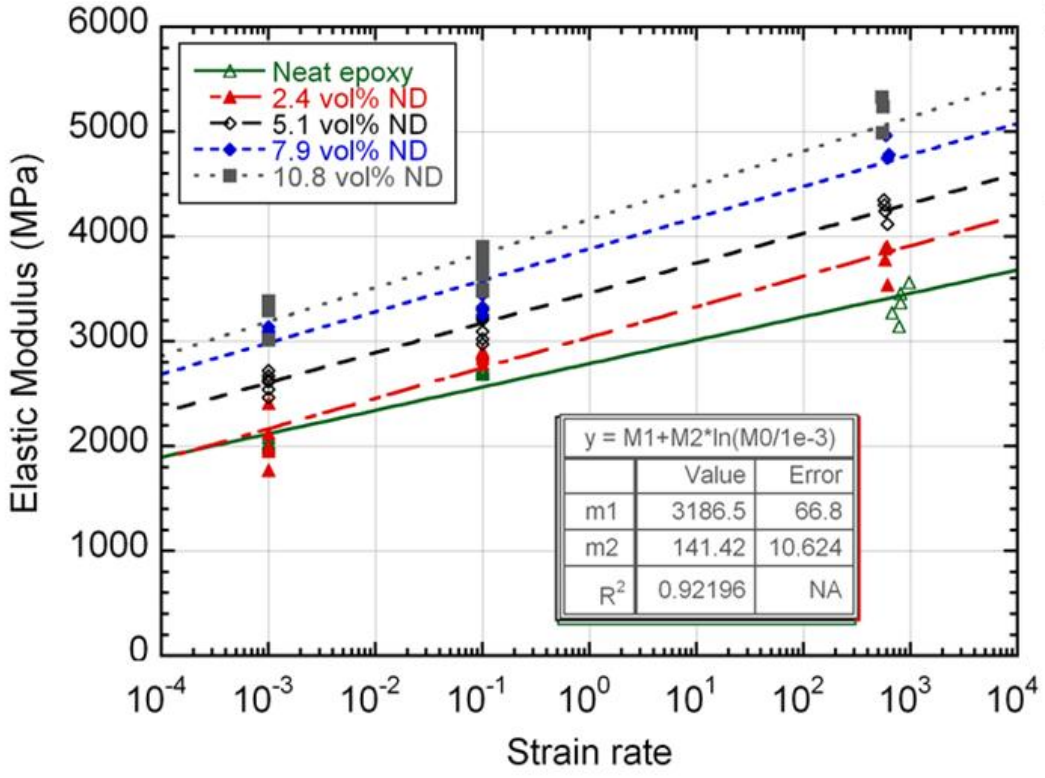

(b)

Figure 8.4. The elastic modulus as a function of logarithmic strain rate: (a) CD filled and (b) ND filled epoxy.

The fracture of the neat and filled epoxy matrices tested at quasi-static strain rates is observed to occur through two shear bands progressing ~45^{o} to the loading axis as shown in Figure 8.5(a). On the other hand, the failure of neat epoxy proceeds with the fracture of a single shear band (~45^{o} to the loading axis) at high strain rate testing in SHPB (Figure 8.5(b)). It is noted that the failure of the filled epoxy matrices switches from shear banding to axial spitting with the increasing the frustule vol%'s at high strain rates as depicted Figure 8.5(b). Microscopic analysis of the fracture surfaces of samples compression tested at quasi-static strain rate also reveals the debonded and crushed frustules into many pieces (Figure 8.6(a)). While, the fracture of the frustule filled epoxy matrix is seen relatively flat with few or no crushed frustules pieces (Figure 8.6(b)), proving the brittle behavior of the filled epoxy at high strain rates.

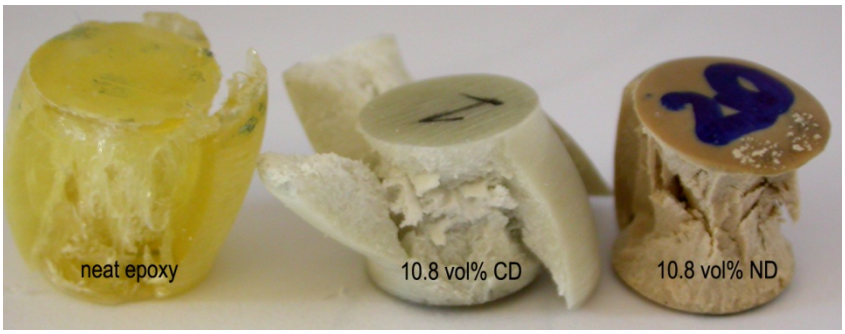

(a)

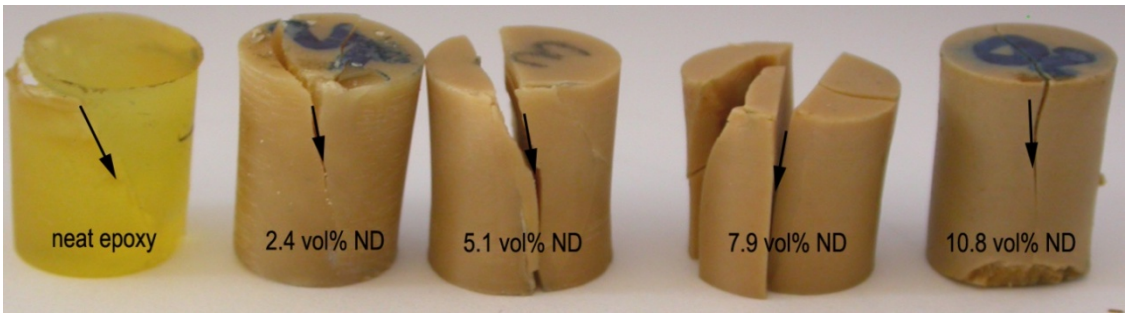

(b)

Figure 8.5. The pictures of failed compression test samples (a) $1x10^{-3}$ s^{-1} and (b) $600s^{-1}$..

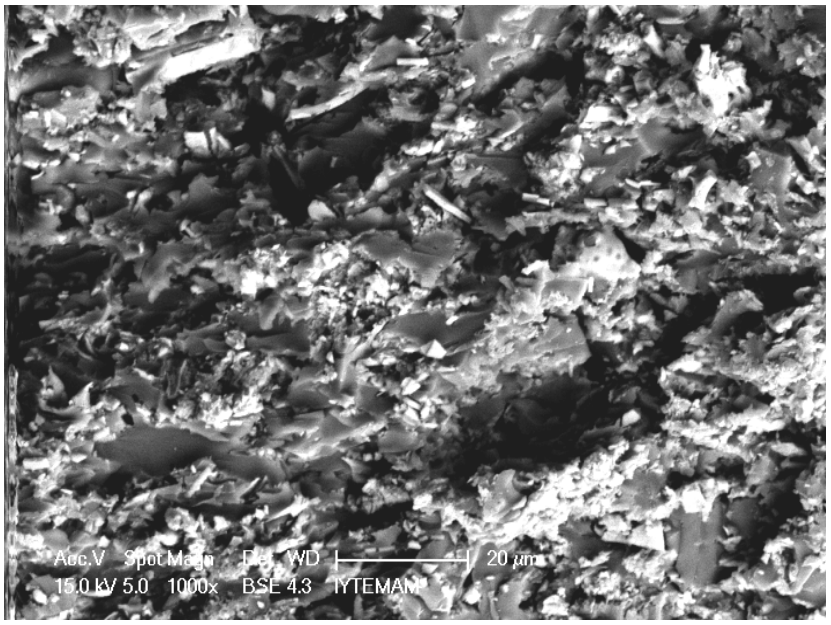

(a)

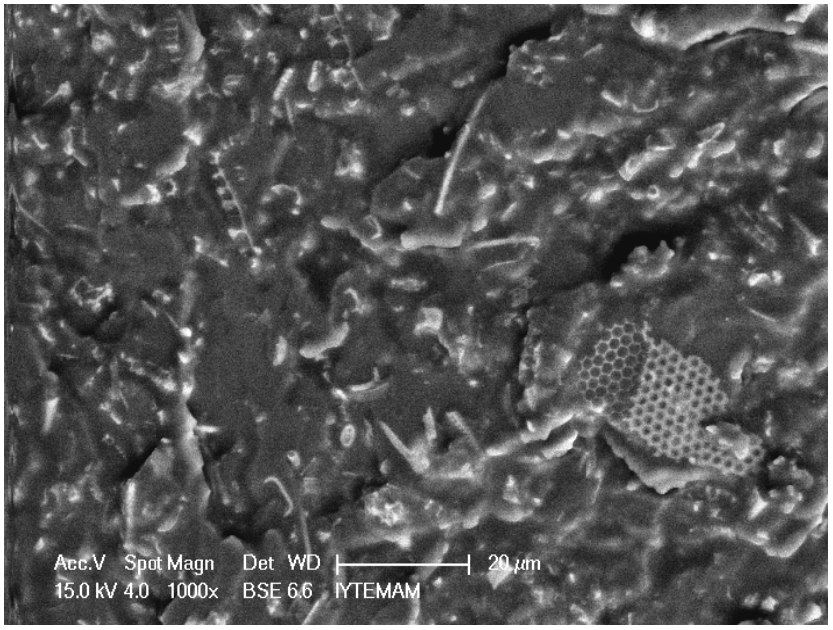

(c)

Figure 8.6. The fracture surface of 10.8vol%ND filled epoxy tested at (a) $1x10^{-1}$ s^{-1} and (b) 600 s^{-1}.

In order to identify the deformation mechanism of the filled composites till fracture, quasi-statically compression tested filled epoxy samples until about failure were further cut longitudinally in the mid section and metallograpically prepared for microscopic observations. High strain rate tested axially splitted filled composites samples surfaces were also polished for the microscopic observations. Figure 8.7(a) shows a crack formed in a quasi-statically tested sample. The crack deflection is clearly

seen in this figure. Away from the crack, debonded and fracture frustules are clearly see (Figure 8.7(b)). The cracks are observed to initiate at the debonded site of the frustules (Figure 8.7(c)). The deformation is seen to be not localized in quasistatically tested samples. Figure 8.8(a) show the high strain rate tested filled epoxy sample microstructure near the fracture site. No debonding is observed around the frustules. The crack proceeds in the epoxy matrices (Figure 8.8(b) and on the fracture site the frustules are pull out the epoxy matrices (Figure 8.8(c)). This shows that the failure of the filled composite at high strain rate is dominated by the fracture of the matrices, while debonding is dominated the quasi-static failure of the composite. The similar failure strains of the filled and neat epoxy samples at high strain rates tend to confirm that the failure is matrix-dominated.

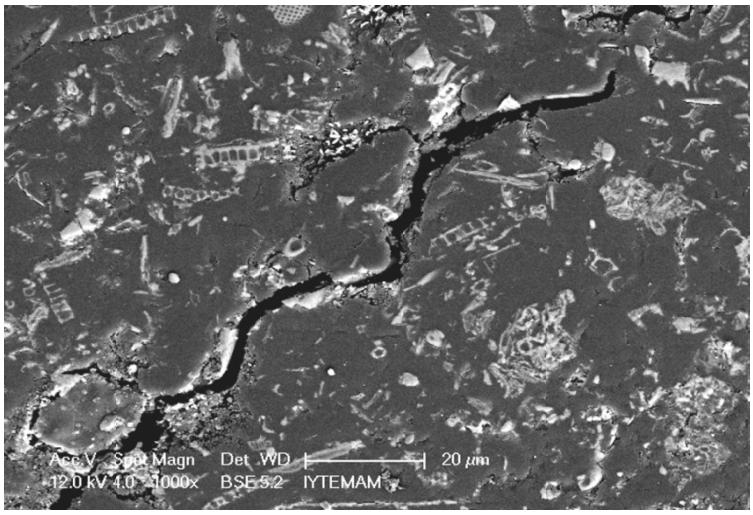

(a)

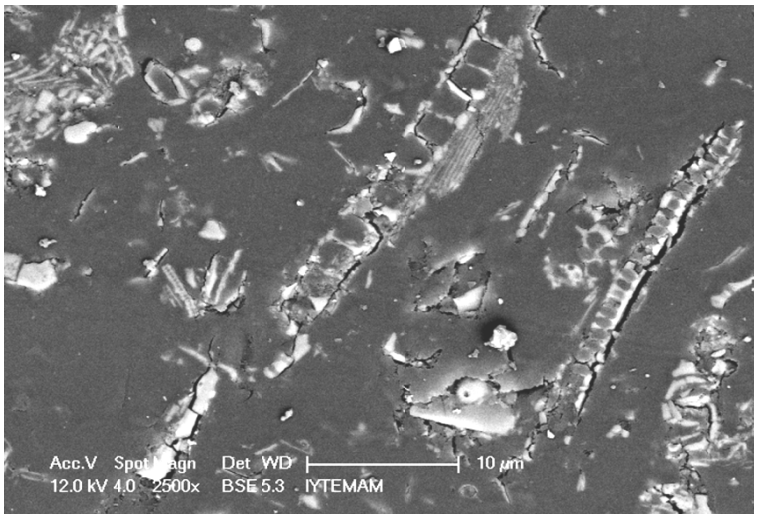

(b)

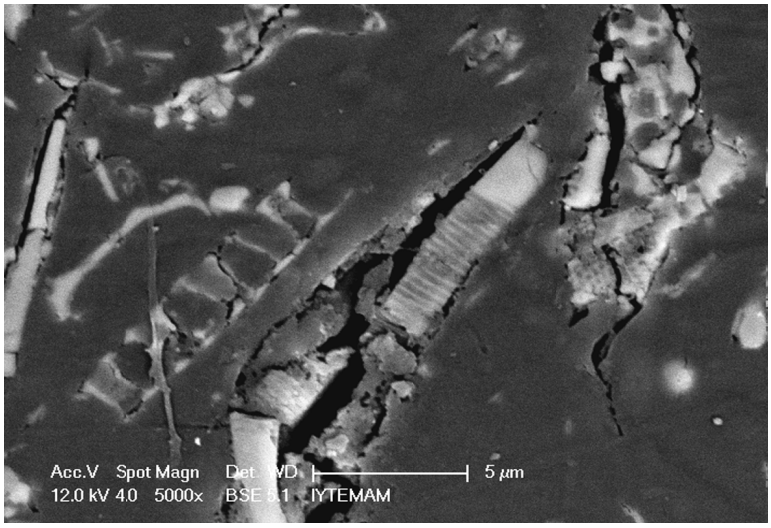

(c)

Figure 8.7. SEM micrograph of polished cross-section of 10.8 vol% ND filled epoxy samples tested at strain rate of $1x10^{-1}$ s^{-1}.

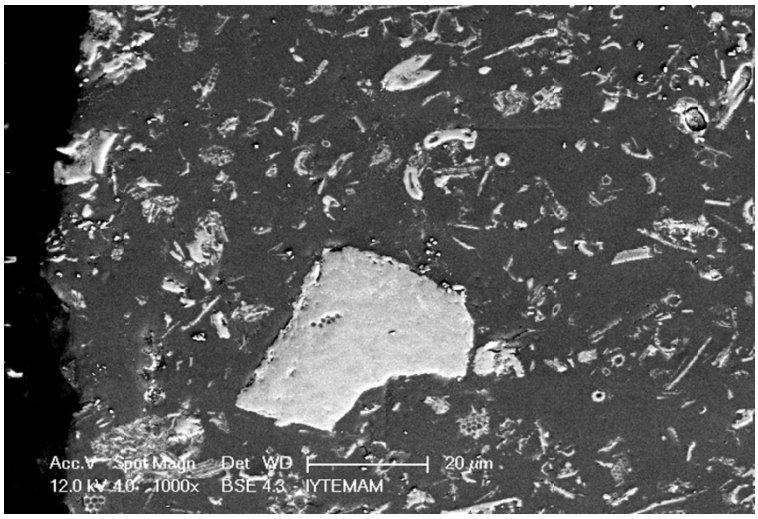

(a)

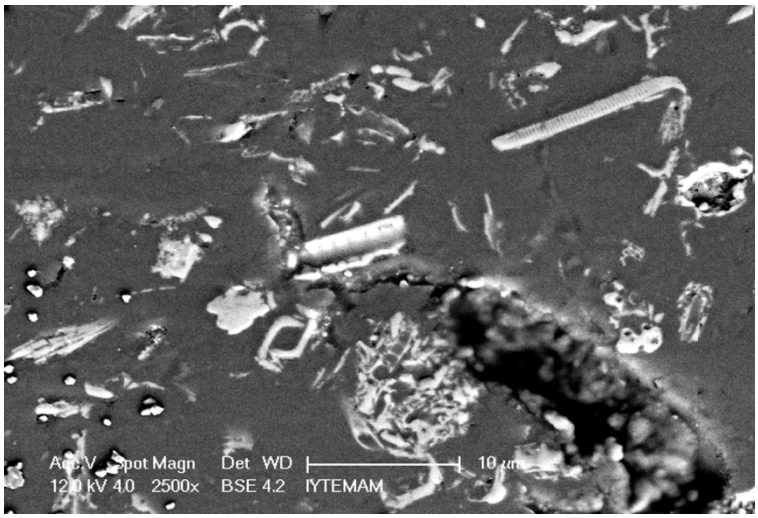

(b)

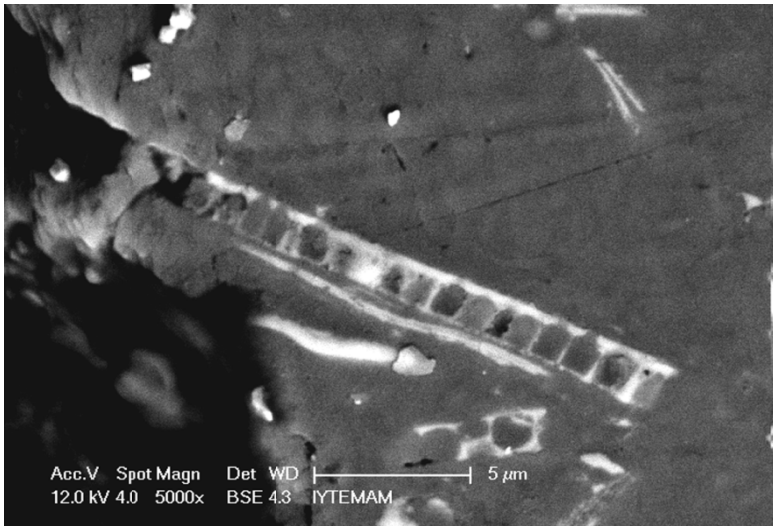

(c)

Figure 8.8. SEM micrograph of polished cross-section of 10.8vol% ND filled epoxy samples tested at strain rate of 600 s^{-1}.

SEM micrographs of ND and CD filled samples reveal that there is almost no agglomeration in the composites and and micromechanical bonding can be achieved by introducing the polymer matrix into the pore channels of inorganic fillers (Ji, et al. 2003). The restriction of silane coupling agents can be overcome by improving the bonding between filler and the matrix by mechanical interlocking of two phases. The micromechanical interlocking may improve the resistance to hydrolytic de-bonding at the filler-matrix interfaces (Praveen, et al. 2006). In this manner, the interlocking between epoxy and frustules plays a significance role on the mechanical properties of composites. SEM micrographs of fracture surface of tested samples exhibit pores and channels of frustules fully filled with epoxy. This shows a mechanical interlocking between frustules and epoxy.

8.2. Tensile Behavior

Typical tensile stress–strain curves for neat epoxy and its CD filled version are shown in Figure 8.9, indicating a reinforcing effect of CD frustules on the epoxy matrices. The composite elastic moduli are calculated by linear fitting of the initial portion of each curve. Generally, the elastic modulus increases and strain at break decreases with the addition of CD frustules except for 1.2 vol% addition.

Elastic modulus increases with increasing particle volume percentage, as seen in Figure 8.10. The modulus of epoxy resin increases from 2.6 MPa to 3.7 MPa with the addition of 11.3 vol% frustules. The variation of the ultimate tensile strength of neat and CD filled epoxy with volume percentage of the filler is shown in Figure 8.11. The incorporation of CD frustules leads to an increase in tensile strength of epoxy when particle addition reaches ≈8vol% except from 1.2 vol% CD, but then a drop in strength occurs. The decrease in tensile strength of CD/epoxy above 7.7vol% is believed due to the heterogeneous distribution of the CD frustules. The reduction in tensile strength at high filler loading may be due to the incomplete wetting of frustules or the existing of micro voids (Fu, et al. 2002).

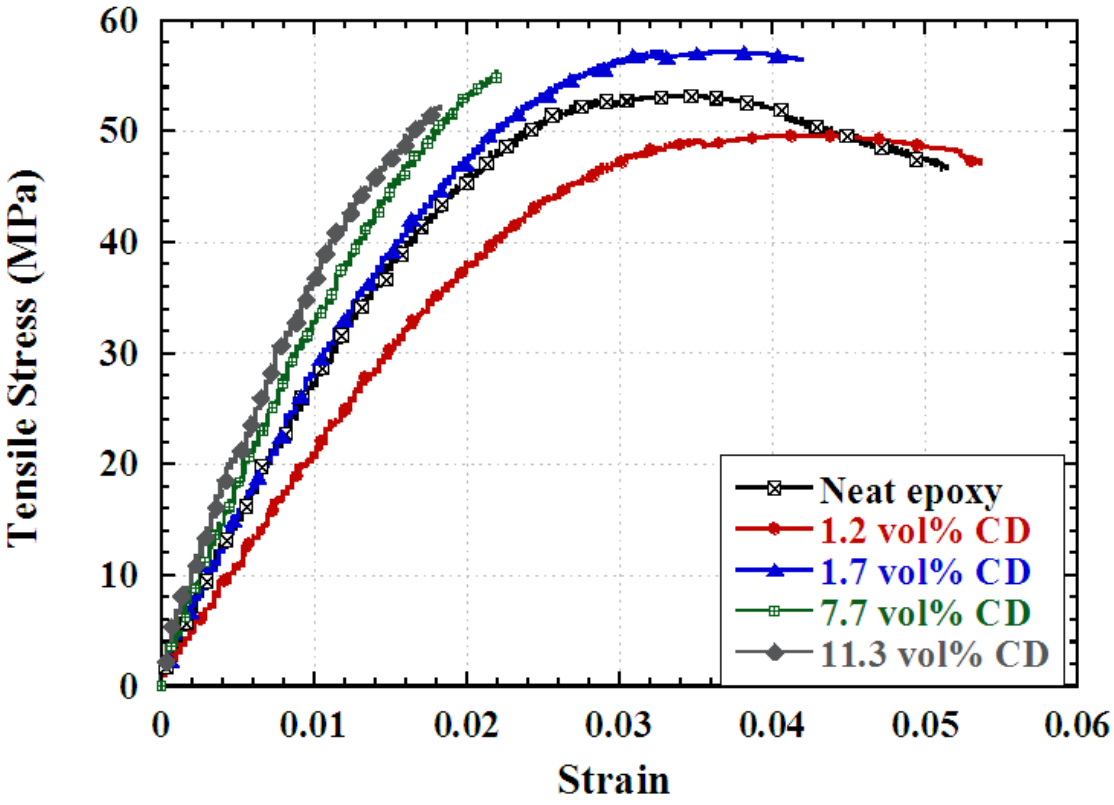

Figure 8.9. The stress-strain curves of neat and CD filled epoxy.

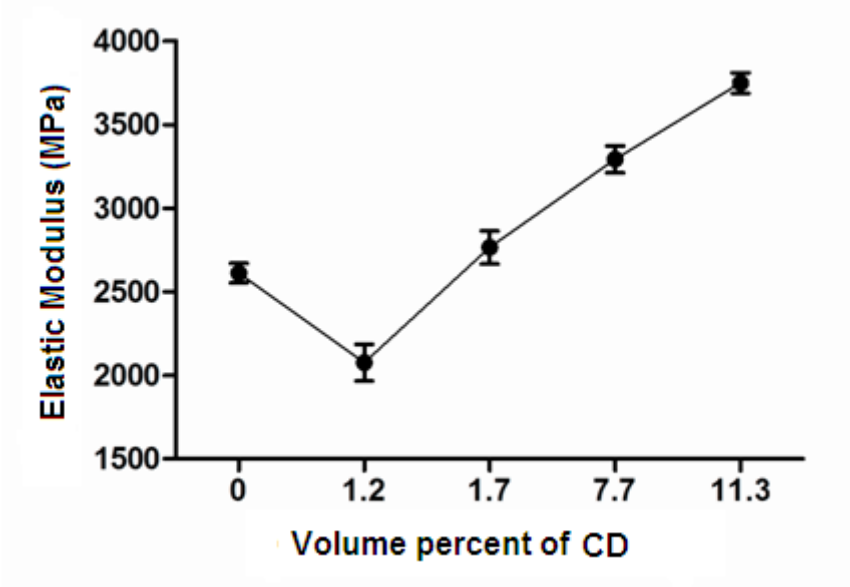

Figure 8.10. The effect of CD addition on the elastic modulus of the epoxy.

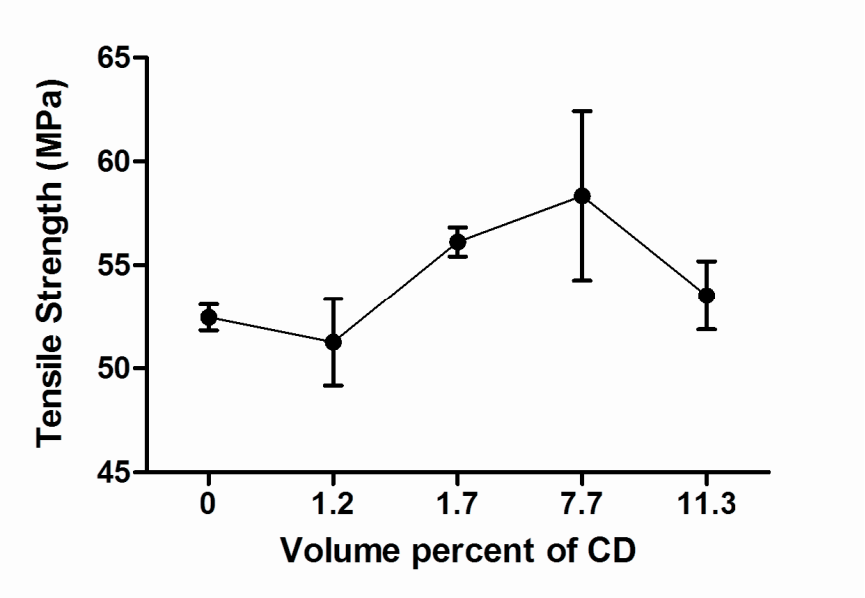

Figure 8.11. The effect of CD addition on the tensile strength of the epoxy.

The effect of frustule filling on the matrix, interfacial adhesion between frustules and epoxy and fracture modes of the composites are examined by the SEM of the fracture surface of composites. The tensile fracture surface of neat epoxy and 1.2, 7.7 and 11.3 vol% of CD frustules filled epoxy specimens are shown in Figures 8.12(a-d), respectively. The fracture surface of neat epoxy resembles the typical fracture surface expected from the brittle thermosetting matrices. As the frustules content increases, the fracture surface appearance changes from wavy form in neat epoxy to rough form. Moreover, the micrographs further show that the dispersion of frustules in epoxy matrix is relatively uniform and there is no agglomeration in the composites. This observation proves the efficient mixing of frustules in the matrix was obtained via melt mixing of frustules and epoxy. It is clearly seen in Figure 8.12(a) and (b) that the fracture surface of neat epoxy and 1.2 vol% CD filled epoxy is very much similar and relatively smooth and featureless. Figures 8.13(a) and (b) show the fracture surfaces of the neat and 7.7 vol% CD filled epoxy. These micrographs show the increased fracture surface roughness with frustules filling. In addition, frustules are completely embedded in the epoxy and show good adhesion to the epoxy matrix Figure 8.13(b). The tensile fracture surfaces of 1.2 vol% of CD filled epoxy are shown in Figures 8.14(a-d). Although, the volume content of CD frustules is relatively small, frustules are seen to be collected in a small region, showing in homogeneous distribution Figures 8.14(a) and (b). A closer examination of the fracture surface at a higher magnification shows the adhesion

between CD frustules and epoxy matrix (Figures 8.14(c) and (d)). Debonded interface is observed between CD and epoxy matrix Figure 8.14(c).

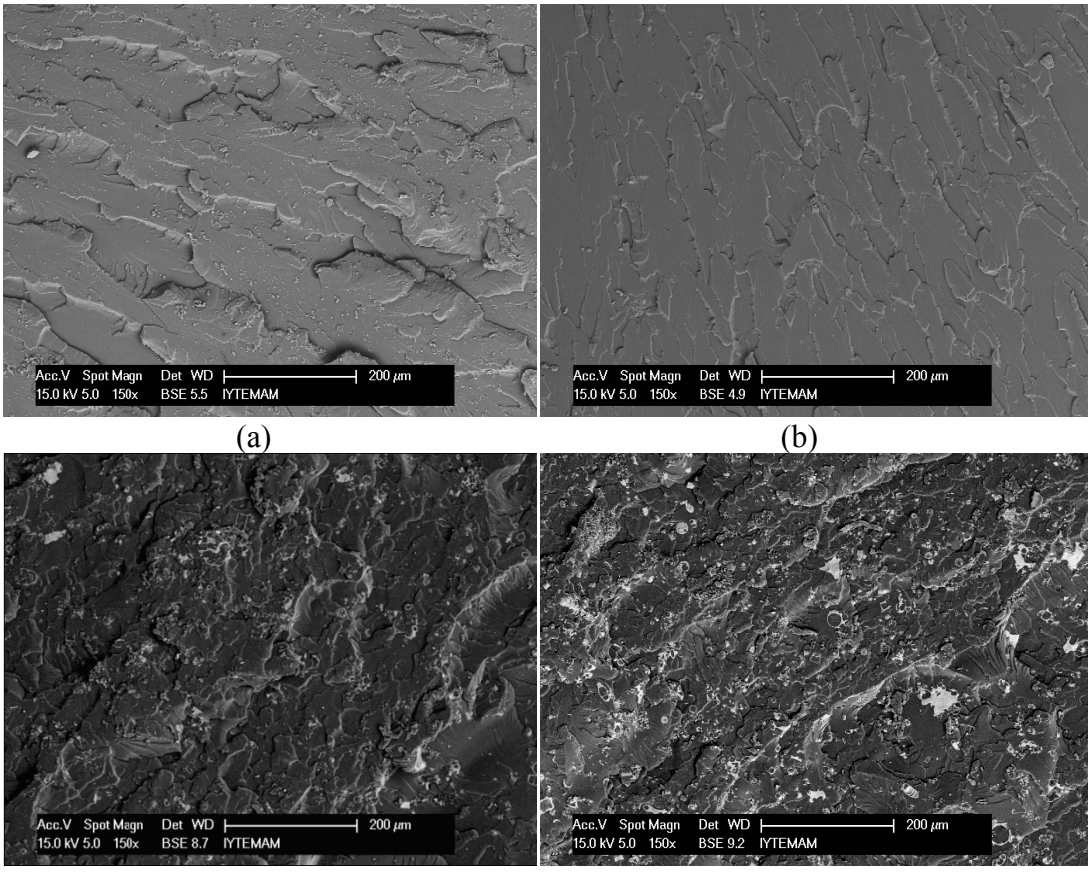

(a) (b)

(c) (d)

Figure 8.12. The SEM micrographs of fracture surfaces of (a) neat epoxy (b)1.2vol% filled, (c) 7.7 vol% filled and (d) 11.3 vol% filled epoxy.

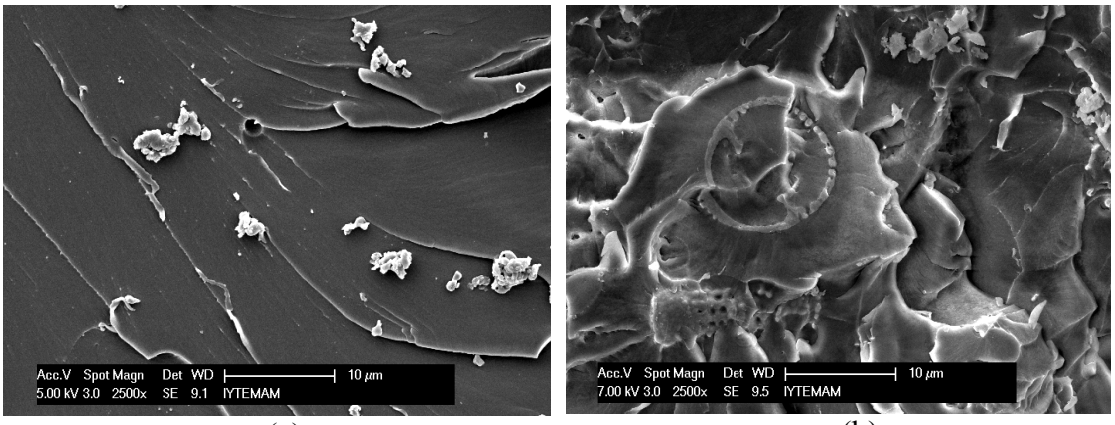

(a) (b)

Figure 8.13. The tensile fracture surfaces of (a) neat and (b) 7.7 vol% CD filled epoxy.

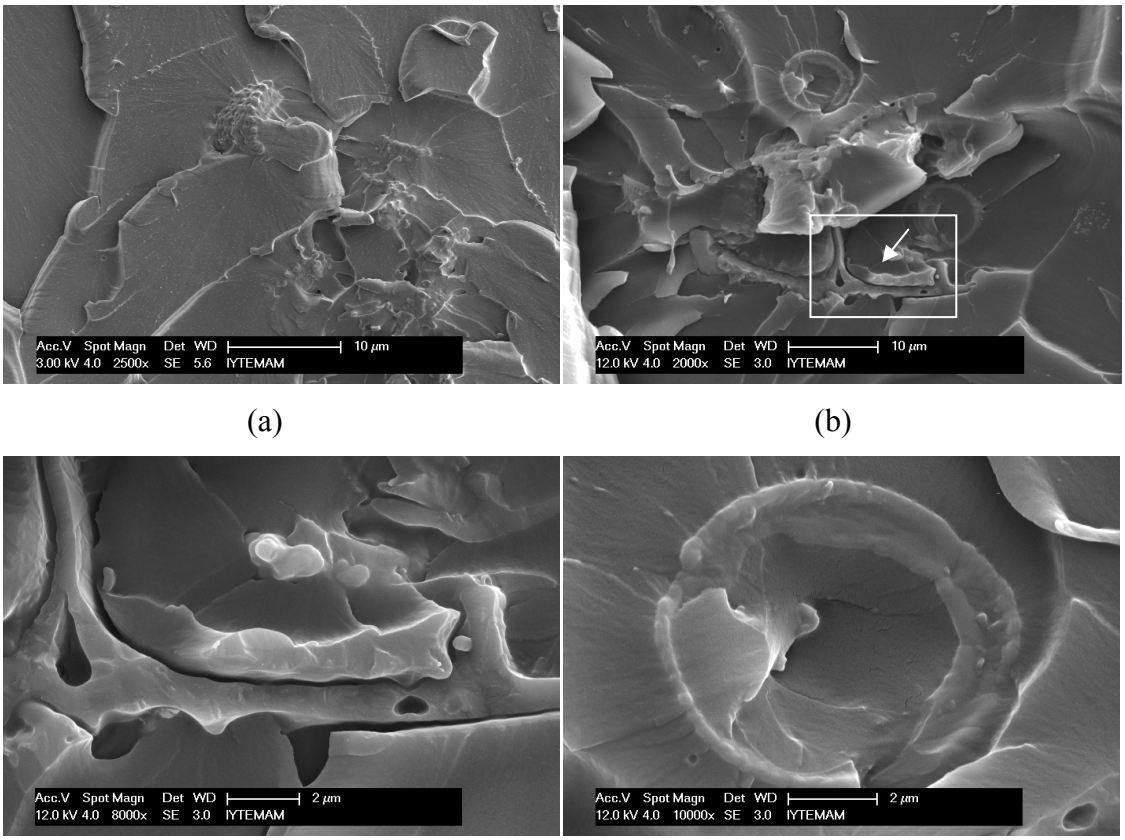

(a) (b)

(c) (d)

Figure 8.14. The SEM observation of fracture surface of 1.2 vol% CD filled epoxy.

SEM micrographs of the fracture surfaces of 11.3 vol% CD filled epoxy samples are shown in Figures 8.15(a-h). The general observation of fracture surfaces, frustules breakage and zigzag propagation of fracture due to frustules filling are seen Figure 8.15(a). This is an evidence of effective stress transfer between fiber and matrix. Figure 8.15(b) shows the crack initiation from the interface between matrix and frustules and single fracture of composites. Figures 8.15(c) and (d) show mechanical interlocking between two phases. Large size crushed frustules bonded to epoxy are seen in Figures 8.15 (e) and (f). The surface of the CD frustules is shown the part of epoxy resin, indicating that the adhesion between the particles and matrix is good (Figure 8.15 (g)). Figure 8.15(h) shows the debonded frustules and matrix crack growth in the same region. These SEM micrographs show the presence of mechanical interlocking between CD frustules and the epoxy matrix.

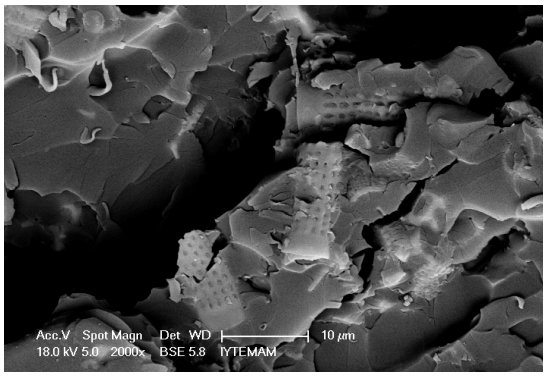

(a)

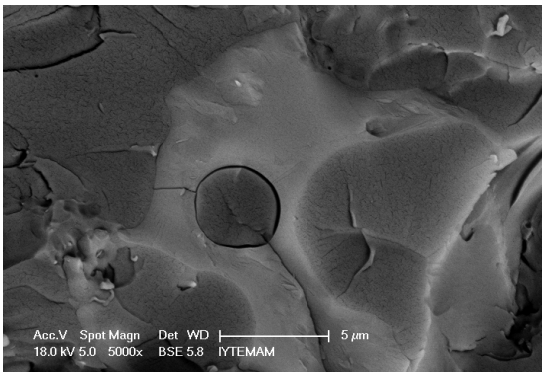

(b)

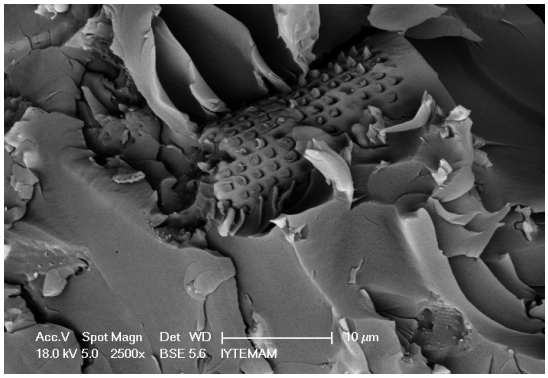

(c)

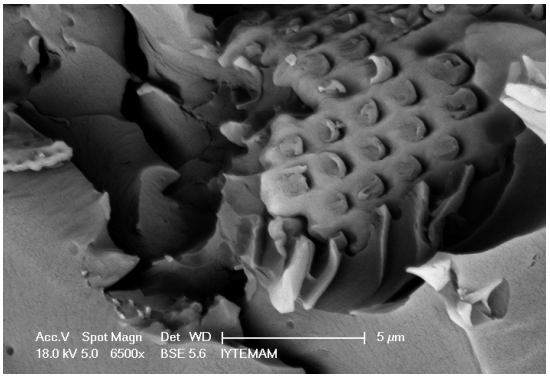

(d)

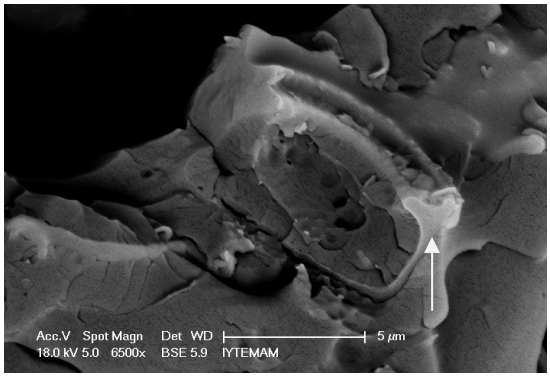

(e)

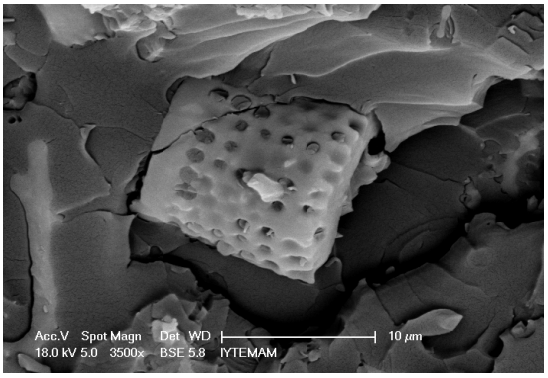

(f)

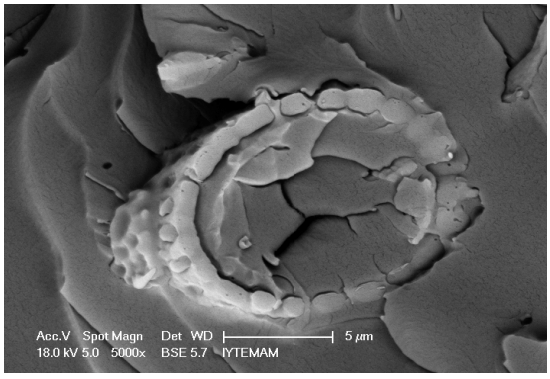

(g)

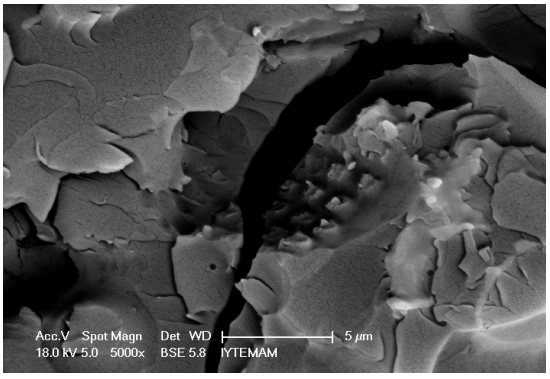

(h)

Figure 8.15. Fracture surfaces of CD filled epoxy samples.

Figure 8.16 shows tensile stress-strain curves of ND frustules filled epoxy. Generally, the elastic modulus increases and strain at break decreases with the addition of ND frustules except for 1.2 vol% addition, similar to CD filling. The variation of the elastic modulus of ND filled epoxy with the volume percent of ND is shown Figure 8.17. The elastic modulus increases with the addition of ND frustules up to 11.7 vol%. The elastic modulus increases from 2500 MPa to 4000 MPa at 11.7vol% ND frustule addition. The increases in elastic modulus are about 54%. The frustules filling decreases the tensile failure strains of the epoxy similar to CD filled epoxy composite. The effect of ND frustule on the tensile strength is shown in Figure 8.18. In general, the graph shows an increasing trend as the ND frustules volume percent increases.

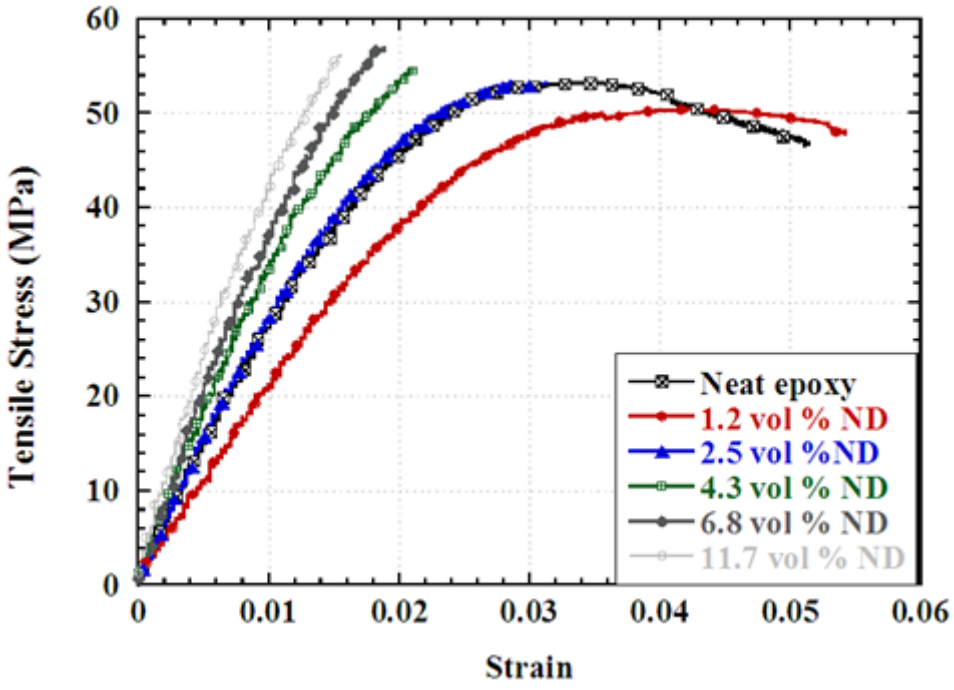

Figure 8.16. The stress-strain curves of neat and CD filled epoxy.

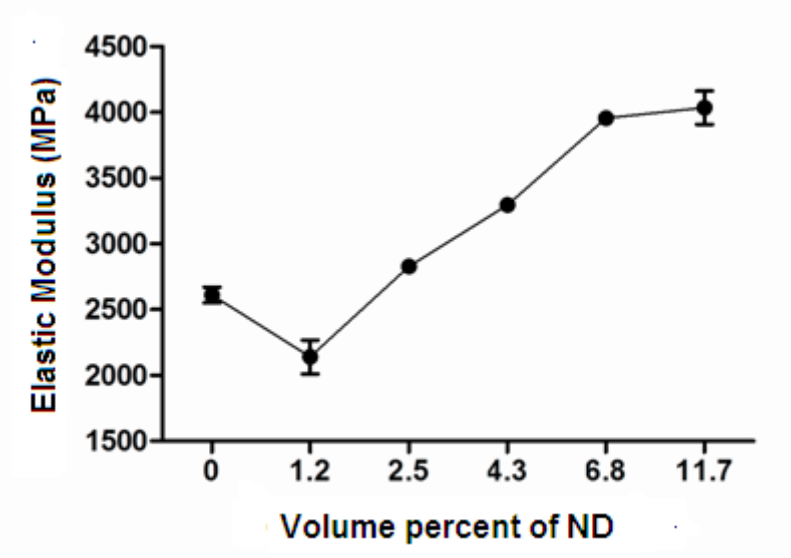

Figure 8.17. The effect of ND addition on the elastic modulus of the epoxy.

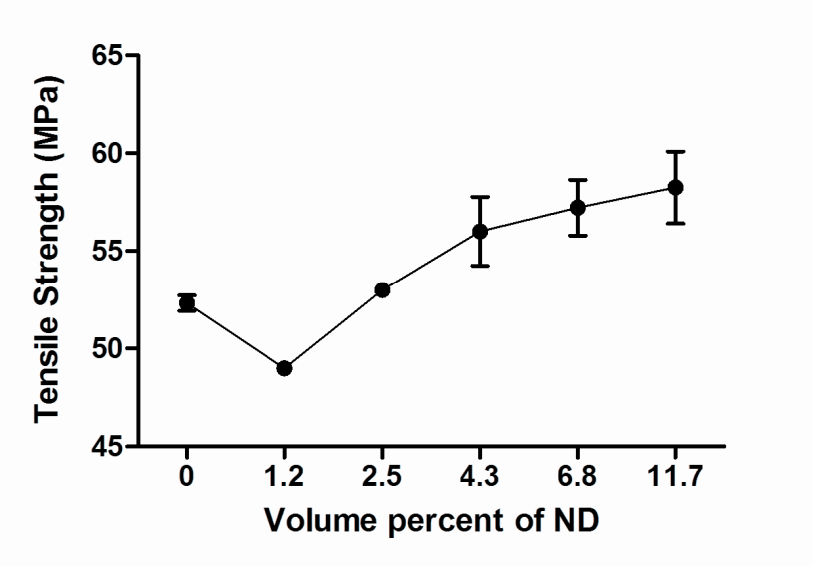

Figure 8.18. The effect of ND addition on the tensile strength of the epoxy

The tensile fracture surface SEM micrographs of 2.5, 4.3 6.8 and 11.7 vol% of ND frustules filled epoxy specimens are shown in Figures 8.19(a-d), respectively. At the same volume fraction, it is noted that ND frustules filled epoxy samples contain more diatom frustules on the fracture surface than CD frustules filled epoxy samples, simply arising from the smaller particles size of ND frustules. Because of this, the dimples on the surface are smaller and narrower in ND frustules filled fractured epoxy samples as compared with CD frustules filled epoxy.

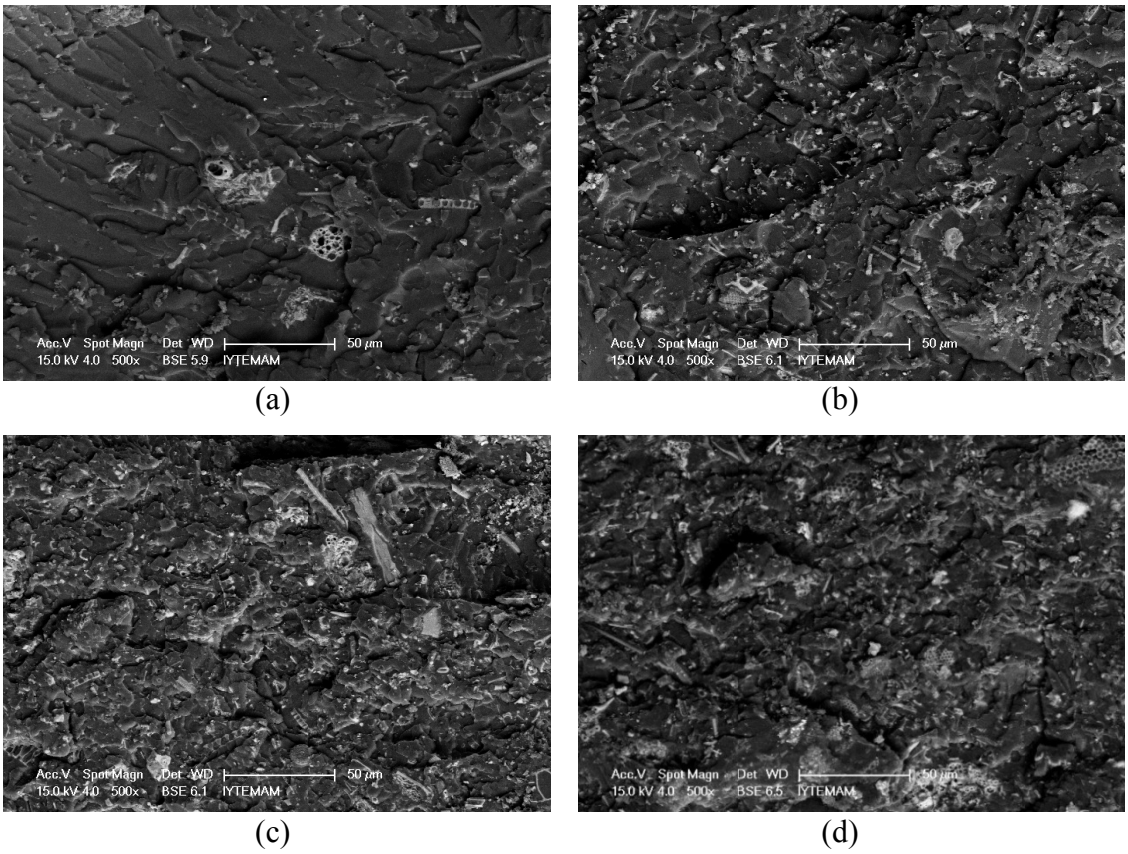

(a) (b)

(c) (d)

Figure 8.19 The fracture surfaces of (a) 2.5vol%, (b) 4.3vol%, (c) 6.8vol% and (c)11.7vol% ND filled epoxy composites.

Although, similar failure mechanism were observed in ND frustule filled epoxy, as the frustule shape and size are heterogeneous, the identification of the effect frustule alignment to loading axis is rather difficult. Fracture surfaces of 11.7 vol% ND filled epoxy specimens are seen in Figures 8.20(a-d). The fiber breakage between the pores, matrix cracking and frustule debonding are clearly seen in Figures 8.20(a) and (b). The cracks are seen in Figures 8.20(c) and (d) both proceed through the matrix and the frustule fracture and deflected the crack.

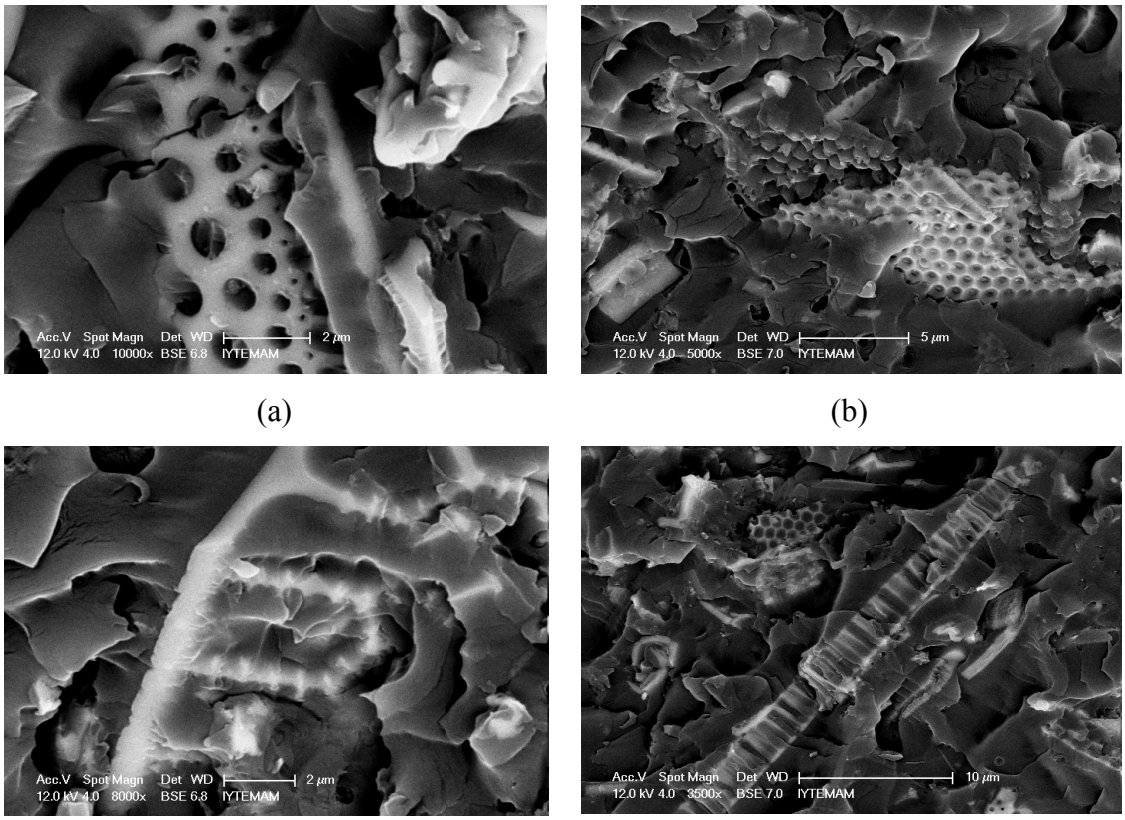

(a) (b)

(c) (d)

Figure 8.20 Fracture surfaces of 11.7vol%ND filled epoxy samples.

8.3. Projectile impact

Projectile impact tests were performed to the neat epoxy and 10.8vol% CD and ND filled epoxy samples. The test parameters; projectile velocity (V_0), volume percentage of frustules in the target material (V_f), mass of the target (M_t) and density of the target (ρ_t) are tabulated in Table 8.1. The impact velocity of projectile is 100,160 and 200 m/s. Neat and frustules filled epoxy panels are perforated, leaving a clean hole, at the impact velocities studied as shown in Figures 8.21(a-c), Figures 8.22(a-c) and Figures 8.23(a-c) for neat (NE) and CD and ND filled epoxies. The characteristic damage mechanisms for neat and frustules filled epoxy samples are the radial cracks, the cone cracks and the fragmentation of the cone. Similar damages were previously detected in polymer based composites (Sherman and Ben-Shushan 1998). It is also noted as the impact velocity increases the size of the cone decreases and the extent of crack formation decreases as seen in Figures 8.21(a-c) and Figures 8.22(a-c).

Table 8.1 Projectile impact test parameters.

Test Number	V_0 (m/sec)	V_f	Mt (g)	ρ_t (g/cm^3)
NE-1	100	0	472	1.165
CD-1	100	10.8	502	1.239
ND-1	100	10.8	521	1.286
NE-3	160	0	470	1.160
CD-3	160	10.8	496	1.224
ND-3	160	10.8	496	1.224
NE-5	200	0	469	1.157
CD-5	200	10.8	485	1.198
ND-5	200	10.8	502	1.241

(a) (b) (c)

Figure 8.21. Damage zone of the specimens after projectile test at 100 m/s: (a) neat epoxy, (b) 10.8vol% CD and (c) 10.8 vol% ND filled epoxy.

(a) (b) (c)

Figure 8.22. Damage zone of the specimens after projectile test at 160 m/s: (a) neat epoxy, (b) 10.8vol% CD and (c) 10.8 vol% ND filled epoxy.

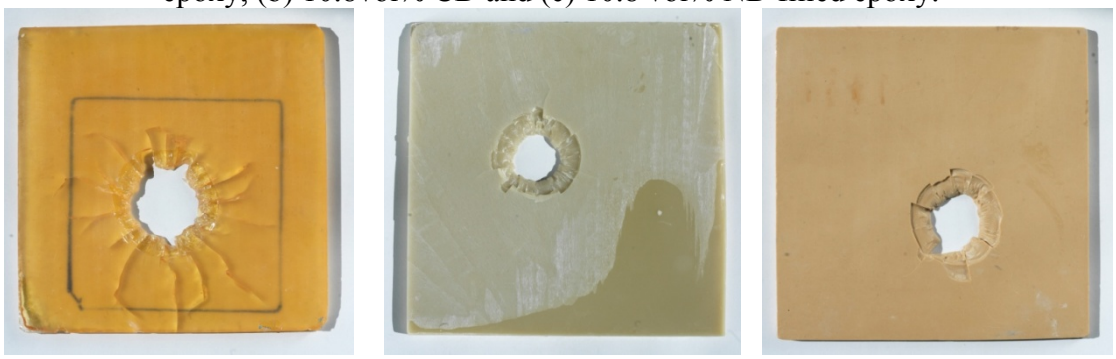

(a) (b) (c)

Figure 8.23 Damage zone of specimens after projectile test at 200 m/s: (a) neat epoxy, (b) 10.8vol% CD and (c) 10.8 vol% ND filled epoxy.

The cone crack formation is a major damage mechanism in brittle materials, especially thick ceramic plates (Hertz 1896, Wilkins 1978). The cone crack formation during ballistic test is related to the ballistic resistance improvement of the ceramic materials (Zhang, et al. 2010). According to Hetherington, (Hetherington 1992) the increment cone angle (Figure 8.24) can increase block effect of plate. The cone angle is as;

$$\theta = \arctan\left(\frac{d_2 - d_1}{2h_c}\right) \tag{8.1}$$

Where θ is the cone angle of panels, d_1 and d_2 are the top and bottom diameters of the cone, and h_c is the thickness of the panels. The top and bottom diameter of cone space of each plates are measured (Figure 8.25 (b)), the half cone angles of panels are calculated and tabulated in Table 8.2 together with the number of radial cracks. The crack generation and propagation on the panels change with the frustules filling and impact velocities. The cone diameter of 10.8 vol% frustules filled samples is smaller than that of neat epoxy at three different impact velocities. ND filled epoxy samples show smaller cone crack than CD filled epoxy samples at all impact velocities, proving a better ballistic resistance in ND filled samples. The produced fragments of the panels resulting from impact tests are collected (Figure 8.26), the size and weight of all fragments are measured and the results are tabulated in Table 8.3. The last column in Table 8.3 shows the total mass of the gathered fragments. Compare with Tables 8.1 and 8.3, it is shown that the mass destruction of the gathered material (due to scattering of fine particles) is less than 10%. The size of fragments is assumed linear and considered isometric.

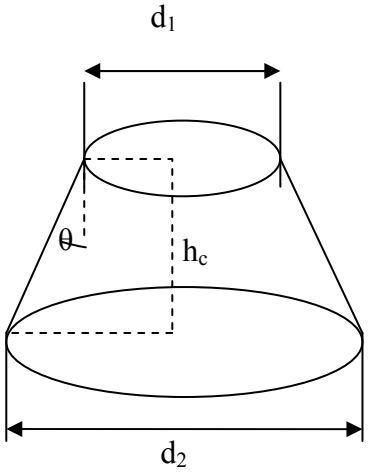

Figure 8.24 Schematic drawing of the inverse cone (Zhang, et al. 2010).

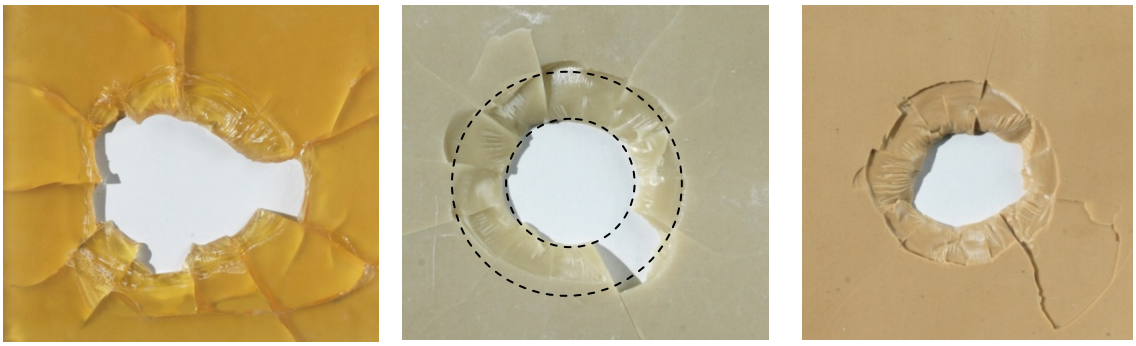

(a) (b) (c)

Figure 8.25 Cone region of specimens after projectile test at 100 m/s: (a) neat epoxy, (b) 10.8vol% CD and (c) 10.8 vol% ND filled epoxy.

Table 8.2. Damage parameters of epoxy panels.

Targets	d_1(mm)	d_2(mm)	θ (°)	Number of radial crack	Number of cone crack
NE-1	41.6	62.3	50.2	6	6
CD-1	27.7	47.2	50.6	1	9
ND-1	21.2	43.5	54.3	-	6
NE-3	25.1	46.1	52.6	2	8
CD-3	23.8	45.9	54.2	2	8
ND-3	23.3	46.3	55.2	3	4
NE-5	31.4	48.7	44.2	3	17
CD-5	20.1	40.4	51.7	-	10
ND-5	22.1	42.2	51.5	-	10

(a)

(b)

(c)

Figure 8.26 The fragments collected after test for (a) neat, (b) 10.8 vol% CD and (c) 10.8vol% ND filled epoxy samples at 100 m/s impact velocity.

Table 8.3. Mass of group of fragments and their weight.

Test Number	M (g) at d (mm)			Total mass (g)
	0-10	10-20	20-	
NE-1	-	3.19	38.4	41.6
CD-1	0.17	0.98	7.36	8.51
ND-1	0.32	2.89	3.12	6.33
NE-3	-	-	8.61	8.68
CD-3	0.37	3.36	0.69	4.43
ND-3	0.52	5.22	-	5.74
NE-5	0.15	2.23	3.45	5.83
CD-5	0.82	3.38	-	4.20
ND-5	0.21	4.53	0.70	5.48

The dimensions of the collected fragments are statistically analyzed using ANOVA test. There is no significant differences among the fragment size of NE, CD and ND filled epoxy samples at 160 m/s ($p > 0.05$) (Figure 8.26). The sizes of ND samples are significantly lower (13.05±5.07) than those of NE samples ($p<0.05$) while no differences with that of CD at velocity of 100 m/s ($p>0.05$). At highest velocities, there is no significant difference among the fragment size of all the samples ($p > 0.05$). The variation of fraction sizes of NE, ND and CD filled epoxy with frustule addition is shown in Figure 8.28. There is seen to be no important distinction in size of ND filled epoxy samples with changing impact velocity in Figure 8.28 ($p < 0.05$). At the velocity of 100 m/s, the sizes of CD filled epoxy samples are higher (19.13±7.75) than those of CD filled epoxy at 160 and 200 m/s impact velocities ($p < 0.05$). On the other hand, the fragment size of NE at 100 m/s is significantly higher (24.02±10.75) than size of NE samples at 200 m/s while there is no difference between the size of NE samples at 100 and 160 m/s impact velocity. The fracture of fine fraction increases with increasing impact velocity (Pilyugin 2008a). The dimensional analysis confirms that the size of fragments decrease with increasing impact velocity for NE and CD filled epoxy. On the other hand, ND frustules addition does not change the fragment size at all impact velocities.

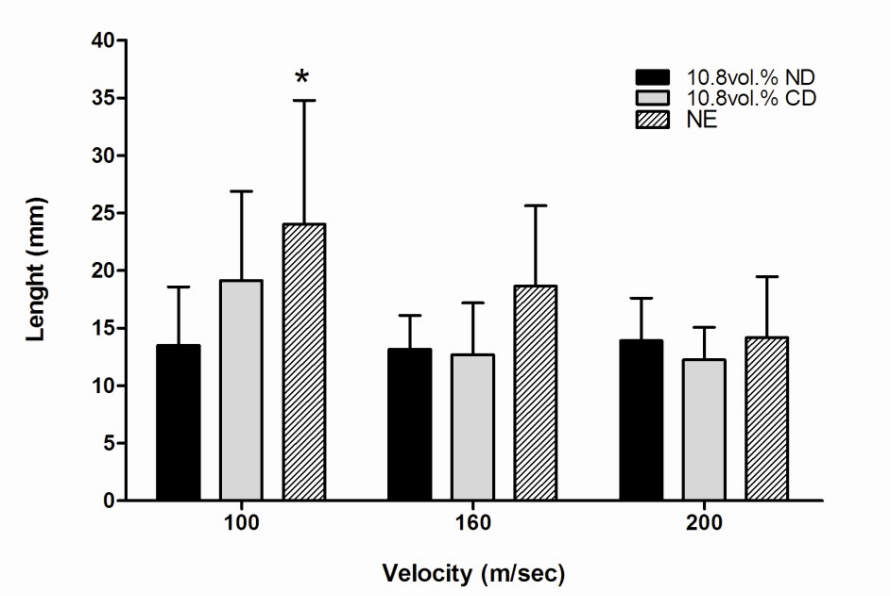

Figure 8.27 The variation particle size of NE, ND and CD filled epoxy with impact velocity ,*P<0.05 vs. 10.8vo.% ND sample at 100 m/s.

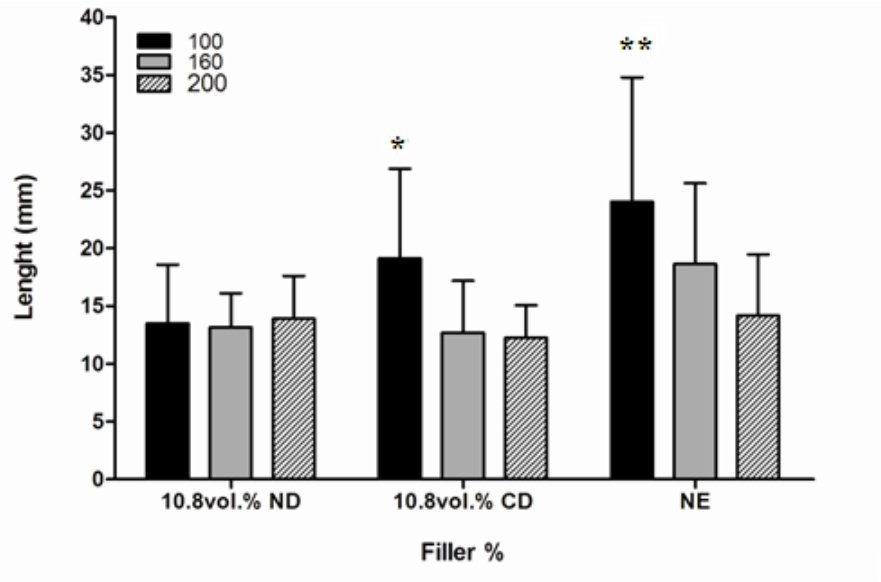

Figure 8.28 The variation of the fragment size of NE, ND and CD filled epoxy with impact velocity; *p<0.05 the size of 10.8vol% CD filled samples at 160 and 200 m/s **p<0.05 the size of NE samples at 200 m/s.

The failure mechanism of neat and CD and ND filled epoxy samples under impact loading is mainly formation of radial and cone cracks and the fraction of cone. Radial cracks are known to be tensile cracks and generally propagate below the contact zone on the surface. The local biaxial bending stresses in the contact zone produce radial cracks. Therefore, the bending stress promotes radial cracks occur (Sherman and

Ben-Shushan 1998, Zhang, et al. 2010). The cone crack formation occurs near the contact zone between projectile and panel and propagates to the bottom of the panels. Figures 8.29(a-d) show the SEM photographs of the cone surface near the bottom surface of neat and 10.8vol% ND filled epoxy samples at 100 m/s velocity, respectievly. Figures 8.29(a) and (b) show typical brittle fracture morphology of the neat epoxy. River patterns are formed through fracture surface and cracks propagate from front surface to the back surface of panels. The fracture surface of ND filled epoxy shows rougher surface and larger river type morphology.

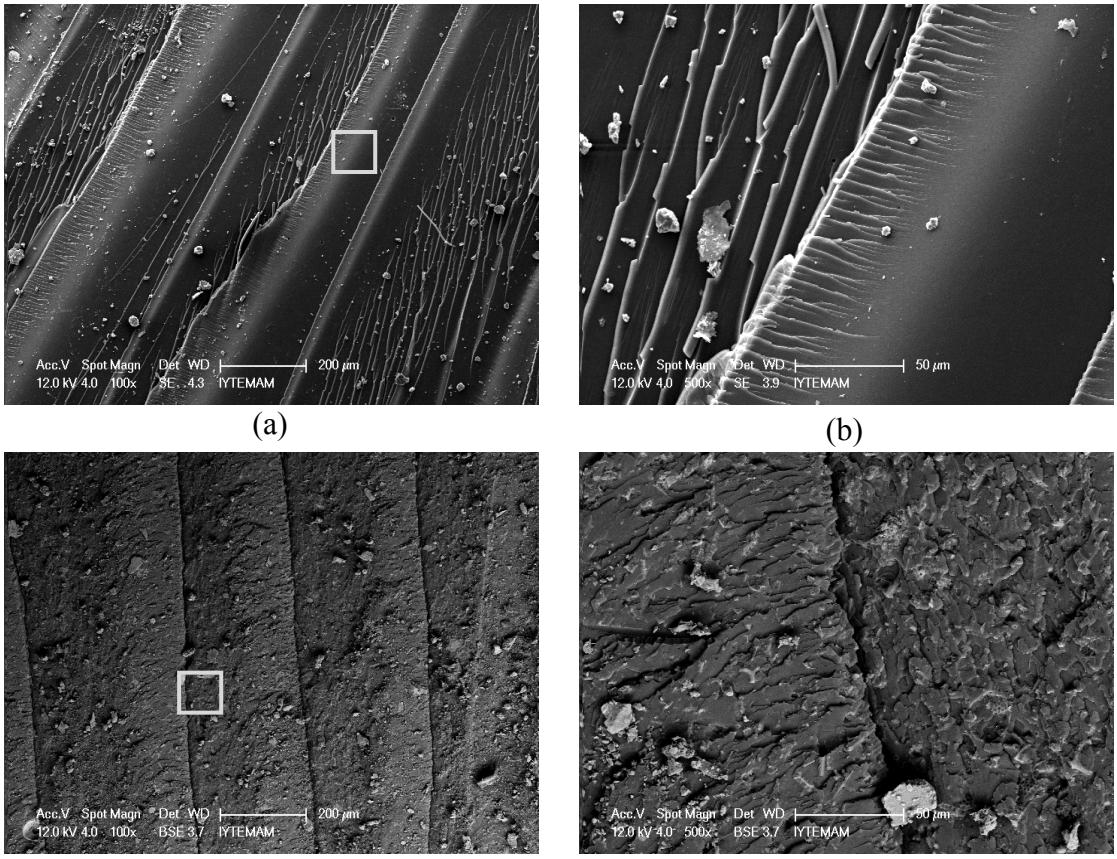

(a) (b)

(c) (d)

Figure 8.29. SEM micrographs showing the cone surface near the bottom surface of (a), (b) neat epoxy, (c) and (d) 10.8vol% ND filled samples at 100 m/s.

CHAPTER 9

THE PREDICTION OF MECHANICAL BEHAVIOR FRUSTULE FILLED COMPOSITES

A number of models have been proposed to predict the thermal and mechanical properties of short fiber and particulate reinforced composites. These composite models can be grouped into five basic models; law of mixtures, shear lag, laminated plate, Eshelby's and variational principle models. Theoretical analyses of elastic modulus can be classified for short fiber composites as, law of mixtures, the shear-lag model, the modified shear lag model and the Eshelby model. Law of mixtures and shear lag models give poor estimation of stiffness of a composite where the aspect ratio of short fibers is small (Taya and Arsenault 1989). In addition, semi-empirical Halpin Tsai and Guth models are used to estimate the mechanical properties of composites.

9.1. Law of Mixtures

It is considered a composite with N different reinforcing elements distributed in a matrix. Assume that each fiber has a shear modulus μ_i and volume fraction of fibers is V_i (i=1,2,3,…..N), and the shear modulus and volume fraction of matrix material are μ_0 and V_0 respectively. The shear modulus of composites μ_c is

$$\mu_c = \sum_{i=0}^{N} V_i \mu_i \tag{9.1}$$

where

$$\sum_{i=0}^{N} V_i = 1 \tag{9.2}$$

Assuming that the externally applied shear strain γ_a is equal to shear strains in all phases including the matrix can be explained as the average strain $\bar{\gamma}$ Since the stress in

the ith phase, σ_i is given by $\mu_i\bar{\gamma}$ the average stress in the composite $\bar{\sigma}$ can be approached by

$$\bar{\sigma} = \sum_{i=0}^{N} V_i\sigma_i = \sum_{i=0}^{N} V_i\mu_i\bar{\gamma} \tag{9.3}$$

On the other hand, the average stress $\bar{\sigma}$ is related to the applied strain $\gamma_a (= \bar{\gamma})$ by

$$\bar{\sigma} = \mu_c\bar{\gamma} \tag{9.4}$$

From equations (9.3) and (9.4) one can be obtained equation (9.1). If the shear moduli μ_c and are replaced by the strength of composite (σ_c) and reinforcing materials (σ_i), composite strength can be obtained by

$$\sigma_c = \sum_{i=0}^{N} V_i\sigma_i \tag{9.5}$$

In this case of two phase system, matrix and one kind of reinforced element, equation (9.5) can be written as

$$\begin{aligned}\sigma_c &= V_0\sigma_0 + V_1\sigma_1 \\ &= V_m\sigma_m + V_f\sigma_f\end{aligned} \tag{9.6}$$

where matrix and fiber were denoted m and f, respectively. The value predicted by law of mixtures is an upper bound, because the strain in the fiber and the matrix are not equal (Taya and Arsenault 1989).

9.2. Shear Lag Model

Shear lag model was developed by Cox (Cox 1952) and adequately predicts the stress transfer in fiber-reinforced composites, particularly for large differences in inclusion to matrix elastic modulus ratios (Nairn 1997). It is assumed that short fibers having uniform length and diameter are aligned in the loading direction and distributed uniformly throughout the material as seen in Figure 9.1(a). A unit cell shown in Figure 9.1(b) represents the basic model, in which short fiber surrounded by matrix. The other

boundary of the surrounding matrix is taken as mid-surface between two short fibers. This short fiber composite is subjected to the applied uniaxial strain e along the z-direction. Let the axial displacements in the fiber and the matrix on the boundary of the unit cell ($r = D/2$) be denoted by u and v respectively.

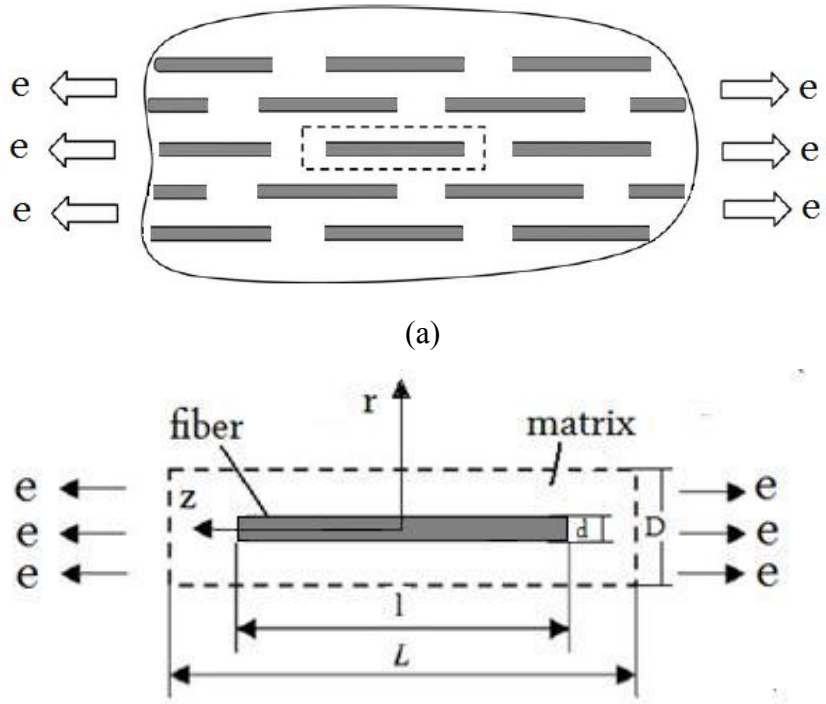

Figure 9.1. Shear lag model for aligned short fiber composite: (a) representative short fiberand(b) unit cell model for shear lag analysis
(Source:Taya and Arsenault 1989).

In addition, it is assumed that the difference in the axial displacements, $u - v$, is proportional to the shear stress at the matrix-fiber interface τ_0, or $d\sigma_f/d_z$, one can obtain z

$$\frac{d\sigma_f}{d_z} = -\frac{4\tau_0}{d} = h(u - v) \tag{9.7}$$

where, σ_f is the axial stress in the fiber and is a constant. The first equation in equation (9.7) was derived by considering the equilibrium of force along the z-direction. It is noted in equation (9.7) that the positive direction of shear stress τ_0 is taken to along the positive z-axis. In the fiber, Hooke's Law is valid

$$\sigma_f = E_f \frac{du}{dz} \tag{9.8}$$

where, E_f is the axial elastic modulus of the fiber. The applied composite strain e is the equal to dv/dz. Hence, from equations (9.7) and (9.8), ordinary differential equation is written as

$$\frac{d^2\sigma_f}{dz^2} = h(\frac{\sigma_f}{E_f} - e) \tag{9.9}$$

The general solution of equation (9.9) is given as

$$\sigma_f = E_f e + C_1 \cosh \beta z + C_2 \sinh \beta z \tag{9.10}$$

Where,

$$\beta = \sqrt{\frac{h}{E}} \tag{9.11}$$

and C_1 and C_2 are unknown constants. Applying boundary conditions, $\sigma_f = constant(\sigma_0)$ at $z = l/2$ and $d\sigma_f/dz = 0$ at $z = 0$, we obtain the stress field in the fiber is

$$\sigma_f = E_f e \left\{ 1 + \frac{\left(\frac{\sigma_0}{E_f e} - 1\right) \cosh \beta z}{\cosh\left(\frac{\beta l}{2}\right)} \right\} \tag{9.12}$$

It is noted in equation (9.12) that $\sigma_0 = 0$ was used in the original derivation of Cox (Cox 1952), but σ_0 may not be zero for the case of strongly bonded fiber ends. The average fiber stress σ_f is computed as

$$\begin{aligned} \bar{\sigma_f} &= \frac{2}{l} \int_0^{1/2} \sigma_f dz \\ &= E_f e \left\{ 1 + \frac{\left(\frac{\sigma_0}{E_f e} - 1\right) \cosh\left(\frac{\beta l}{2}\right)}{\cosh\left(\frac{\beta l}{2}\right)} \right\} \end{aligned} \tag{9.13}$$

Consider the displacement along the z-direction at an arbitrary point $(r = r)$ in the matrix, w, where $w(r = d/2) = u$, and $w(r = D/2) = v$. Force equilibrium at $r = (d/2)$ and an arbitrary point $(r = r)$ provides

$$2\pi r\tau = 2\pi\left(\frac{d}{2}\right)\tau_0 \tag{9.14}$$

The shear strain at $r = r$, γ is related to τ_0 as

$$\gamma = \frac{dw}{dr} = \frac{\tau}{G_m} = \frac{\tau_0}{2G_m}\frac{d}{r} \tag{9.15}$$

where, τ is the shear stress in the matrix at $r = r$, and G_m is the shear modulus of the matrix. Integrating equation (9.15) from $= (d/2)$ to $r = (D/2)$, one can obtain

$$v - u = \frac{\tau_0 d}{2G_m} ln\left(\frac{D}{d}\right) \tag{9.16}$$

From equations (9.7) and (9.16), the constant is

$$h = \frac{8G_m}{d^2 \ln(D/d)} \tag{9.17}$$

From equations (9.11) and (9.17), β is found as

$$\beta = \frac{2\sqrt{2}}{d}\sqrt{\frac{G_m/E_f}{\ln(D/d)}} \tag{9.18}$$

The average stress σ_f in the fiber is calculated from equation (9.13). To obtain the average stress in the composite along the loading (z) direction, σ_c can be estimated by using the law of mixtures, equation (9.6), where $\overline{\sigma_m}$ and $\overline{\sigma_f}$ are interpreted as the average quantities in the relevant domain,

$$\sigma_c = \left(1 - V_f\right)\overline{\sigma_m} + V_f\overline{\sigma_f} \tag{9.19}$$

where, V_f is the volume fraction of fiber. For a given applied strain e, one can assume that

$$\overline{\sigma_m} = E_m e \tag{9.20}$$

$$\sigma_c = E_c e \tag{9.21}$$

Substitution of equations (9.13), (9.20) and (9.21) into equation (9.19) yields the composite elastic modulus as E_c

$$E_c = \left(1 - V_f\right)E_m + V_f E_f \left\{1 - \frac{\tanh\left(\frac{\beta l}{2}\right)}{\frac{\beta l}{2}}\right\} \tag{9.22}$$

where, $\sigma_0 = 0$ (no load transfer at fiber ends) is assumed. If $\sigma_0 = \sigma_m$ is assumed, then

$$E_c = \left(1 - V_f\right)E_m + V_f E_f \left\{1 - \frac{\left(\frac{E_m}{E_f} - 1\right)\tanh\left(\frac{\beta l}{2}\right)}{\frac{\beta l}{2}}\right\} \tag{9.23}$$

9.3. Modified Shear Lag

According to classical shear-lag model (Cox 1952), the fiber is supposed to support only the axial load, the matrix is supposed to transmit only the shear stress, and no load is transferred through the fiber ends (i.e. the fiber ends are debonded from the matrix) (Hsueh 2000). When the fiber is bonded with fiber ends, the stress at the fiber ends has a finite value, and this stress is demanded as a boundary condition due to obtain the stress distribution in the fiber. The use of classical shear lag model causes difficulties because this finite stress is not decided beforehand value. The representative volume element was given for Shear Lag Model in Figure 9.2.

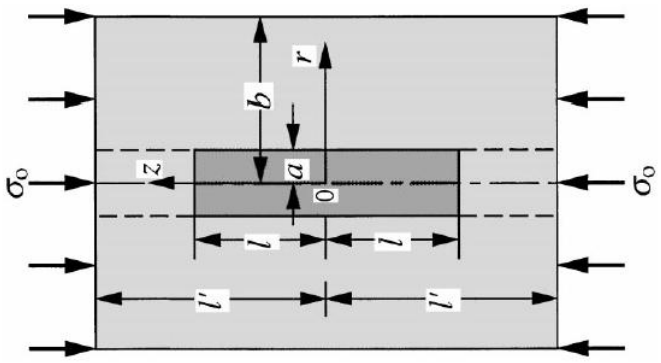

Figure 9.2. A representative volume element in modified shear lag model (Source:Hsueh 2000).

In the modified shear-lag model (Hsueh 1995, Hsueh, et al. 1997), the radial dependence of the axial stress in the matrix is included in the analysis, the axial-stress distribution in the represented volume elements is at equilibrium with the applied load, the shear-stress distribution in the matrix fulfills the free surface condition at r=b, and the boundary condition at the bonded fiber ends is determined by the condition at z±l. The matrix connecting the fiber ends to the surface of the representative volume element is treated as two imaginary fibers, which have the matrix properties. Hence, the stress-transfer problem (Figure 9.2) can be solved using two shear-lag models: one for 0≤z≤ l and one for l≤z≤l'. Although the stress at the fiber end is unknown, the two shear-lag models are jointed at z = l with the continuity condition, which, in turn, determines the stress at the fiber end. A technique developed earlier by Fukuda and Chou (Fukuda and Chou 1981) by introducing a partially axial load into the matrix in the classical shear-lag model is found to be similar to the ``imaginary fiber'' technique. Using the methodology described above, the stress transfer problem was analyzed previously by also including Poisson's effect and residual thermal stresses (Hsueh, et al. 1997). In order to simplify the equations, both Poisson's effect and residual thermal stress are removed from the analysis, and the axial stress distributions in the fiber and the imaginary fiber σ and σ_f',

$$\sigma_f = \frac{b^2 E_f \sigma_0}{a^2 E_f + (b^2 - a^2) E_m} + A[exp(\alpha z) + \exp(-\alpha z)]$$

$$(for\ 0 \le z \le l) \tag{9.24.a}$$

$$\sigma_f' = \sigma_0 + A'\left[\exp(\alpha' z) - exp[\alpha'(2l' - z)]\right]$$
$$for\ l \le z \le l' \tag{9.24.b}$$

where

$$\alpha = \frac{1}{a}\left\{\frac{a^2+\left(b^2-a^2\right)\frac{E_m}{E_f}}{b^2\left[\frac{b^2}{b^2-a^2}ln\left(\frac{b}{a}\right)-\frac{3b^2-a^2}{4b^2}\right](1+v_m)}\right\}^{\frac{1}{2}} \tag{9.25.a}$$

$$\alpha' = \frac{1}{a}\left\{\frac{1}{\left[\frac{b^2}{b^2-a^2}ln\left(\frac{b}{a}\right)-\frac{3b^2-a^2}{4b^2}\right](1+v_m)}\right\}^{\frac{1}{2}} \tag{9.25.b}$$

$$A = \frac{(b^2-a^2)\left(E_m-E_f\right)\sigma_0}{a^2E_f+(b^2-a^2)E_m}\left\{\exp(\alpha l)+\exp(-\alpha l)\right.$$
$$\left.-\frac{\alpha[\exp(\alpha l)-\exp(-\alpha l)\{\exp(\alpha' l)-exp[\alpha'(2l'-l)]\}]}{\alpha'\{\exp(\alpha' l)+exp[\alpha'(2l'-l)]\}}\right\}^{-1} \tag{9.26.a}$$

$$A' = \frac{\alpha[\exp(\alpha l)-\exp(-\alpha l)]A}{\alpha'\{\exp(\alpha' l)+exp[\alpha'(2l'-l)]\}} \tag{9.26.b}$$

It is noted that although the modified shear-lag model is much more rigorous than the classical shear-lag model, it is not exact and approximations are adopted in deriving the axial stress in the matrix. Also, the axial displacement is non-uniform on the faces of the represented volume element. In this case, the effective elastic modulus of the volume element in the axial direction is dictated by the average axial displacement at $z = l'$ under the axial loading stress, σ_0. The average axial displacement at $z = l$ is

$$w = \frac{2}{b^2}\left(\int_0^a r\int_0^l \frac{\sigma_f}{E_f}dzdr + \int_a^b r\int_0^l \frac{\sigma_m}{E_m}dzdr\right) \tag{9.27}$$

where, $\sigma_m$is the axial stress in the matrix. It is noted that whereas the radial dependence of $\sigma_f$is ignored in both the classical and the modified shear-lag models as a result of the relatively small fiber radius, the radial dependence of σ_m is considered in the modified shear-lag model, i.e. $\sigma_f(z)$ and $\sigma_m(r,z)$ are considered in the analysis. However, the explicit expression of σ_m is not required in equation (9.27) in order to solve w. This is

because the mechanical equilibrium condition requires

$$2\int_0^a r\sigma_f dr + 2\int_a^b r\sigma_m dr = b^2\sigma_0 \tag{9.28}$$

The combination of equation (9.27) and (9.28) yields

$$w = \frac{l\sigma_0}{E_m} + \frac{a^2}{b^2}\left(\frac{1}{E_f} - \frac{1}{E_m}\right)\int_0^l \sigma_f dz \tag{9.29}$$

Substitution of equation (9.24.a) into equation (9.29)

$$w = \frac{l\sigma_0}{E_m} + \frac{a^2}{b^2}\left(\frac{1}{E_f} - \frac{1}{E_m}\right)\left\{\frac{lb^2E_f\sigma_0}{a^2E_f+(b^2-a^2)E_m} + \frac{A}{\alpha}[exp(\alpha l) - exp(-\alpha l)]\right\} \tag{9.30}$$

Similarly, the average axial displacement at $z = l'$ relative to $z = l$ can be derived from

$$w = \frac{2}{b^2}\left(\int_0^a r\int_l^{l'}\frac{\sigma_f'}{E_m}dzdr + \int_a^b r\int_l^{l'}\frac{\sigma_m}{E_m}dzdr\right) \tag{9.31}$$

Such that ‘

$$w' = \frac{(l'-l)\sigma_0}{E_m} \tag{9.32}$$

Hence, the average axial displacement at $z = l'$, $w_0(= w + w')$, is

$$w_0 = \frac{l'\sigma_0}{E_m} + \frac{a^2}{b^2}\left(\frac{1}{E_f} - \frac{1}{E_m}\right)\left\{\frac{lb^2E_f\sigma_0}{a^2E_f+(b^2-a^2)E_m} + \frac{A}{\alpha}[exp(\alpha l) - exp(-\alpha l)]\right\} \tag{9.33}$$

The effective elastic modulus of the representative volume element in the axial direction, E_0, can be related to the loading stress, the average axial displacement at $z = l'$, and the length of the volume element, such that

$$E_0 = \frac{l'\sigma_0}{w_0} \tag{9.34}$$

A closed-form solution for $E_0$is hence obtained (Hsueh 2000).

9.4. Eshelby Model

Eshelby model is based on the elastic stress field around an ellipsoidal particle in an in finite matrix (Eshelby 1957, Eshelby 1961). Although, the Eshelby model cannot be used to predict the stress transfer, gives a good approach to predict elastic modulus of short fiber composites (Hsueh 2000). The Cartesian coordinates, X_1, X_2, and X_3, are used, and X_3 is the axis of symmetry of the ellipsoidal inclusion. A stress, σ_0, is applied to the composite in the X_3 direction. In this case, the remote applied strains, ε_{ij}^a, become

$$\varepsilon_{11}^a = \varepsilon_{22}^a = \frac{-v_m \sigma_0}{E_m} \tag{9.35.a}$$

$$\varepsilon_{33}^a = \frac{\sigma_0}{E_m} \tag{9.35.b}$$

where, v is Poisson's ratio. In the absence of the inclusion, the deformation throughout the system is uniform, i.e., the applied strain ε_{ij}^a. However, because of the presence of the inclusion, the deformation in the inclusion is perturbed, and the strain due to this perturbation is defined as the constrained strain. ε_{ij}^c. To solve this problem, the true inclusion is replaced by an equivalent inclusion, which has the same elastic constants as the matrix and undergoes an equivalent transformation strain, ε_{ij}^t. However, this replacement is subjected to the requirement that the displacement and the stress within the true and the equivalent inclusions are identical, such that (Eshelby 1957)

$$K_e(\varepsilon^c + \varepsilon^a) = K_m(\varepsilon^c + \varepsilon^a - \varepsilon^t) \tag{9.36.a}$$

$$G_e\left('\varepsilon_{ij}^c + '\varepsilon_{ij}^a\right) = G_m\left('\varepsilon_{ij}^c + '\varepsilon_{ij}^a - '\varepsilon_{ij}^t\right) \tag{9.36.b}$$

where, K and G are the bulk modulus and the shear modulus, the subscript, e, denotes the ellipsoidal inclusion, and ε and $'\varepsilon_{ij}$ are the dilatational and the deviatoric strains, respectively. When the volume fraction of inclusions is finite, the constrained strain in the inclusion consists of two components, such that (Mori and Tanaka 1973)

$$\varepsilon_{ij}^c = \varepsilon_{ij}^{c\prime} + \varepsilon_{ij}^{c\prime\prime} \tag{9.37}$$

where, $\varepsilon_{ij}^{c\prime}$ is the constrained strain component when a single inclusion is embedded in an infinite matrix, and it can be related to the transformation strain by (Eshelby 1957)

$$\varepsilon_{ij}^{c\prime} = S_{ijkl}\varepsilon_{kl}^{t} \tag{9.38}$$

where, S_{ijkl} is the Eshelby tensor and is a function of the aspect ratio of the inclusion and Poisson's ratio of the matrix. The second constrained strain component, $\varepsilon_{ij}^{c\prime\prime}$ is introduced to account for the effect of the presence of other inclusions on an inclusion, and can be related to the transformation strain by (Mori and Tanaka 1973)

$$(1-f)\varepsilon_{ij}^{c\prime\prime} + f\left(\varepsilon_{ij}^{c} - \varepsilon_{ij}^{t}\right) = 0 \tag{9.39}$$

The solutions of the strain components, ε_{ij}^{c} and ε_{ij}^{t} can be obtained by solving equations (9.35)-(9.39). The stress in the ellipsoidal inclusion in the loading direction, σ_e, can be derived from the stress/strain relationship, such that (Eshelby 1957)

$$\sigma_e = \frac{v_e E_e(\varepsilon^c + \varepsilon^a)}{(1+v_e)(1-2v_e)} + \frac{E_e(\varepsilon_{33}^c + \varepsilon_{33}^a)}{1+v_e} \tag{9.40}$$

The effective elastic modulus of the composite along the loading direction, E_o, can be obtained by dividing the applied stress with the average strain in the composite in the loading direction, such that (Withers, et al. 1989)

$$E_0 = \frac{\sigma_q}{\varepsilon_{33}^a + f\varepsilon_{33}^t} \tag{9.41}$$

It is noted that formulations of the solutions of ε_{ij}^{c} and ε_{ij}^{t} (and hence $\sigma_e$and E_o) are lengthy and have been obtained by Tandon and Weng (Hsueh 2000, Tandon and Weng 1984).

9.5. Halphin Tsai Model

Halpin-Tsai equations are widely used expressions in order to predict

reinforcement effect of fillers in micro-composite systems with both spherical (or near spherical) and non-spherical filled systems. Halpin-Tasi equations was modified by Halphin-Kardos (J. C. Halpin 1976) for the plate-like filler as expressed in the following form;

$$E_c = \frac{E_m(1+\xi\eta Vf)}{1-\eta Vf} \tag{9.42.a}$$

$$\eta = \frac{E_f / E_m - 1}{E_f / E_m + \xi} \tag{9.42.b}$$

Here, E_f denotes elastic modulus of the filler, and ξ is the shape factor depending on the filler orientation and loading direction. For the rectangular plate-like filler in a composite system, ξ is equal to 2w/t, in which w is the width and t is the thickness of the dispersed phase. The aspect ratio α has very significant effect on elastic modulus of the composite even at low volume fraction of the filler.

9.6. Guth Model

The relations between the elastic modulus and the concentration of filler given by Guth (Guth 1945) for non-spherical filled particulate composites. This modified model considers the chains composed of spherical fillers that are similar to rod like filler particles embedded in a continuous matrix. By introducing a shape factor to original Guth and Gold equation, Guth developed a new expression as in the following form:

$$E_c = E_m[1 + 0.67\alpha Vf + 1.62(\alpha Vf)^2] \tag{9.43}$$

where, α is the shape factor (length/width of the filler), E_m is the elastic modulus of the matrix and E_c is the elastic modulus of the composite (Y. P. Wu 2004).

9.7. Tensile Strength and Modulus

The tensile strength and elastic modulus of 1.2vol% ND and CD filled

composites are lower than those of neat epoxy and this can be explained with the calculated critical volume fraction. The relevant properties (ε_f^*, σ_m^*, σ_f^* and σ_m') are determined using tensile testing of epoxy matrix and researches related with mechanical properties of frustules. The elastic modulus of diatom frustules of *T. punctigera* was reported as 22.4 GPa and frustules exhibited fully elastic deformations up to 2.5 % strain (Hamm, et al. 2003). Assuming linear elastic behavior of the frustules up to the failure stress, the failure strength of frustules is determined 560 MPa. The tensile strength (σ_m^*) of the epoxy is 52.53 MPa. With an epoxy elastic modulus of 2.6 GPa, the stress level in the epoxy at the frustules failure strains (σ_m') of 2.5% was 46.7 MPa. These values are used in determining the V_{min} and V_{crit} parameter for frustules filled epoxy in order to examine a range of potential composite strengths. The predicted composite strength in contrast to frustules volume fraction for CD, ND/epoxy composite is shown in Figure 9.3. The solid line is the predicted composite tensile strength. The minimum volume fraction (V_{min}) is 0.01 and for fiber volume fractions in the range $0<V_f<0.01$ failure of the frustules does not arrived to composite failure and composite failure occurs matrix failure strain. In this fiber fraction range the tensile strength decreases with increasing fiber fraction. At volume fractions greater than 0.01, fiber failure happens during fracture of composite. According to these results, critical volume percent of frustules was determined 1 and the tensile strength and modulus values decreases below this calculated value. The tensile results of both 1.2vol% frustules filled epoxy showed for both frustules inclusion, the tensile strength of samples was lower than the volume percent of 1. Critical volume fraction was calculated with assumption of using well aligned and continuous fiber in the matrix but our study the frustules was considered short fiber and randomly oriented in to the epoxy matrix. Therefore, this volume fraction value was changeable.

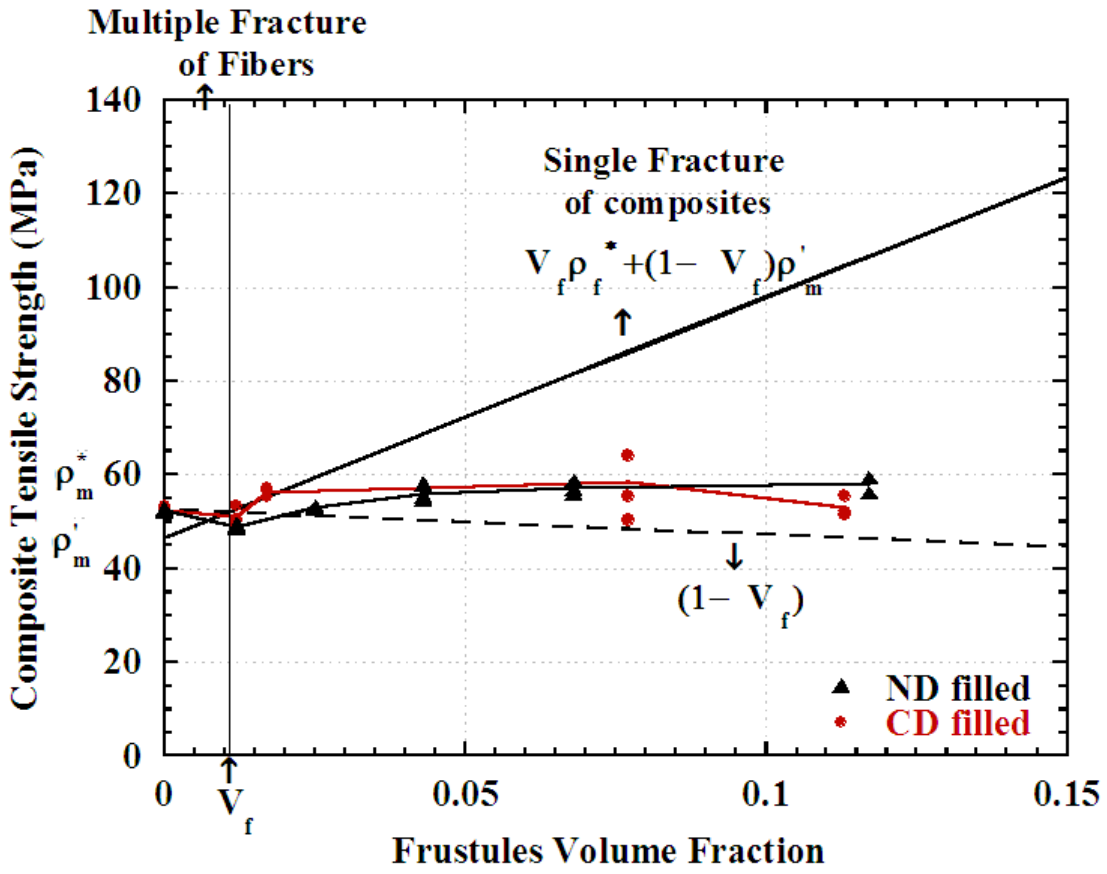

Figure 9.3 Tensile strength of CD and ND frustules filled epoxy composite as a function fiber volume fraction.

The strengths connected to the effectiveness of stress transfer between matrix and fillers and the particle loading for composites. It was noted that the composite strength decreased with increasing particle volume percent for the particles size above 80 nm (Fu Shao-Yun 2008) as the smaller particles improved the strength of composites due to high specific surface area. The strengths of ND filled epoxy composites are higher than those of CD/epoxy composites. This may be due to the smaller particle size of ND frustules and the interface adhesion between the particle and matrix or the randomly distributed particles in the matrix. Furthermore, it is noted that as the fiber volume contents increases, the composite strength increases slightly only. The combined effect of fiber volume fraction and mean fiber length leads to only a slight increase in the composite strength as the fiber volume fraction increases, namely the decrease in the composite strength caused by the reduction in mean fiber length almost offsets the increase in the composite strength caused by the increase in fiber volume

fraction (Fu, et al. 2000).

The variations of the elastic modulus of CD and ND filled epoxy composites as a function of frustules loading is shown in Figure 9.4. The modulus for both frustules filled composites increases with the increasing frustules volume content. The increase in elastic modulus of ND and CD filled composites is 52% and 26% for ≈7vol%, respectively. The effects of ND frustules on the modulus higher at the same volume percentage. At higher volume percent (11%) the increment in modulus of ND and CD filled epoxy is 56% and 42%, respectively. Jun Ma et al. (Jun Ma 2008) demonstrated 40% modulus improvement with the addition of 20 wt% silica nano particles into epoxy system.

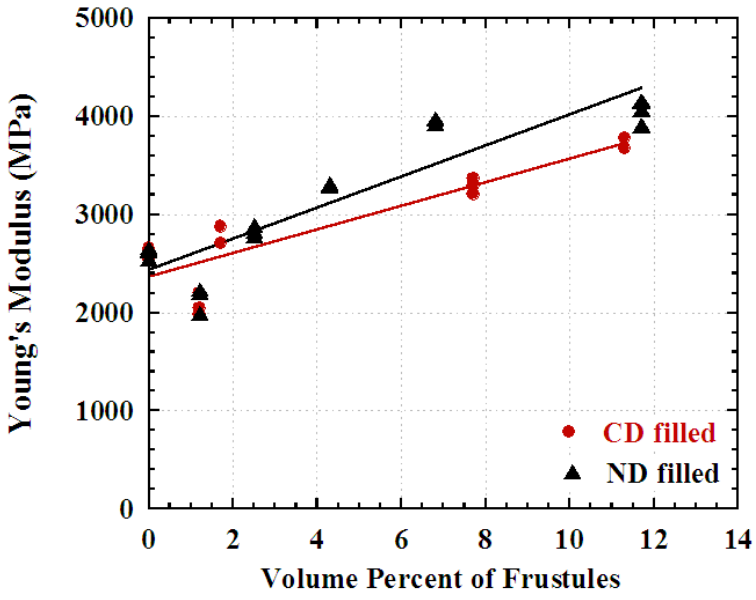

Figure 9.4. Elastic modulus of frustules filled epoxy.

The investigation of the mechanism of the fracture of the composite is very important to analyze the reliability of the components. The mechanism of the fracture of the composite, however, seems not to have been fully clarified because of the complicated behavior of the failure, which is much affected by the fiber length, the fiber orientation and the fiber/matrix bond strength, etc. (Sato, et al. 1984). The results show that mechanical properties of composites increase with increasing frustules volume percent and the strengthening mechanisms involved are based mainly on crack deflection, frustules debonding, and crushing. The existence of stronger interactions between the matrix and fibers can allow the debonding of the fiber instead of pull out ;

in this way, high energy may spread over a larger interfacial area (Li and Zhang 2010). In addition, Chen et al. (Chen and Tokaji 2004) proposed that crack initiation resistance decreased with increasing size of the particulate fillers (>20μm). At low strain rates, speed of crack propagation decreases at higher filler size because the distance between filler is large and crack propagation forms between matrix and filler interface and filler material acts as barrier to propagate cracks. At high strain rates, when filler size is higher then critical size (20 μm), small amount of course filler forms in the matrix at the same volume fraction. Therefore, at high strain rates, the fine particles filled composites show matrix dominated fracture. In this study, ND frustules filled epoxy samples contain more diatom frustules, simply arising from the smaller particles size.

The failure strains of CD and ND filled epoxy composites as function of fiber volume percent are shown in Figure 9.5. The composite failure strain decreases for both composites with the addition of frustules. The reduction in the failure strain is caused by the increased stiffness of the composites with increasing frustules filling. The cause of this effect has been identified as matrix crack formation at the ends of the reinforcing fibers. Because of stress concentration at the ends of the fibers, matrix crack formation starts at these points. As the fiber concentration increases, more cracks form. The failure strain values ND composite are smaller than those of CD filled composites. This confirmed that filler shapes show an effect on the failure strain of composites.

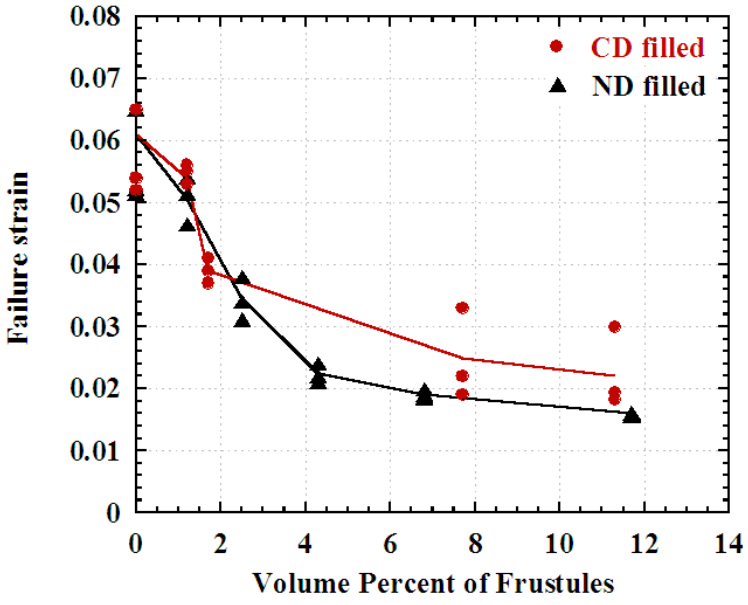

Figure 9.5. The variation failure strain of ND and CD/epoxy with volume percent.

The properties of matrix and filler such as Poisson's ratio, modulus, volume fraction, filler aspect ratio, filler distribution play significance role for composite models. The modulus of matrix material is 2.6 GPa. The modulus of CD and ND frustules is taken as 22.4 GPa (Wee, et al. 2005). Volume percentage of frustules changed between 0-15. Poisson ratio of matrix and frustules are taken as 0.3 and 0.17, respectively. The approximate aspect ratios of both frustules are calculated using Halpin Tsai Model and Guth Model for short fiber composites. The comparison of elastic modulus of CD and ND filled samples obtained from Halpin Tsai and Guth model and experimental elastic modulus are shown in Figures 9.6 and 9.7, respectively. Calculations are made 2.5 and 4.5 aspect ratios for CD and ND composites.. Experimental results demonstrated a good compatibility with modeling results. The predictions based on the Halpin Tsai and Guth equation with these aspect ratios result in with agreement with experimental results.

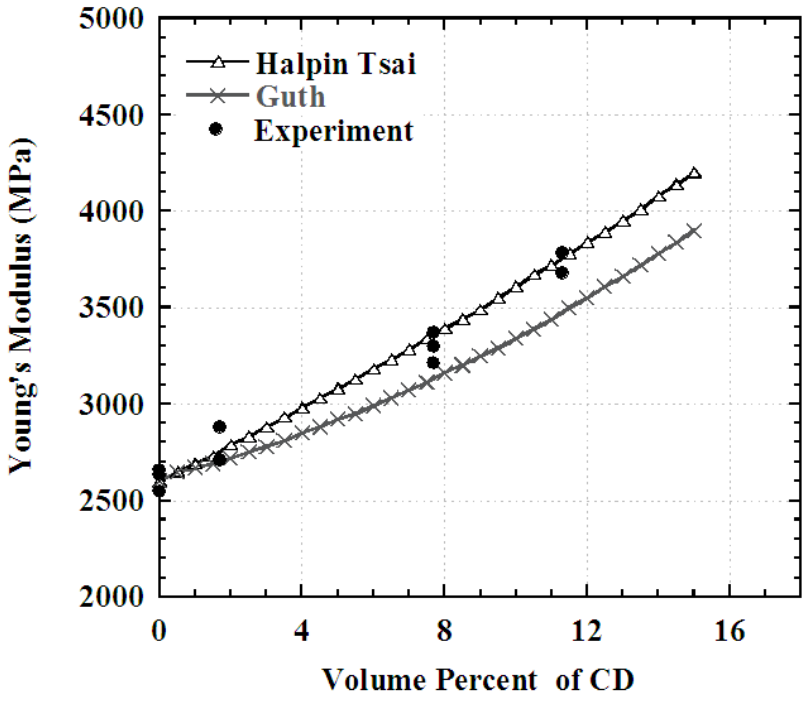

Figure 9.6. The comparison of elastic modulus of CD filled samples predicted from Halpin Tsai and Guth model and experimental elastic modulus.

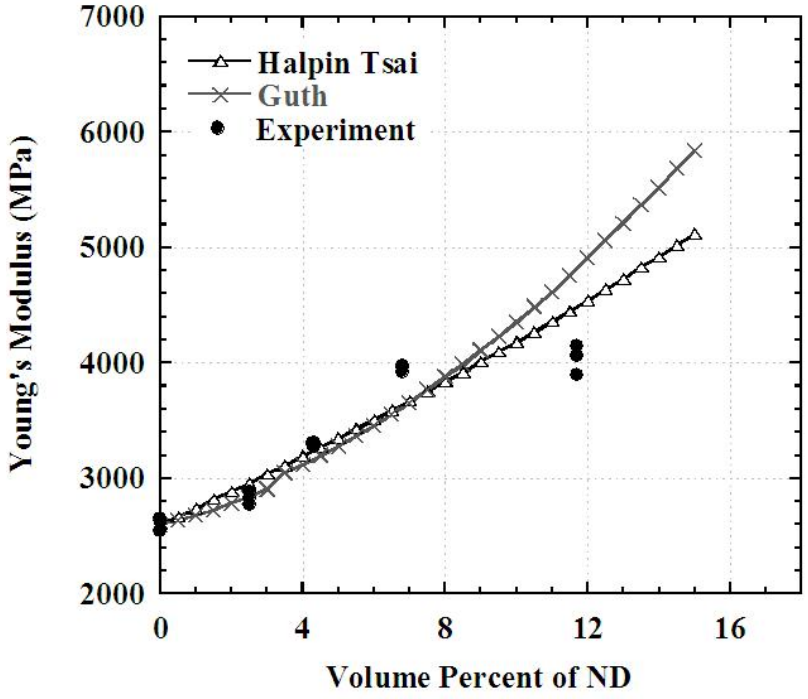

Figure 9.7. The comparison of elastic modulus of ND filled samples predicted from Halpin Tsai and Guth model and experimental elastic modulus.

The elastic moduli of CD and ND composites (along the long axis of the short fiber) are also calculated using rule of mixtures, shear lag model, modified shear lag model and the Eshelby model. The results are shown in Figure 9.8 and Figure 9.9 for CD and ND composites, respectively. As is seen in Figure 9.8, Eshelby model shows very good agreement with experimental elastic modulus values for CD filled composite. For ND filled composite, the experimental modulus vales are in between the elastic values predicted by the modified shear-lag model and Eshelby model as seen in Figure 9.9.

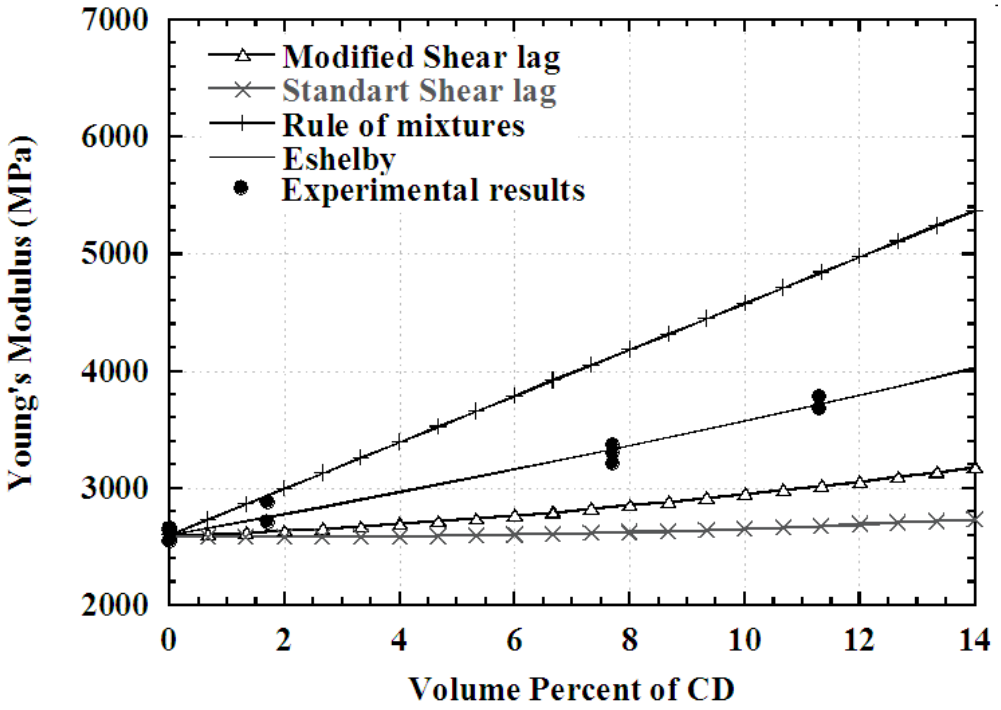

Figure 9.8. The elastic moduli of CD composites (along the long axis of the short fiber) calculated using rule of mixtures, shear lag model, modified shear lag model and the Eshelby model.

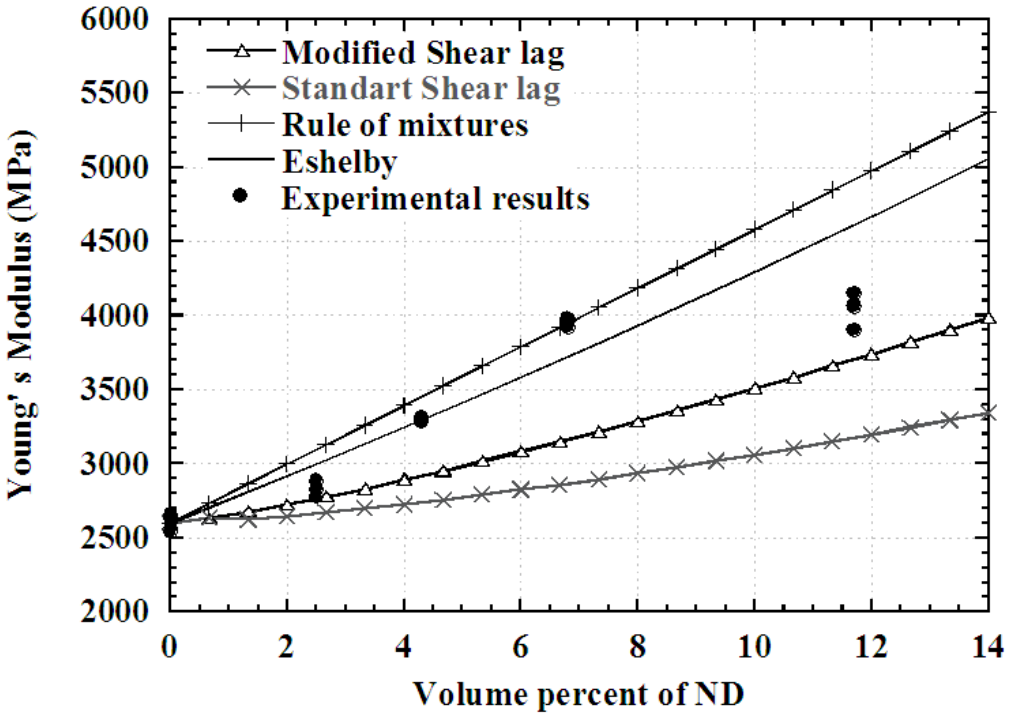

Figure 9.9. The elastic moduli of ND composites (along the long axis of the short fiber) calculated using rule of mixtures, shear lag model, modified shear lag model and the Eshelby model.

CHAPTER 10

CONCLUSIONS

Two different diatom frustules, natural diatomite (ND) and calcined diatom frustules (CD) were used as a filler in epoxy matrix in order to investigate the effect of diatom frustules filling on the mechanical properties of epoxy at quasi-static and high strain rates. The characterization of frustules showed that both frustules mainly consisted of silica with a small amount of other oxides. ND frustules had amorphous structure while CD crystal structure due to applied calcination process by the supplier. The morphological differences between two frustules were determined using SEM. CD frustules were mainly composed of *Melosira granulata* type diatom, cylindrical in shape. On the other hand, ND frustules had various different geometries. The mean particle size of ND and CD frustules were 15.1 and 37.5 μm respectively.

The thermal treatment, acid leaching and ball milling were performed to frustules to obtain silica powder from frustules. The acid leaching was applied to frustules at different concentrations and leaching times. At increasing HF concentrations, the variety of shapes, nanopores and open voids were seen on the surface of frustules as silica particles were removed from the surface. SEM micrograph results showed that HF significantly etched inside the existing pore structure of the diatom frustules. HF concentration was found more effective in mass loss than the leaching time. Thermal treatment induced several cracks propagated between macro pores and nanopores of the frustules. The observed smooth surfaces and grain boundaries of frustules at 1200 °C was because of transformation of the amorphous structure into crystal phase. Ball milling was applied at different milling times at 500 rpm to both frustules. Results showed that after 4 h grinding, the mean size of silica powders was reduced to 3 μm.

The glass transition of epoxy was determined as 105°C and post curing process was applied above this temperature at about 110 °C. The contact angles of CD/ND frustules and epoxy samples were measured as 14.60±0.87/19.24±0.84 and 80.21±1.72, respectively. The thermal stability of CD and ND filled epoxy samples was investigated at different volume percentage of frustules (0-12%). The patterns of the thermo

gravimetric curves of the ND and CD filled epoxy were found to be similar to the patterns of the neat epoxy. No significance differences between the initial decomposition temperature of the epoxy resins and frustules filled resin were found.

The compression test with strain rates of $1x10^{-3}$ and $1x10^{-1}$ s^{-1}. and 300-600 s^{-1} were applied on the CD and ND filled epoxy composites with the various volume percent (0-12 %). The increase in yield stress and modulus was sequentially found 27% and 59% for CD filled composite (10.8%). On the other hand, the increase in yield stress and modulus with the addition of ND frustules was 27% and 65%, respectively. Elastic modulus of the composites increased as the frustules content and strain rate increased. The increase in modulus of the frustules-filled composites indicated an increase in the rigidity of epoxy. Tensile tests of frustules filled epoxy samples also showed that elastic modulus increased with increasing frustule addition. The increase in the elastic modulus of ND and CD filled composites was 52% and 26% for ≈7% frustules content, respectively. Incorporation of CD frustules leaded to an increase in the tensile strength of the epoxy up to the particle addition of 8vol% except at 1.2 vol% CD addition. Tensile strength of ND filled epoxy also increased with increasing ND frustule content. Microscopic analysis of the fracture surfaces of samples tested at quasi-static strain rate showed the debonding and crushing of the frustules into several pieces. The characteristic damage mechanisms for neat and frustules filled epoxy samples under projectile impact were the radial and the cone cracks and the fragmentation of the cone. Results showed that the addition of ND enhanced the ballistic performance of epoxy. The aspect ratios of CD and ND frustules were determined as 2.5 and 4.5 using semi empirical equations such as Halpin Tsai and Guth Model. The modeling results showed good agreements with experimental results. The modulus of ND (6.8vol.%) filled epoxy according to Law of Mixture Model was very close to experimental results.

This study clearly indicated that the frustules filling improved the mechanical properties of epoxy at quasi-static and high strain rates. The use of higher aspect ratio diatom frustules as filler is recommended for the future studies.

REFERENCES

Adachi, T., Osaki, M., Araki, W. and Kwon, S. C., 2008, Fracture toughness of nano- and micro-spherical silica-particle-filled epoxy composites. *Acta Materialia*. 59(9): p. 2101-2109.

Ahmad, F. N., Jaafar, M., Palaniandy, S. and Azizli, K. A. M., 2008, Effect of particle shape of silica mineral on the properties of epoxy composites. *Composites Science and Technology*. 68(2): p. 346-353.

Aksoy, G., Polat, H., Polat, M. and Coskun, G., 2006, Effect of various treatment and glazing (coating) techniques on the roughness and wettability of ceramic dental restorative surfaces. *Colloids and Surfaces B-Biointerfaces*. 53(2): p. 254-259.

Almqvist, N., Delamo, Y., Smith, B. L., Thomson, N. H., Bartholdson, A., Lal, R., Brzezinski, M. and Hansma, P. K., 2001, Micromechanical and structural properties of a pennate diatom investigated by atomic force microscopy. *Journal of Microscopy-Oxford*. 202: p. 518-532.

Anderson, M. W., Holmes, S. M., Hanif, N. and Cundy, C. S., 2000, Hierarchical pore structures through diatom zeolitization. *Angewandte Chemie-International Edition*. 39(15): p. 2707-2710.

Bae, J., Jang, J. and Yoon, S. H., 2002, Cure Behavior of the liquid-crystalline epoxy/carbon nanotube system and the effect of surface treatment of carbon fillers on cure reaction. *Macromolecular Chemistry and Physics*. 203(15): p. 2196-2204.

Barra, G. M. O., Fredel, M. C., Al-Qureshi, H. A., Taylor, A. W. and Clemenceau, C., 2006, Properties of chemically treated natural amorphous silica fibers as polyurethane reinforcement. *Polymer Composites*. 27(5): p. 582-590.

Beier, U., Fischer, F., Sandler, J. K. W., Altstadt, V., Weimer, C. and Buchs, W., 2007, Mechanical performance of carbon fibre-reinforced composites based on stitched preforms. *Composites Part a-Applied Science and Manufacturing*. 38(7): p. 1655-1663.

Bradbury, Jane, 2004, Nature's Nanotechnologists: Unveiling the Secrets of Diatoms. *PLoS Biology*. 2(10): p. 306-347.

Cai, Y., Allan, S. M. and Sandhage, K. H., 2005, Three-dimensional magnesia-based nanocrystal assemblies via low-temperature magnesiothermic reaction of diatom microshells. *Journal of the American Ceramic Society*. 88(7): p. 2005-2010.

Chatterjee and A.Islam, M. S., 2008, Fabrication and characterization of TiO2 epoxy nanocomposite. *Materials Science and Engineering a-Structural Materials Properties Microstructure and Processing*. 487(1-2): p. 574-585.

Chen, C. G., Justice, R. S., Schaefer, D. W. and Baur, J. W., 2008a, Highly dispersed nanosilica-epoxy resins with enhanced mechanical properties. *Polymer*. 49(17): p. 3805-3815.

Chen, Q., Chasiotis, I., Chen, C. and Roy, A., 2008b, Nanoscale and effective mechanical behavior and fracture of silica nanocomposites. *Composites Science and Technology*. 68(15-16): p. 3137-3144.

Chen, W. and Ravichandran, G., 1994, Dynamic Compressive Behavior Of Ceramics Under Lateral Confinement. *Journal De Physique Iv*. 4(C8): p. 177-182.

Chen, Z. Z. and Tokaji, K., 2004, Effects of particle size on fatigue crack initiation and small crack growth in SiC particulate-reinforced aluminium alloy composites. *Materials Letters*. 58(17-18): p. 2314-2321.

Conley, D. J., Kilham, S. S. and Theriot, E., 1989, Differences in Silica Content Between Marine and Fresh-water Diatoms *Limnology and Oceanography*. 34(1): p. 205-213.

Cox, HF., 1952, The elasticity and strength of paper and other fibrous materials. *British Journal of Applied Physics*. 3: p. 29-72.

Crawford, S. A., Higgins, M. J., Mulvaney, P. and Wetherbee, R., 2001, Nanostructure of the diatom frustule as revealed by atomic force and scanning electron microscopy. *Journal of Phycology*. 37(4): p. 543-554.

De Rosa, I. M., Kenny, J. M., Puglia, D., Santulli, C. and Sarasini, F., 2010, Morphological, thermal and mechanical characterization of okra (Abelmoschus esculentus) fibres as potential reinforcement in polymer composites. *Composites Science and Technology*. 70(1): p. 116-122.

Dudley, S., Kalem, T. and Akinc, M., 2006, Conversion of SiO2 diatom frustules to BaTiO3 and SrTiO3. *Journal of the American Ceramic Society*. 89(8): p. 2434-2439.

EPMinerals, EP Management and Corporation. *www.epminerals.com*., 2010.

Eshelby, J.D., 1957, The determination of the elastic field of an ellipsoidal inclusion and related problems. . *Proceedings of the Royal Society A*. 241: p. 376-396.

Eshelby, J.D. , 1961, Elastic inclusions and inhomogeneities. *Progress in Solid Mechanics*. 2: p. 89-140.

Fraga, F., Burgo, S. and Nunez, E. R., 2001, Curing kinetic of the epoxy system BADGE n=0/1,2 DCH by Fourier Transform Infrared Spectroscopy (FTIR). *Journal of Applied Polymer Science*. 82(13): p. 3366-3372.

Fraga, F., Vazquez, E. C., Rodriguez-Nunez, E. and Martinez-Ageitos, J. M., 2008, Curing kinetics of the epoxy system diglycidyl ether of bisphenol A/isophoronediamine by Fourier transform infrared spectroscopy. *Polymers for Advanced Technologies*. 19(11): p. 1623-1628.

Fu, S. J., Wu, P. P. and Han, Z. W., 2002, Tensile strength and rupture energy of hybrid poly(methylvinylsiloxane) composites reinforced with short PET fibers and wollastonite whiskers. *Composites Science and Technology*. 62(1): p. 3-8.

Fu, S. Y., Lauke, B., Mader, E., Yue, C. Y. and Hu, X., 2000, Tensile properties of short-glass-fiber- and short-carbon-fiber-reinforced polypropylene composites. *Composites Part a-Applied Science and Manufacturing*. 31(10): p. 1117-1125.

Fu Shao-Yun, Feng Xi-Qiao, Lauke Bernd, Mai Yiu-Wing, 2008, Effects of Particle size, particle/matrix interface adhesion and particle loading on mechanical properties of particulate-polymer composites. *Composites Part B-Engineering*. 39: p. 933-961.

Fuhrmann, T., Landwehr, S., El Rharbi-Kucki, M. and Sumper, M., 2004, Diatoms as living photonic crystals. *Applied Physics B-Lasers and Optics*. 78(3-4): p. 257-260.

Fukuda, H. and Chou, T. W., 1981, An Advanced Shear-Lag Model Applicable to Discontinuous Fiber Composites *Journal of Composite Materials*. 15(JAN): p. 79-91.

Gaddis, C. S. and Sandhage, K. H., 2004, Freestanding microscale 3D polymeric structures with biologically-derived shapes and nanoscale features. *Journal of Materials Research*. 19(9): p. 2541-2545.

Goldberg, E. L., Grachev, M. A., Bobrov, V. A., Bessergenev, A. V., Zolotaryov, B. V. and Likhoshway, Y. V., 1998, Do diatom algae frustules accumulate uranium? *Nuclear Instruments & Methods in Physics Research Section a-Accelerators Spectrometers Detectors and Associated Equipment*. 405(2-3): p. 584-589.

Gordon, R. and Drum, R. W., 1994, The Chemical Basis of Diatom Morphogenesis, International Review of Cytology - a Survey of Cell Biology, Vol 150 ed. 243-372,

Gordon, R. and Parkinson, J., 2005, Potential roles for diatomists in nanotechnology. *Journal of Nanoscience and Nanotechnology*. 5(1): p. 35-40.

Goren, R., Baykara, T. and Marsoglu, M., 2002, Effects of purification and heat treatment on pore structure and composition of diatomite. *British Ceramic Transactions*. 101(4): p. 177-180.

Guo, T., Wang, L. S., Zhang, A. Q. and Cai, T. M., 2005, Effects of nano calcium carbonate modified by a lanthanum compound on the properties of polypropylene. *Journal of Applied Polymer Science*. 97(3): p. 1154-1160.

Guo, Y. Z. and Li, Y. L., 2007, Quasi-static/dynamic response of SiO2-epoxy nanocomposites. *Materials Science and Engineering a-Structural Materials Properties Microstructure and Processing*. 458(1-2): p. 330-335.

Guth, E., 1945, Theory of Filler Reinforcement. *J. Appl Phys*. 16: p. 20.

Hamm, C. E., Merkel, R., Springer, O., Jurkojc, P., Maier, C., Prechtel, K. and Smetacek, V., 2003, Architecture and material properties of diatom shells provide effective mechanical protection. *Nature*. 421(6925): p. 841-843.

Harada, M., Morimoto, M. and Ochi, M., 2003, Influence of Network Chain Orientation on the Mechanical
Property of Epoxy Resin Filled with Silica Particles. *Journal of Applied Polymer Science*. 87: p. 787-794.

Hassan, A., Salema, A. A., Ani, F. N. and Abu Baker, A., 2010, A Review on Oil Palm Empty Fruit Bunch Fiber-Reinforced Polymer Composite Materials. *Polymer Composites*. 31(12): p. 2079-2101.

Hetherington, J. G., 1992, An Investigation into the Energy Absorbed During Ballistic Perforation of Composite Armors-Reply. *International Journal of Impact Engineering*. 12(2): p. 325-327.

Hourston, Mike Reading and Douglas J., 2006, Modulated Temperature Differential Scanning Calorimetry Theoretical and Practical Applications in Polymer Characterisation *Springer Link.*

Hsueh, C. H., 1995, A Modified Analysis fro Stress Transfer in Fiber -reinforced composites with bonded fiber ends. *Journal of Materials Science*. 30(1): p. 219-224.

Hsueh, C. H., 2000, Young's modulus of unidirectional discontinuous-fibre composites. *Composites Science and Technology*. 60(14): p. 2671-2680.

Hsueh, C. H., Young, R. J., Yang, X. and Becher, P. F., 1997, Stress transfer in a model composite containing a single embedded fiber. *Acta Materialia*. 45(4): p. 1469-1476.

Hui Zhang , Long-Cheng Tang , Zhong Zhang , Klaus Friedrich , Stephan Sprenger, 2008, Fracture behaviours of in situ silica nanoparticle filled epoxy at different temperatures. *Polymer*. 49: p. 3816–3825.

Ichazo, M. N., Albano, C., Gonzalez, J., Perera, R. and Candal, M. V., 2001, Polypropylene/wood flour composites: treatments and properties. *Composite Structures*. 54(2-3): p. 207-214.

Imanaka, M., Takeuchi, Y., Nakamura, Y., Nishimura, A. and Iida, T., 2001, Fracture toughness of spherical silica-filled epoxy adhesives. *International Journal of Adhesion and Adhesives*. 21(5): p. 389-396.

Iveson, S. M., Holt, S. and Biggs, S., 2000, Contact angle measurements of iron ore powders. *Colloids and Surfaces a-Physicochemical and Engineering Aspects*. 166(1-3): p. 203-214.

J. C. Halpin, J. L. Kardos, 1976, The Halpin-Tsai Equations: A Review *Polm Eng Sci*. 16: p. 344-352.

Ji, X. L., Hampsey, J. E., Hu, Q. Y., He, J. B., Yang, Z. Z. and Lu, Y. F., 2003, Mesoporous silica-reinforced polymer nanocomposites. *Chemistry of Materials*. 15(19): p. 3656-3662.

Ji, X. L., Jing, J. K., Jiang, W. and Jiang, B. Z., 2002, Tensile modulus of polymer nanocomposites. *Polymer Engineering and Science*. 42(5): p. 983-993.

Jiang, J. K., Oberdorster, G. and Biswas, P., 2009, Characterization of size, surface charge, and agglomeration state of nanoparticle dispersions for toxicological studies. *Journal of Nanoparticle Research*. 11(1): p. 77-89.

Joseph, P. V., Joseph, K. and Thomas, S., 1999, Effect of processing variables on the mechanical properties of sisal-fiber-reinforced polypropylene composites. *Composites Science and Technology*. 59(11): p. 1625-1640.

Jun Ma, Mao-Song Mo, Xu-Sheng Du, Patrick Rosso, Klaus Friedrich, Hsu-Chiang Kuan 2008, Effect of inorganic nanoparticles on mechanical property, fracture toughness and toughening mechanism of two epoxy systems. *Polymer*. 49: p. 3510-3523.

Kinloch, A. J. and Taylor, A. C., 2006, The mechanical properties and fracture behaviour of epoxy-inorganic micro- and nano-composites. *Journal of Materials Science*. 41(11): p. 3271-3297.

Kwon, S. C. and Adachi, T., 2007, Strength and fracture toughness of nano and micron-silica particles bidispersed epoxy composites: evaluated by fragility parameter. *Journal of Materials Science*. 42(14): p. 5516-5523.

Kwon, S. C., Adachi, T., Araki, W. and Yamaji, A., 2008, Effect of composing particles of two sizes on mechanical properties of spherical silica-particulate-reinforced epoxy composites. *Composites Part B-Engineering*. 39(4): p. 740-746.

Li, J. and Zhang, Y. F., 2010, The Tensile Properties of Short Carbon Fiber Reinforced ABS and ABS/PA6 Composites. *Journal of Reinforced Plastics and Composites*. 29(11): p. 1727-1733.

Li, X. W., Bian, C. Q., Chen, W., He, J. B., Wang, Z. Q., Xu, N. and Xue, G., 2003a, Polyaniline on surface modification of diatomite: a novel way to obtain conducting diatomite fillers. *Applied Surface Science*. 207(1-4): p. 378-383.

Li, X. W., Bian, C. Q., Chen, W., Xue, G., Zhu, W. and Fang, J. N., 2003b, Spectral studies of a polyaniline/diatomite composite. *Spectroscopy Letters*. 36(1-2): p. 25-33.

Losic, D., Mitchell, J. G. and Voelcker, N. H., 2005, Complex gold nanostructures derived by templating from diatom frustules. *Chemical Communications*,(39): p. 4905-4907.

Losic, D., Short, K., Mitchell, J. G., Lal, R. and Voelcker, N. H., 2007, AFM nanoindentations of diatom biosilica surfaces. *Langmuir*. 23(9): p. 5014-5021.

Metin, D., Tihminhoglu, F., Balkose, D. and Ulku, S., 2004, The effect of interfacial interactions on the mechanical properties of polypropylene/natural zeolite composites. *Composites Part a-Applied Science and Manufacturing*. 35(1): p. 23-32.

Mori, T. and Tanaka, K., 1973, Average stress in matrix and average elastic energy of materials with misfitting. *Acta Metallurgica*. 21(5): p. 571-574.

Mulliken, A. D. and Boyce, M. C., 2006, Polycarbonate and a polycarbonate-POSS nanocomposite at high rates of deformation. *Symposium on Time-Dependent Behaviors of Polymers and Polymer Matrix Composites*: p. 543-550

Nairn, J. A., 1997, On the use of shear-lag methods for analysis of stress transfer unidirectional composites. *Mechanics of Materials*. 26(2): p. 63-80.

Nakamura, Y., Yamaguchi, M. and Okubo, M., 1993, Instrumented Charpy Impact Test of Epoxy-Resin Filled with Irregular-Shaped Silica Particles. *Polymer Engineering and Science*. 33(5): p. 279-284.

Nakamura, Y., Yamaguchi, M., Okubo, M. and Matsumoto, T., 1992, Effect of particle size on the fracture toughness of epoxy resin filled with spherical silica. *Polymer*. 33(16): p. 3415-3426.

Ongerth, J. E. and Hutton, P. E. , 1997, DE filtration to remove Cryptosporidium. *J. Am. Water Works Assoc.* . 89: p. 39-4.

Park, I. and Pinnavaia, T. J., 2007, Mesocellular silica foam as an epoxy polymer reinforcing agent. *Advanced Functional Materials*. 17(15): p. 2835-2841.

Parkinson, J. and Gordon, R., 1999, Beyond micromachining: the potential of diatoms. *Trends in Biotechnology*. 17(5): p. 190-196.

Pickett-Heaps, J.D., Schmid, A.M. and Edgar, L.A. , 1990, The cell biology of diatom valve formation. *Progress in Phycological Research*. 7: p. 1-168.

Pilyugin, N. N., 2008a, Destruction of filled polymer targets by high-velocity impact. *Combustion Explosion and Shock Waves*. 44(2): p. 239-247.

Pilyugin, N. N., 2008b, Determining the Strength of Filled Epoxy from Ballistic Experiments. *Combustion Explosion and Shock Waves*. 44(5): p. 607-613.

Praveen, S., Sun, Z. F., Xu, J. G., Patel, A., Wei, Y., Ranade, R. and Baran, G., 2006, Compression and aging properties of experimental dental composites containing mesoporous silica as fillers. *Molecular Crystals and Liquid Crystals*. 448: p. 223-231.

Presising, H.R., 1994, Siliceous Structures and Silicification in Flagellated Protists. *Protoplasma*. 181: p. 29-42.

Pukanszky B, Voros G., 1993, Mechanism of interfacial interactions in particulate filled composites. *compos interf*. 1: p. 411-427.

Radford, K. C., 1971, Mechanical Properties of an Epoxy Resin with a Second Phase Dispersion. *Journal of Materials Science*. 6(10): p. 1286-&.

Ramis, X., Salla, J. M., Mas, C., Mantecon, A. and Serra, A., 2004, Kinetic study by FTIR, TMA, and DSC of the curing of a mixture of DGEBA resin and gamma-butyrolactone catalyzed by ytterbium triflate. *Journal of Applied Polymer Science*. 92(1): p. 381-393.

Sahu, S. and Broutman, L. J., 1972, Mechanical Properties of Particulate Composites. *Polymer Engineering and Science*. 12(2): p. 91-&.

Sandhage, K. H., Allan, S. M., Dickerson, M. B., Gaddis, C. S., Shian, S., Weatherspoon, M. R., Cai, Y., Ahmad, G., Haluska, M. S., Snyder, R. L., Unocic, R. R., Zalar, F. M., Zhang, Y. S., Rapp, R. A., Hildebrand, M. and Palenik, B. P., 2005, Merging biological self-assembly with synthetic chemical tailoring: The potential for 3-D genetically engineered micro/nano-devices (3-D GEMS). *International Journal of Applied Ceramic Technology*. 2(4): p. 317-326.

Sato, N., Kurauchi, T., Sato, S. and Kamigaito, O., 1984, Mechanism of Fracture of Short Glass Fiber-Reinforced Polyamide Thermoplastic. *Journal of Materials Science*. 19(4): p. 1145-1152.

Scala, S. and Bowler, C., 2001, Molecular insights into the novel aspects of diatom biology. *Cellular and Molecular Life Sciences*. 58(11): p. 1666-1673.

Sherman, D. and Ben-Shushan, T., 1998, Quasi-static impact damage in confined ceramic tiles. *International Journal of Impact Engineering*. 21(4): p. 245-265.

Shian, S., Cai, Y., Weatherspoon, M. R., Allan, S. M. and Sandhage, K. H., 2006, Three-dimensional assemblies of zirconia nanocrystals via shape-preserving reactive conversion of diatom microshells. *Journal of the American Ceramic Society*. 89(2): p. 694-698.

Singh, R. P., Zhang, M. and Chan, D., 2002, Toughening of a brittle thermosetting polymer: Effects of reinforcement particle size and volume fraction. *Journal of Materials Science*. 37(4): p. 781-788.

Stoermer E F, Smol J P, 2004, The Diatoms: Applications for the Environmental and Earth Sciences. *Cambridge University Press*.

Strzelczyk, F., Leterq, D., Wilhelm, A. M. and Steinbrunn, A., 1998, Gas-solid chromatographic separation of hydrogen isotopes: a comparison between two palladium bearing materials - alumina and kieselguhr. *Journal of Chromatography A*. 822(2): p. 326-331.

Suarez, J. C. M., Coutinho, F. M. B. and Sydenstricker, T. H., 2003, SEM studies of tensile fracture surfaces of polypropylene - sawdust composites. *Polymer Testing*. 22(7): p. 819-824.

Subhash, G., Yao, S., Bellinger, B. and Gretz, M. R., 2005, Investigation of mechanical properties of diatom frustules using nanoindentation. *Journal of Nanoscience and Nanotechnology*. 5(1): p. 50-56.

Tandon, G. P. and Weng, G. J., 1984, The effect of aspect ratio of inclusions on the elastic properties of unidirectionally aligned composites. *Polymer Composites*. 5(4): p. 327-333.

Tasdemir, M., Akalin, M., Kocak, D., Usta, I. and Merdan, N., 2010, Investigation of Properties of Polymer/Textile Fiber Composites. *International Journal of Polymeric Materials*. 59(3): p. 200-214.

Tasdemirci, A., Yuksel, S., Karsu, D., Gulturk, E., Hall, I. W. and Guden, M., 2008, Diatom frustule-filled epoxy: Experimental and numerical study of the quasi-static and high strain rate compression behavior. *Materials Science and Engineering a-Structural Materials Properties Microstructure and Processing*. 480(1-2): p. 373-382.

Taya, M. and Arsenault, R. J., 1989, Metal matrix composites : thermomechanical behavior. , Pergamon Press.

Thio, Y. S., Argon, A. S. and Cohen, R. E., 2004, Role of interfacial adhesion strength on toughening polypropylene with rigid particles. *Polymer*. 45(10): p. 3139-3147.

Tsai, W. T., Hsien, K. J. and Lai, C. W., 2004, Chemical activation of spent diatomaceous earth by alkaline etching in the preparation of mesoporous adsorbents. *Industrial & Engineering Chemistry Research*. 43(23): p. 7513-7520.

Tsai, W. T., Lai, C. W. and Hsien, K. J., 2006, Characterization and adsorption properties of diatomaceous earth modified by hydrofluoric acid etching. *Journal of Colloid and Interface Science*. 297(2): p. 749-754.

Unocic, R. R., Zalar, F. M., Sarosi, P. M., Cai, Y. and Sandhage, K. H., 2004, Anatase assemblies from algae: coupling biological self-assembly of 3-D nanoparticle structures with synthetic reaction chemistry. *Chemical Communications*,(7): p. 796-797.

Vrieling, E. G., Beelen, T. P. M., van Santen, R. A. and Gieskes, W. W. C., 1999a, Diatom silicon biomineralization as an inspirational source of new approaches to silica production. *Journal of Biotechnology*. 70(1-3): p. 39-51.

Vrieling, E. G., Gieskes, W. W. C. and Beelen, T. P. M., 1999b, Silicon deposition in diatoms: Control by the pH inside the silicon deposition vesicle. *Journal of Phycology*. 35(3): p. 548-559.

Wee, K. M., Rogers, T. N., Altan, B. S., Hackney, S. A. and Hamm, C., 2005, Engineering and medical applications of diatoms. *Journal of Nanoscience and Nanotechnology*. 5(1): p. 88-91.

Werner, D., 1977, The Biology of Diatoms, University of California Press.

Wichmann, M. H. G., Cascione, M., Fiedler, B., Quaresimin, M. and Schulte, K., 2006, Influence of surface treatment on mechanical behaviour of fumed silica/epoxy resin nanocomposites. *Composite Interfaces*. 13(8-9): p. 699-715.

Wilkins, M. L., 1978, Mechanics of Penetration and Perforation. *International Journal of Engineering Science*. 16(11): p. 793-807.

Withers, P. J., Stobbs, W. M. and Pedersen, O. B., 1989, The application of the Eshelby method of internal-stress determination to short fiber metal matrix composites. *Acta Metallurgica*. 37(11): p. 3061-3084.

Xiao, W. S., Peng, W. S., Wang, G. X., Wang, F. Y. and Weng, K. N., 2004, Infrared spectroscopic study of changbaishan diatomite. *Spectroscopy and Spectral Analysis*. 24(6): p. 690-693.

Xing, X. S. and Li, R. K. Y., 2004, Wear behavior of epoxy matrix composites filled with uniform sized sub-micron spherical silica particles. *Wear*. 256(1-2): p. 21-26.

Y. P. Wu, Q.X. Jia, D. S. Yu, L. Q. Zhang, 2004, Modeling Young's Modulus of Rubber-Clay Nanocomposites Using Composite Theories. *Polymer Testing* 23: p. 903-909.

Yuan, P., He, H.P., Wu, D.Q., Wang, D.Q. and Chen, L.J., 2004, Characterization of diatomaceous silica by Raman spectroscopy. *Spectrochimica Acta Part a-Molecular and Biomolecular Spectroscopy*. 60: p. 2941-2945.

Zafeiropoulos, N. E., Williams, D. R., Baillie, C. A. and Matthews, F. L., 2002, Engineering and characterisation of the interface in flax fibre/polypropylene composite materials. Part I. Development and investigation of surface treatments. *Composites Part a-Applied Science and Manufacturing*. 33(8): p. 1083-1093.

Zhang, H., Zhang, Z., Friedrich, K. and Eger, C., 2006, Property improvements of in situ epoxy nanocomposites with reduced interparticle distance at high nanosilica content. *Acta Materialia*. 54(7): p. 1833-1842.

Zhang, Z. G., Wang, M. C., Song, S. C., Li, M. and Sun, Z. J., 2010, Influence of panel/back thickness on impact damage behavior of alumina/aluminum armors. *Journal of the European Ceramic Society*. 30(4): p. 875-887.

Zhao, H. X. and Li, R. K. Y., 2008, Effect of water absorption on the mechanical and dielectric properties of nano-alumina filled epoxy nanocomposites. p. 602-611

Zhao, J. P., Gaddis, C. S., Cai, Y. and Sandhage, K. H., 2005, Free-standing microscale structures of nanocrystalline zirconia with biologically replicable three-dimensional shapes. *Journal of Materials Research*. 20(2): p. 282-287.

Zhao, S., Schadler, L. S., Hillborg, H. and Auletta, T., 2008, Improvements and mechanisms of fracture and fatigue properties of well-dispersed alumina/epoxy nanocomposites. p. 2976-2982

Zurzolo, C. and Bowler, C., 2001, Exploring Bioinorganic Pattern Formation in Diatoms. A Story of Polarized Trafficking. *Plant Physiology* 127: p. 1339-1345.

VITA

Elif GÜLTÜRK
1978 Erzurum

EDUCATION

- B.Sc: (2000) Department of Mechanical Engineering, Cumhuriyet University, Turkey.
- M.Sc: (2003) Department of Mechanical Engineering, Cumhuriyet University, Turkey.
- PhD: (2010) Department of Mechanical Engineering, Izmir Institute of Technology, Turkey (in English).

PUBLICATIONS

- Tasdemirci A., Yuksel S., Karsu D., Gulturk E., Hall I.W., Guden M., Diatom Frustule-Filled Epoxy:Experimental and Numerical Study of the Quasi-static and High Strain Rate Compression Behavior, *Materials Science and Engineering A*, 480 (2008) 373-382.

- Gulturk E. and Guden M., Diatom Frustules and Their Use in Polymers as Filling Material: Microscopic and Mechanical Investigation, *5. Ulusal Nanobilim ve Nanoteknoloji Konferansı,* 08-12 Haziran 2009, Eskişehir.

- Guden M. and Gulturk E., Fosil nano silika diatom kabuklarının nano sertlik özellikleri, *18. Ulusal Elektron Mikroskopi Kongresi,* 27-29 Ağustos 2007, Eskişehir.

- Gulturk E. and Guden M., Diyatom Kabuklarının Mikroyapısal Analizi ve Kabuklardan Nano-Silika Toz Elde Edilmesi, *12. Denizli Malzeme Sempozyumu Bildiriler Kitabı,* Sf. 312-319, 15-17 Ekim 2008, Denizli.